

INSTITUTE FOR CHEMICAL AND BIOENGINEERING
DEPARTMENT OF CHEMISTRY AND APPLIED BIOSCIENCES
ETH ZURICH
8093 ZURICH, SWITZERLAND

LECTURE NOTES

(INTENDED TO COMPLETE BUT
NOT TO SUBSTITUTE THE LECTURES)

**POLYMER REACTION
&
COLLOID ENGINEERING**

PROF. DR. M. MORBIDELLI

October 29, 2015

AUTUMN SEMESTER 2015

Contents

1 Free-Radical Polymerization	5
1.1 Chemical Reactions	5
1.1.1 Initiation	5
1.1.2 Propagation	6
1.1.3 Chain Transfer	6
1.1.4 Bimolecular Termination	8
1.2 Diffusion Control of Chemical Reactions	8
1.3 Polymerization Processes	10
1.3.1 Bulk Polymerization	10
1.3.2 Solution Polymerization	10
1.3.3 Suspension Polymerization	10
1.3.4 Emulsion Polymerization	10
1.4 Kinetics of Free-Radical Polymerization	11
1.4.1 Involved Chemical Reactions	11
1.4.2 Population Balance Equations in a Batch Reactor	11
1.4.3 Rate of Monomer Consumption	13
1.5 Pseudo Steady State Approximation	14
1.5.1 Stiffness Ratio	17
2 Chain Length Distribution of Polymers	19
2.1 Population Balance Equations	19
2.1.1 Active Chains	19
2.1.2 Dead Chains	21
2.2 Instantaneous Chain Length Distribution	23
2.2.1 Number Distribution and Number Average	23
2.2.2 Weight Distribution and Weight Average	24
2.2.3 Polydispersity	25
2.2.4 Summary	26
3 Cumulative Properties of Polymers	27
3.1 Cumulative Chain Length Distribution, Moments, and Properties	27
3.1.1 Width of the Cumulative Distribution	29
3.2 Designing Polymerization Processes with Respect to Desired CLDs	30
3.2.1 Case I: Termination by Combination is Negligible	30
3.2.2 Case II: Termination by Combination Dominates	32

Contents

4 Copolymerization	34
4.1 Kinetics of Copolymerization	34
4.1.1 Involved Chemical Reactions	34
4.1.2 Long-Chain Approximation	35
4.1.3 Rate of Monomer Consumption	36
4.2 Chain Length Distribution of Copolymers	37
4.2.1 Population Balance Equation	37
4.2.2 Pseudo-Homogeneous Approach	37
4.2.3 Kinetics of Multi-Monomer Polymerization	38
4.3 Chain Composition Distribution of Copolymers	40
4.3.1 Instantaneous Chain Composition	40
4.3.2 Composition Drift	42
4.3.3 Chain Composition Control	43
4.3.4 Reactor Monitoring and Control	49
5 Heterogeneous Free-Radical Polymerization	52
5.1 Concept of Micellar Particle Nucleation	52
5.2 Radical Segregation	53
5.3 Phase Partitioning	55
5.3.1 Monomer	56
5.3.2 Emulsifier	56
5.4 Colloidal Stability	57
5.5 Kinetic Mechanism of Emulsion Polymerization (Smith & Ewart, 1954)	57
5.6 Kinetics of Micellar Particle Nucleation	60
5.7 Distribution of Active Radicals in the Polymer Particles	62
6 Stability of Colloidal Suspensions	66
6.1 Kinetic Stability of Colloidal Suspensions	66
6.2 Interaction between two Charged Bodies	67
6.2.1 van der Waals Forces	67
6.2.2 Electrostatic Forces	71
6.2.3 Total Interaction Energy	84
6.2.4 Simple Manifestation of Electrical Double Layers: Soap Films	85
6.3 Coagulation of Colloidal Suspensions	85
6.3.1 Aggregation by Potential Control	87
6.3.2 Aggregation by Electrolyte Addition	87
6.4 Steric Interactions	89
7 Kinetics and Structure of Colloidal Aggregates	93
7.1 Diffusion Limited Cluster Aggregation – DLCA	93
7.1.1 Aggregation Rate Constant – DLCA	93
7.1.2 Cluster Mass Distribution – DLCA	95

Contents

7.1.3	Role of Aggregate Morphology – DLCA	96
7.2	Reaction Limited Cluster Aggregation – RLCA	98
7.2.1	Aggregation Rate Constant – RLCA	98
7.2.2	Role of Cluster Morphology – RLCA	101
7.2.3	Cluster Mass Distribution – RLCA	103
7.3	Comparison of Aggregation Regimes – DLCA vs. RLCA	103
7.3.1	Aggregation Rate Constant – DLCA vs. RLCA	103
7.3.2	Cluster Mass Distribution – DLCA vs. RLCA	104
7.3.3	Aggregate Morphology – DLCA vs. RLCA	107
7.3.4	Comparison to Experimental Data	108
7.4	Cluster Coalescence	109
7.5	Solid Suspensions under Shear	114
7.5.1	Shear induced Aggregation	114
7.5.2	Shear induced Breakage	119
7.6	Gelation of Colloidal Suspensions	120
7.6.1	The Gelation Process	120
7.6.2	Brownian-Induced Gelation	122
7.6.3	Shear-Induced Gelation	123
7.7	Experimental Characterization of Colloidal Suspensions	126
7.7.1	Light Scattering	126
7.7.2	Static Light Scattering	127
7.7.3	Dynamic Light Scattering	133
7.8	Zeta Potential, Electrophoretic Mobility, and Surface Charge Density	135
8	Protein Aggregation	140
8.1	Introduction	140
8.2	Monoclonal Antibodies	141
8.3	Protein Colloidal Stability	142
8.4	Protein Conformational Stability	143
8.5	Mechanisms of Protein Aggregation	144
8.6	Aggregation Kinetics and Reaction Order	145
8.7	Case Studies	146
8.7.1	Case Study 1: mAb-1	147
8.7.2	Case Study 2: mAb-2	162
8.8	Conclusion	171

Chapter 1

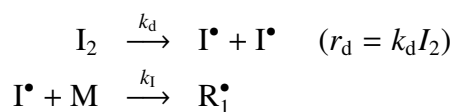
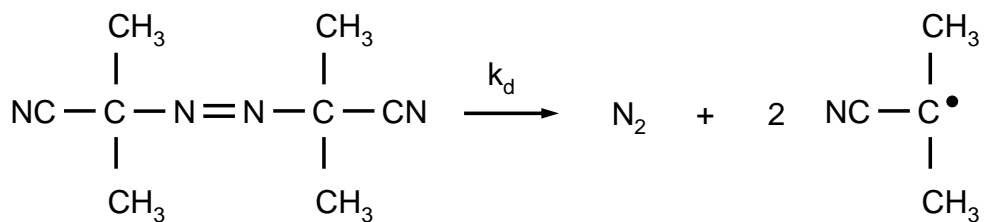
Free-Radical Polymerization

1.1 Chemical Reactions

1.1.1 Initiation

The initiation reaction produces free radicals. There are several ways to do this:

- Chemical initiation The decomposition of the initiator (e.g. AIBN) forms free radicals:



$$\frac{dI^\bullet}{dt} = 2fk_d I_2 - k_l I^\bullet M \approx 0 \quad (1.1)$$

$$\Rightarrow k_l I^\bullet M = 2fk_d I_2 \equiv R_I \quad (1.2)$$

where f is the initiator efficiency, typically $f = [0.5, 1]$. Note that in order to ensure a continuous production of radicals all over the process, $1/k_d$ should be larger than the characteristic time of the polymerization reaction. Examples of the decomposition characteristic time, τ_d for some commercial initiators are:

CHAPTER 1. FREE-RADICAL POLYMERIZATION

	τ_d	T
Acetyl peroxide	2 h	80 °C
Cumyl peroxide	12 h	110 °C
<i>t</i> -Butyl hydroperoxide	45 h	150 °C

Since this is a first order process, $\tau_d = 1/k_d$.

- Thermal initiation: thermal decomposition of the monomer (e.g. styrene).

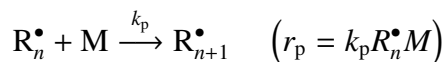
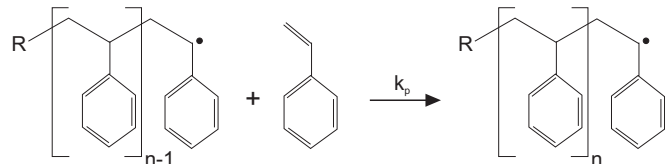
This represents a danger, for example during monomer transportation, since it may lead to undesired polymerization of the monomer. For this reason, inhibitors (scavengers of radicals) are usually added to the monomers before storage. This causes the occurrence of a non reproducible induction period when such monomers are polymerized.

- Initiation by radiation

The decomposition of the initiator is caused by light or another source of radiation. Since this method is quite expensive, it is only applied to polymerization systems operating at very low temperatures.

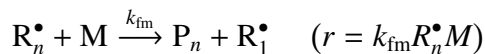
1.1.2 Propagation

Propagation is the addition of a monomer molecule to a radical chain.



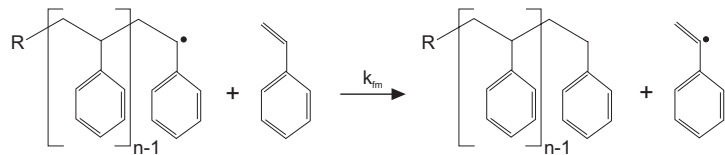
1.1.3 Chain Transfer

- Chain transfer to monomer



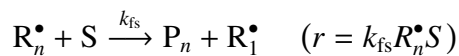
The reactants are the same as for the propagation reaction, but the activation energy is much larger. Accordingly, k_{fm} is usually at least 10^3 times smaller than k_p . This reaction

CHAPTER 1. FREE-RADICAL POLYMERIZATION



leads to the formation of a polymer chain with a terminal double bond. This can induce chain branching through the terminal double bond propagation reaction.

- Chain transfer to chain transfer agent



A chain transfer agent, S is a molecule containing a weak bond that can be broken to lead to radical transfer, similarly as in the case of monomer above (e.g. CCl_4 , CBr_4 , mercaptans).

- Chain transfer to polymer



In this reaction the growing radical chain, R_n^\bullet extracts a hydrogen from the dead chain, P_m . Since this extraction can occur on any of the m monomer units along the chain, the rate of this reaction is proportional to the length of P_m .

General observations on the role of chain transfer reactions:

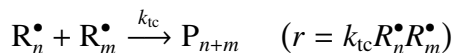
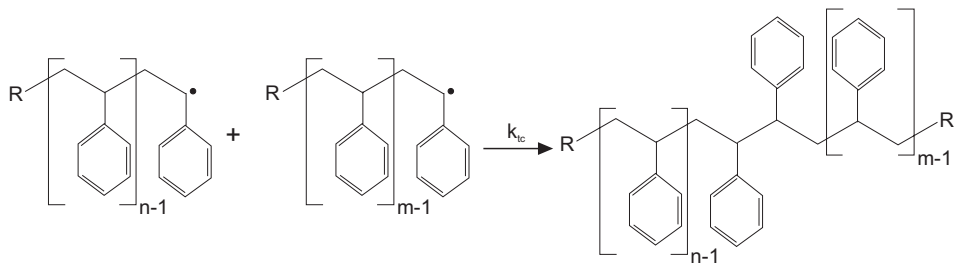
- The concentration of radicals is not affected and therefore the rate of monomer consumption is also unchanged.
- The growth of polymer chains is stopped and therefore shorter chains are produced.
- Each transfer event leaves a different end-group on the chain that can be detected (NMR, titration) so as to identify and quantify the corresponding chain transfer reaction.
- Nonlinear (branched) polymer chains are produced: directly by chain transfer to polymer or indirectly through the propagation of the terminal double bond left by a chain transfer to monomer event.

CHAPTER 1. FREE-RADICAL POLYMERIZATION

1.1.4 Bimolecular Termination

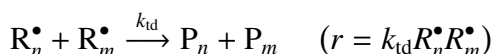
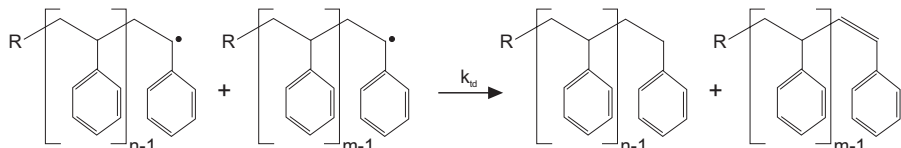
Bimolecular termination occurs according to two different mechanisms: termination by combination and termination by disproportionation. Their relative importance depends upon the specific polymerization system.

- Termination by combination



This reaction results in an increase of the chain length.

- Termination by disproportionation



The chain length remains constant during the termination reaction. Note that also in this case chains with terminal double bond are produced, which can therefore lead to the occurrence of branching.

1.2 Diffusion Control of Chemical Reactions

When dealing with macromolecules we can regard the reaction event as constituted by two steps in series:

CHAPTER 1. FREE-RADICAL POLYMERIZATION

- a relative motion or diffusion of the two molecules in order to overlap their active centers (note that the centers of gravity of the two macromolecules already overlap, i.e., we have no mass transport involved)
- the reaction event per se, i.e., breakage and formation of chemical bonds.

Since the two steps are in series, the slowest one defines the rate of the overall process, that is the reaction rate.

In the case of termination by combination, the reaction step is very fast, while the diffusion step is slow due to the difficulty of the two macromolecules to find their respective active centers (the two chains exhibit strong entanglements). The result is that diffusion is the rate determining step. Accordingly the rate constant of termination by combination, k_{tc} has the following characteristics:

- decreases with viscosity (and therefore with conversion)
- increases very mildly with temperature
- is substantially independent of the chemical nature of the radicals.

This effect is usually referred to as *Trommsdorf* or *gel effect*. This is responsible for the accumulation of radicals during the reaction which can also lead to thermal runaway of the reactor.

Let us now consider the other involved reactions. It is found that in most cases they are not diffusion controlled for the following reasons:

- termination by disproportionation: the reaction step is slower (can still be diffusion controlled)
- chain transfer to polymer: reaction is slower and diffusion is faster since we have many reactive points along the chain.
- propagation: reaction is slower and diffusion much faster due to the small dimension of the monomer (this reaction stops below the glass transition temperature)

1.3 Polymerization Processes

1.3.1 Bulk Polymerization

- ingredients: monomer and initiator only
- products: high purity
- disadvantage: poor temperature control at high conversion (thermal runaway!)

1.3.2 Solution Polymerization

- ingredients: solvent, monomer and initiator
- guarantees an efficient heat transfer
- disadvantage: low productivity because of low solubility of the produced polymer

1.3.3 Suspension Polymerization

- ingredients: water, monomer, initiator and stabilizer
- size of formed polymer particles approx. $0.01 - 0.5 \text{ cm}$
- initiator is solubilized in monomer phase
- polymerization occurs within the monomer droplets
- high productivity ($> 40\% \text{ solid}$)
- heat production is under control

1.3.4 Emulsion Polymerization

- ingredients: water, monomer, initiator and stabilizer
- size of formed polymer particles approx. $0.05 - 1 \mu\text{m}$
- initiator is solubilized in water phase
- polymerization occurs mainly within the polymer particles

- high productivity (> 40 % solid)
- heat production is under control
- advantage: high molecular weight as well as high polymerization rate can be achieved simultaneously

1.4 Kinetics of Free-Radical Polymerization

1.4.1 Involved Chemical Reactions

Initiation	$I_2 \longrightarrow 2 R_1^\bullet$	$r = 2fk_dI_2 \equiv R_I$
Propagation	$R_n^\bullet + M \xrightarrow{k_p} R_{n+1}^\bullet$	$r = k_pMR_n^\bullet$
Chain Transfer	$R_n^\bullet + M \xrightarrow{k_{fm}} R_1^\bullet + P_n$	$r = k_{fm}MR_n^\bullet$
	$R_n^\bullet + S \xrightarrow{k_{fs}} R_1^\bullet + P_n$	$r = k_{fs}SR_n^\bullet$
	$R_n^\bullet + P_m \xrightarrow{k_{fp}} R_m^\bullet + P_n$	$r = k_{fp}R_n^\bullet(mP_m)$
Termination	$R_n^\bullet + R_m^\bullet \xrightarrow{k_{tc}} P_{n+m}$	$r = k_{tc}R_n^\bullet R_m^\bullet$
	$R_n^\bullet + R_m^\bullet \xrightarrow{k_{td}} P_n + P_m$	$r = k_{td}R_n^\bullet R_m^\bullet$

where $n, m = [1\dots\infty]$

Note that all reaction rate constants are assumed to be chain length independent, i.e., we use the Terminal Kinetic Model.

1.4.2 Population Balance Equations in a Batch Reactor

- $n=1$:

$$\begin{aligned} \frac{dR_1^\bullet}{dt} &= R_I - k_pMR_1^\bullet \\ &+ (k_{fm}M + k_{fs}S) \sum_{n=2}^{\infty} R_n^\bullet \\ &+ k_{fp} (1P_1) \sum_{n=1}^{\infty} R_n^\bullet - \left[k_{fp} \sum_{n=1}^{\infty} (nP_n) \right] R_1^\bullet \\ &- (k_{tc} + k_{td}) \left[\sum_{n=1}^{\infty} R_n^\bullet \right] R_1^\bullet \end{aligned} \quad (1.3)$$

- $n \geq 2$:

$$\begin{aligned} \frac{dR_n^\bullet}{dt} &= k_p M R_{n-1}^\bullet - k_p M R_n^\bullet \\ &\quad - (k_{fm} M + k_{fs} S) R_n^\bullet \\ &\quad + k_{fp} (nP_n) \sum_{m=1}^{\infty} R_m^\bullet - k_{fp} \sum_{m=1}^{\infty} (mP_m) R_n^\bullet \\ &\quad - (k_{tc} + k_{td}) \left[\sum_{m=1}^{\infty} R_m^\bullet \right] R_n^\bullet \end{aligned} \quad (1.4)$$

Let us define

$$R^\bullet \equiv \sum_{n=1}^{\infty} R_n^\bullet \quad (1.5)$$

and sum up equations (1.3) and (1.4) from $n = 1$ to ∞ . In this way we obtain:

$$\begin{aligned} \frac{dR^\bullet}{dt} &= \frac{dR_1^\bullet}{dt} + \sum_{n=2}^{\infty} \frac{dR_n^\bullet}{dt} \\ &= R_I - k_p M R_1^\bullet + k_p M \sum_{n=2}^{\infty} R_{n-1}^\bullet - k_p M \sum_{n=2}^{\infty} R_n^\bullet \\ &\quad + (k_{fm} M + k_{fs} S) \sum_{n=2}^{\infty} R_n^\bullet - (k_{fm} M + k_{fs} S) \sum_{n=2}^{\infty} R_n^\bullet \\ &\quad + k_{fp} (1P_1) \sum_{n=1}^{\infty} R_n^\bullet - k_{fp} \left[\sum_{n=1}^{\infty} (nP_n) \right] R_1^\bullet \\ &\quad + k_{fp} \sum_{n=2}^{\infty} [nP_n] \sum_{m=1}^{\infty} R_m^\bullet - k_{fp} \left[\sum_{n=2}^{\infty} R_n^\bullet \right] \left[\sum_{m=1}^{\infty} (mP_m) \right] \\ &\quad - (k_{tc} + k_{td}) R_1^\bullet \sum_{n=1}^{\infty} R_n^\bullet - (k_{tc} + k_{td}) \left[\sum_{n=2}^{\infty} R_n^\bullet \right] \left[\sum_{m=1}^{\infty} R_m^\bullet \right] \end{aligned} \quad (1.6)$$

$$\begin{aligned} \frac{dR^\bullet}{dt} &= R_I - k_p M R^\bullet + k_p M \sum_{n=1}^{\infty} R_n^\bullet \\ &\quad + k_{fp} R^\bullet \left[P_1 + \sum_{n=2}^{\infty} (nP_n) \right] - k_{fp} \left[\sum_{n=1}^{\infty} (nP_n) \right] \left[R_1^\bullet + \sum_{n=2}^{\infty} R_n^\bullet \right] \\ &\quad - (k_{tc} + k_{td}) R^\bullet \left[R_1^\bullet + \sum_{n=2}^{\infty} R_n^\bullet \right] \end{aligned} \quad (1.7)$$

$$\Rightarrow \frac{dR^\bullet}{dt} = R_I - (k_{tc} + k_{td}) R^{\bullet 2} \quad (1.8)$$

1.4.3 Rate of Monomer Consumption

Under the assumption of pseudo steady state for the concentration of active chains (see 1.5) we can write:

$$\frac{dR^\bullet}{dt} = R_I - (k_{tc} + k_{td}) R^{\bullet 2} = 0 \quad (1.9)$$

and obtain:

$$R^\bullet = \sqrt{\frac{R_I}{(k_{tc} + k_{td})}} \quad (1.10)$$

Let us now consider the rate of monomer consumption, R_p . Neglecting the chain transfer to monomer reaction we have:

$$R_p = k_p M \sum_{n=1}^{\infty} R_n^\bullet = k_p M \sqrt{\frac{R_I}{(k_{tc} + k_{td})}} \quad (1.11)$$

The mass balance for the monomer can be written as follows (still in the case of a batch reactor):

$$\frac{dM}{dt} = -R_p = -k_p M R^\bullet \quad (1.12)$$

Considering $k_p R^\bullet$ as the pseudo-first order reaction rate constant for monomer consumption, we can conclude that the characteristic time for the process of monomer consumption is $\tau_M = \frac{1}{k_p R^\bullet}$. Using the conversion instead of the concentration, $X = (M_0 - M) / M_0$, and combining equation (1.11) and (1.12) we get:

$$\frac{dX}{dt} = -\frac{1}{M_0} \frac{dM}{dt} = \frac{R_p}{M_0} = (1 - X) k_p \sqrt{\frac{R_I}{(k_{tc} + k_{td})}} \quad (1.13)$$

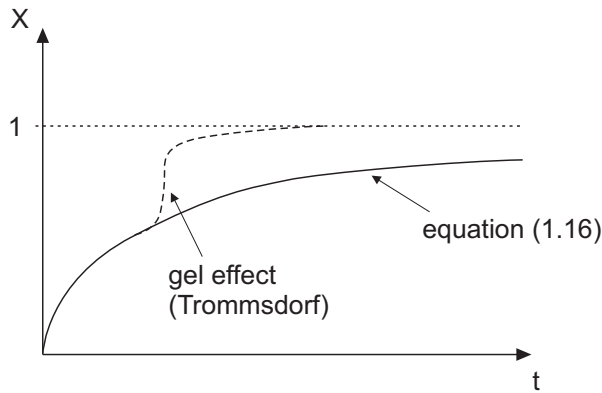
$$\frac{dX}{(1 - X)} = k_p \sqrt{\frac{R_I}{(k_{tc} + k_{td})}} dt \quad (1.14)$$

where the initial condition is $X(t = 0) = 0$. Therefore we can write:

$$X = 1 - \exp \left[- \int_0^t k_p \sqrt{\frac{R_I}{(k_{tc} + k_{td})}} \cdot dt \right] \quad (1.15)$$

As long as the temperature in the reactor remains constant, i.e., before the onset of the so-called gel effect, k_{tc} and k_{td} are independent of the conversion X . Moreover, if the half-life of the initiator is much larger than the characteristic time of the monomer consumption process, $\tau_M, \tau_d \gg \tau_M$, the solution to equation (1.15) is:

$$X = 1 - \exp \left[-k_p \sqrt{\frac{R_I}{(k_{tc} + k_{td})}} \cdot t \right] \quad (1.16)$$



- Which kinetic parameter(s) can be estimated from the plot of the monomer conversion vs. time?

1.5 Pseudo Steady State Approximation

In this section we introduce an important concept often used in chemical reaction engineering, the so-called pseudo steady state approximation (PSSA). Therefore, let us consider two consecutive first-order reactions occurring in a batch reactor:



with initial conditions $I(0) = I_0$, $R(0) = R_0$ and $P(0) = 0$. The mass balances are:

$$\frac{dI}{dt} = -k_1 I \quad (1.17)$$

$$\frac{dR}{dt} = k_1 I - k_2 R \quad (1.18)$$

The solution of equation (1.17) is:

$$I = I_0 \exp(-k_1 t) \quad (1.19)$$

which substituted in equation (1.18) leads to a linear non-homogeneous ODE. We consider the solution of the homogeneous associated equation:

$$R^H = A \exp(-k_2 t) \quad (1.20)$$

CHAPTER 1. FREE-RADICAL POLYMERIZATION

and then the particular solution having the form:

$$R^P = K \exp(-k_1 t) \quad (1.21)$$

Substituting in equation (1.18) we get:

$$-k_1 K \exp(-k_1 t) = k_1 I_0 \exp(-k_1 t) - k_2 K \exp(-k_1 t) \quad (1.22)$$

$$\Rightarrow k_1 K + k_1 I_0 - k_2 K = 0 \quad (1.23)$$

$$\Rightarrow K = \frac{k_1 I_0}{k_2 - k_1} \quad (1.24)$$

Thus the general solution is:

$$R = R^H + R^P = A \exp(-k_2 t) + \frac{k_1 I_0}{k_2 - k_1} \exp(-k_1 t) \quad (1.25)$$

which using the initial condition to compute A reduces to:

$$R = \left(R_0 - \frac{k_1 I_0}{k_2 - k_1} \right) \exp(-k_2 t) + \frac{k_1 I_0}{k_2 - k_1} \exp(-k_1 t) \quad (1.26)$$

Let us now consider the case where R is a very reactive species, that is $k_2 \gg k_1$, then equation (1.26) reduces to:

$$R = \frac{k_1 I_0}{k_2} \exp(-k_1 t) = \frac{k_1}{k_2} I \quad (1.27)$$

This means that R starts at R_0 and after a short time of the order of $1/k_2$ the term $\exp(-k_2 t)$ vanishes and $R = k_1 I / k_2$ as shown in the figure.

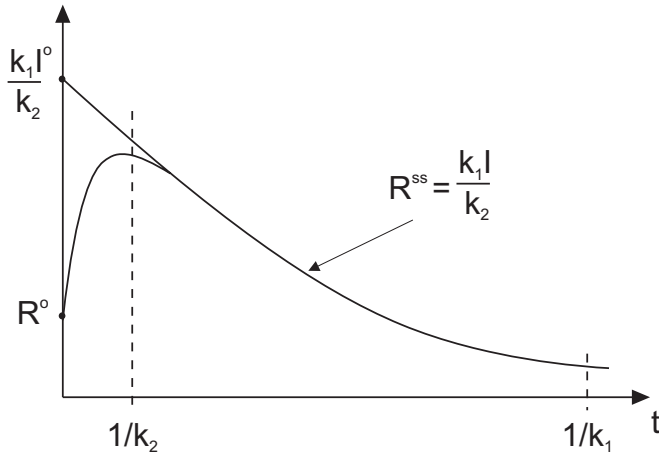
We see two time scales in the process:

- $1/k_2$: characteristic time of disappearance for $R \Rightarrow$ fast
- $1/k_1$: characteristic time of disappearance for $I \Rightarrow$ slow

Since the dynamics of R is faster than that of I , we can assume that R is at any given time at steady state with respect to I , i.e., R is so fast to reach steady state before I can change significantly. This is the PSSA, which means that we can assume $dR/dt = 0$ in equation (1.18), and compute the PSSA value of R :

$$R^{ss} = \frac{k_1}{k_2} I \quad (1.28)$$

which is the same value given by equation (1.27).



Note

In the PSSA we do not mean that $dR/dt = 0$, and in fact in the case above we see that:

$$\frac{dR^{ss}}{dt} = -\frac{k_1^2 I_0}{k_2} \exp(-k_1 t) = -\frac{k_1^2}{k_2} I \quad (1.29)$$

Actually we simply mean that

$$\frac{dR^{ss}}{dt} \ll k_1 I \quad \text{and} \quad \frac{dR^{ss}}{dt} \ll k_2 R^{ss} \quad (1.30)$$

as it is readily seen by comparison noting that $k_1/k_2 \ll 1$.

Another Point of View

Let us rewrite equation (1.18) as follows:

$$\frac{dR}{dt} = k_2 \left(\frac{k_1}{k_2} I - R \right) = k_2 (R^{ss} - R) \quad (1.31)$$

We can observe that:

$$\begin{aligned} \text{if } R > R^{ss} &\Rightarrow dR/dt < 0 \Rightarrow R \text{ decreases} \\ \text{if } R < R^{ss} &\Rightarrow dR/dt > 0 \Rightarrow R \text{ increases} \end{aligned}$$

which means that R remains always “around” R^{ss} . Note that this is not true in general, but only in the case where k_2 is very large we have that the “force” attracting R to R^{ss} increases up to the point where R cannot differ significantly from R^{ss} .

Conclusion

The PSSA can be applied when we have very different characteristic times, typically when the intermediate species is very reactive, i.e., $k_2 \gg k_1$. The obtained solution is valid for most of the process time, with the exception of a short initial transient. We have two characteristic times:

- the fast one ($1/k_2$) which belongs to R and where I does not change significantly
- the slow one ($1/k_1$) which belongs to I and determines the process time, that is the time needed by the slowest species to complete its dynamics.

With respect to numerical integration this has important implications:

- the integration time is given by the process time, i.e., $\tau_p \approx 1/k_1$
- the integration step is proportional to the characteristic time of the fastest dynamics that we want to follow, i.e., $\Delta\tau \approx 1/k_2$
- the number of integration steps is proportional to $\tau_p/\Delta\tau \approx k_2/k_1$ which means that the larger is k_2/k_1 the more we are entitled to use PSSA ... and the more integration steps we have to compute if we fail to use it.

1.5.1 Stiffness Ratio

In general, for a system of ODEs the ratio between the largest and the smallest eigenvalue is referred to as the stiffness ratio of the system. This gives a measure of the difficulty in integrating a system of ODEs numerically. The coefficient matrix of the system of ODEs, defined as:

$$\frac{d\underline{x}}{dt} = \underline{\underline{A}} \underline{x} \quad (1.32)$$

in our case is given by:

$$\underline{\underline{A}} = \begin{vmatrix} -k_1 & 0 \\ k_1 & -k_2 \end{vmatrix} \quad \text{with } \underline{x} = \begin{vmatrix} I \\ R \end{vmatrix} \quad (1.33)$$

The eigenvalues of $\underline{\underline{A}}$ are given by:

$$\begin{aligned} (-k_1 - \lambda)(-k_2 - \lambda) &= 0 \\ \Rightarrow \lambda_1 &= -k_1, \quad \lambda_2 = -k_2 \end{aligned}$$

and the stiffness ratio is then given by:

$$\frac{\lambda_2}{\lambda_1} = \frac{k_2}{k_1} \quad (1.34)$$

which, as discussed above, is proportional to the integration steps to be used in the numerical integration of the system of ODEs.

Chapter 2

Chain Length Distribution of Polymers

2.1 Population Balance Equations

In the following we concentrate on linear chains only which means $k_{fp} = 0$ and no propagation of the terminal double bond.

2.1.1 Active Chains

Under the assumption of pseudo steady state for species R_1^\bullet ,

$$\frac{dR_1^\bullet}{dt} = 0 \quad (2.1)$$

we can set equation (1.3) equal to zero:

$$R_I + (k_{fm}M + k_{fs}S)(R^\bullet - R_1^\bullet) = k_p M R_1^\bullet + (k_{tc} + k_{td}) R^\bullet R_1^\bullet \quad (2.2)$$

Solving for R_1^\bullet we obtain:

$$R_1^\bullet = \frac{R_I + (k_{fm}M + k_{fs}S)R^\bullet}{k_p M + (k_{tc} + k_{td})R^\bullet + (k_{fm}M + k_{fs}S)} \quad (2.3)$$

Since R_I is given by equation (1.10):

$$R_I = (k_{tc} + k_{td})R^{\bullet 2} \quad (2.4)$$

we can simplify equation (2.3) as follows:

$$R_1^\bullet = R^\bullet \frac{\alpha}{1 + \alpha} \quad (2.5)$$

where α is the summation of various characteristic time ratios:

$$\begin{aligned} \alpha &= \frac{k_{tc}R^\bullet}{k_p M} + \frac{k_{td}R^\bullet}{k_p M} + \frac{k_{fm}M}{k_p M} + \frac{k_{fs}S}{k_p M} \\ &= \frac{\tau_p}{\tau_{tc}} + \frac{\tau_p}{\tau_{td}} + \frac{\tau_p}{\tau_{fm}} + \frac{\tau_p}{\tau_{fs}} \end{aligned} \quad (2.6)$$

where τ_p is the characteristic time of the addition reaction of a single monomer unit, while the τ at the denominator are the characteristic times of the chain transfer and the termination reactions involved in the system. The order of magnitude of these characteristic times, which refer to second-order processes, can be computed using pseudo-first order reaction approximation. So far the monomer addition reaction, $r = k_p M R_n^\bullet$ and the pseudo-first order rate constant is $k_p M$, so that $\tau_p = \frac{1}{k_p M}$. In most applications, we have that $\tau_p \approx 10^{-3}$ s while termination reactions (or at least the dominating one) has τ_f or $\tau_t \approx 10^0$ s. This means that a polymer chain leaves about 1 s and in this time it adds about 10^3 monomer units. Note that the characteristic time of the process is that of monomer consumption, $\tau_M = \frac{1}{k_p R^\bullet}$ which is of the order of 10^3 s. These are the three time scales dominating the process under examination. From equation (2.5) we can see that for $\alpha \ll 1 \Rightarrow R_1^\bullet \ll R^\bullet$, as expected.

If we apply the pseudo steady state assumption now to the species R_n^\bullet ($n \geq 2$), we can write:

$$\frac{dR_n^\bullet}{dt} = 0 \quad (2.7)$$

$$k_p M R_{n-1}^\bullet = [k_p M + k_{fm} M + k_{fs} S + (k_{tc} + k_{td}) R^\bullet] R_n^\bullet \quad (2.8)$$

$$\Rightarrow R_n^\bullet = R_{n-1}^\bullet \Phi \quad (2.9)$$

where

$$\Phi = \frac{1}{1 + \alpha} \quad (2.10)$$

Therefore we obtain:

$$R_n^\bullet = R_{n-1}^\bullet \Phi = R_{n-2}^\bullet \Phi^2 = \dots = R_1^\bullet \Phi^{n-1} \quad (2.11)$$

and using equation (2.5):

$$R_n^\bullet = \frac{1}{(1 + \alpha)^{n-1}} R^\bullet \frac{\alpha}{1 + \alpha} = R^\bullet \frac{\alpha}{(1 + \alpha)^n} \quad (2.12)$$

Thus, we can consolidate the two cases ($n = 1$ and $n \geq 2$) and write the general expression for $n \geq 1$:

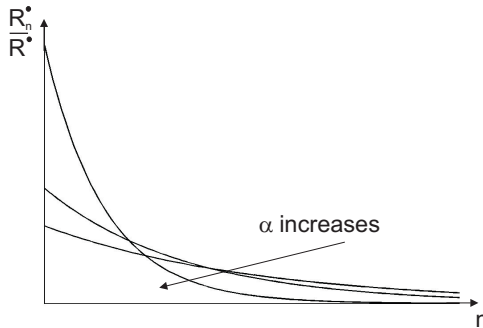
$$R_n^\bullet = R^\bullet \frac{\alpha}{(1 + \alpha)^n} \quad (2.13)$$

Note

- equation (2.13) can be simplified if $\alpha \ll 1$:

$$\frac{1}{(1 + \alpha)^n} \approx \exp(-\alpha n) \quad \text{for } \alpha \ll 1 \quad (2.14)$$

$$\Rightarrow \frac{R_n^{\bullet}}{R^{\bullet}} \approx \alpha \exp(-\alpha n) \quad (2.15)$$



- $\int_0^\infty \frac{R_n^{\bullet}}{R^{\bullet}} dn = \int_0^\infty \alpha \exp(-\alpha n) dn = \alpha \left| -\frac{\exp(-\alpha n)}{\alpha} \right|_0^\infty = 1$

To summarize, we can state that the distribution of active chains is normalized and, moreover, it is characterized by only one kinetic parameter α defined by equation (2.6).

2.1.2 Dead Chains

$$\frac{dP_n}{dt} = (k_{fm}M + k_{fs}S + k_{td}R^{\bullet})R_n^{\bullet} + \frac{1}{2}k_{tc} \sum_{j=1}^{n-1} R_j^{\bullet}R_{n-j}^{\bullet} \quad (2.16)$$

Here we can write:

$$\frac{1}{2}k_{tc} \sum_{j=1}^{n-1} R_j^{\bullet}R_{n-j}^{\bullet} = \begin{cases} \frac{1}{2}(R_1^{\bullet}R_2^{\bullet} + R_2^{\bullet}R_1^{\bullet}) = R_1^{\bullet}R_2^{\bullet} & (n = 3) \\ \frac{1}{2}(R_1^{\bullet}R_3^{\bullet} + R_2^{\bullet}R_2^{\bullet} + R_3^{\bullet}R_1^{\bullet}) = R_1^{\bullet}R_3^{\bullet} + \frac{1}{2}R_2^{\bullet}R_2^{\bullet} & (n = 4) \\ \frac{1}{2}(R_1^{\bullet}R_4^{\bullet} + R_2^{\bullet}R_3^{\bullet} + R_3^{\bullet}R_2^{\bullet} + R_4^{\bullet}R_1^{\bullet}) = R_1^{\bullet}R_4^{\bullet} + R_2^{\bullet}R_3^{\bullet} & (n = 5) \end{cases} \quad (2.17)$$

CHAPTER 2. CHAIN LENGTH DISTRIBUTION OF POLYMERS

If we use equation (2.13) to express R_n^\bullet , we obtain for the sum term:

$$\begin{aligned} k_{tc} \sum_{j=1}^{n-1} R_j^\bullet R_{n-j}^\bullet &= k_{tc} \sum_{j=1}^{n-1} \left[\left(R^\bullet \frac{\alpha}{(1+\alpha)^j} \right) \left(R^\bullet \frac{\alpha}{(1+\alpha)^{n-j}} \right) \right] \\ &= k_{tc} \frac{R^\bullet 2 \alpha^2}{(1+\alpha)^n} \sum_{j=1}^{n-1} (1) \\ &= k_{tc} \frac{\alpha^2 (n-1)}{(1+\alpha)^n} R^\bullet 2 \end{aligned} \quad (2.18)$$

Therefore we can rewrite equation (2.16) as follows:

$$\frac{dP_n}{dt} = (k_{fm}M + k_{fs}S + k_{td}R^\bullet) \frac{\alpha}{(1+\alpha)^n} R^\bullet + \frac{1}{2} k_{tc} \frac{\alpha^2 (n-1)}{(1+\alpha)^n} R^\bullet 2 \quad (2.19)$$

where we see that α alone is not anymore sufficient to fully describe the distribution, and we have to introduce further parameters:

$$\frac{dP_n}{dt} = \left(k_p M R^\bullet \right) \left[\left(\frac{k_{fm}}{k_p} + \frac{k_{fs}}{k_p M} + \frac{k_{td}}{k_p M} R^\bullet \right) \frac{\alpha}{(1+\alpha)^n} + \left(\frac{k_{tc} R^\bullet}{k_p M} \right) \frac{1}{2} \frac{\alpha^2 (n-1)}{(1+\alpha)^n} \right] \quad (2.20)$$

The introduced parameters are defined as follows:

$$\gamma = \frac{k_{fm}}{k_p} + \frac{k_{fs}}{k_p M} + \frac{k_{td}}{k_p M} R^\bullet = \frac{\tau_p}{\tau_{fm}} + \frac{\tau_p}{\tau_{fs}} + \frac{\tau_p}{\tau_{td}} \quad (2.21)$$

$$\beta = \frac{k_{tc} R^\bullet}{k_p M} = \frac{\tau_p}{\tau_{tc}} \quad (2.22)$$

where

$$\alpha = \beta + \gamma \quad (2.23)$$

Finally, we obtain for $n \geq 1$:

$$\frac{dP_n}{dt} = R_p \frac{\alpha}{(1+\alpha)^n} \left[\gamma + \frac{1}{2} (n-1) \alpha \beta \right] \quad (2.24)$$

Comparing equations (2.13) and (2.24) it is easy to see that in the case of active chain distribution only the ratio between the characteristic times of propagation and termination is relevant. On the other hand, dealing with the dead chain distribution we have to distinguish between two different types of chain reactions: chain transfers and disproportionation on one side, and combination on the other side.

The question is: what is the conceptual difference between these reactions which makes them to play a different role in determining the chain length distribution?

2.2 Instantaneous Chain Length Distribution

In the following section we consider the instantaneous CLD of polymer chains. Different distributions can be introduced.

2.2.1 Number Distribution and Number Average

The instantaneous CLD or number distribution is defined as follows:

$$f_N(n) = \frac{\text{polymer chains of length } n}{\text{total number of polymer chains}} = \frac{\frac{dP_n}{dt}}{\sum_{n=1}^{\infty} \frac{dP_n}{dt}} \quad (2.25)$$

Note that this is an instantaneous property, that is it represents the CLD of the infinitesimal amount of polymer produced at a given time. Using equation (2.24) we obtain:

$$f_N(n) = \frac{\frac{\gamma + \frac{1}{2}(n-1)\beta(\beta+\gamma)}{(1+\alpha)^n}}{\sum_{n=1}^{\infty} \left[\frac{\gamma + \frac{1}{2}(n-1)\beta(\beta+\gamma)}{(1+\alpha)^n} \right]} \quad (2.26)$$

Since the following equality holds for geometric series

$$\sum_{n=1}^{\infty} (a + nb) q^n = \frac{aq}{(1-q)} + \frac{bq}{(1-q)^2} \quad \text{for } |q| < 1 \quad (2.27)$$

we can rewrite the denominator in equation (2.26) as follows:

$$\begin{aligned} & \sum_{n=1}^{\infty} \left[\gamma - \frac{1}{2}\beta(\beta+\gamma) \right] \left(\frac{1}{1+\alpha} \right)^n + \sum_{n=1}^{\infty} n \left[\frac{1}{2}\beta(\beta+\gamma) \right] \left(\frac{1}{1+\alpha} \right)^n \\ &= \left[\gamma - \frac{1}{2}\beta(\beta+\gamma) \right] \left(\frac{1}{\alpha} \right) + \frac{1}{2}\beta(\beta+\gamma) \left(\frac{1+\alpha}{\alpha^2} \right) \end{aligned} \quad (2.28)$$

and since $\alpha = \beta + \gamma$

$$= \gamma \left(\frac{1}{\alpha} \right) - \frac{1}{2}\beta + \frac{1}{2}\beta \left(\frac{1+\alpha}{\alpha} \right) = \frac{1}{\alpha} \left(\gamma + \frac{1}{2}\beta \right) \quad (2.29)$$

Finally, we obtain for equation (2.26):

$$f_N(n) = \frac{\alpha}{(1+\alpha)^n} \left[\frac{\gamma + \frac{1}{2}(n-1)\beta(\beta+\gamma)}{\gamma + \frac{1}{2}\beta} \right] \quad (2.30)$$

By definition holds:

$$\sum_{n=1}^{\infty} f_N(n) = 1 \quad (2.31)$$

Let us focus now on the moments of this distribution. In particular, the j -th order moment of $f_N(n)$ is defined as follows:

$$\mu_j = \sum_{n=1}^{\infty} n^j f_N(n) \quad (2.32)$$

From the first two moments we can calculate the number average of the CLD:

$$\bar{n}_N = \frac{\mu_1}{\mu_0} \approx \frac{1}{\gamma + \frac{1}{2}\beta} \text{ for } \alpha \ll 1 \quad (2.33)$$

which, when multiplied by the molecular weight of the monomer, M_M , leads to the so-called *number average molecular weight*:

$$M_N = \frac{\mu_1}{\mu_0} M_M \quad (2.34)$$

2.2.2 Weight Distribution and Weight Average

Another way to characterize the distribution of the polymer chains is the so-called instantaneous weight distribution:

$$f_W(n) = \frac{\text{number of monomer units in the chains of length } n}{\text{total amount of consumed monomer}} = \frac{n \cdot dP_n}{R_p} \quad (2.35)$$

or expressed in terms of f_N :

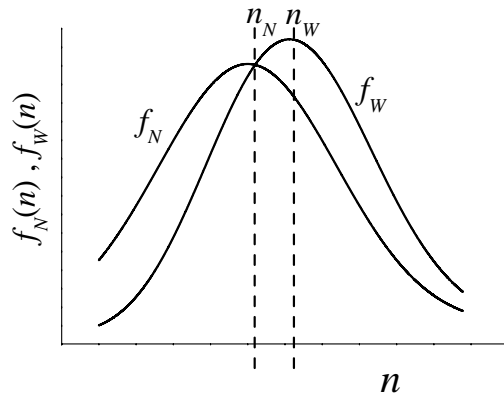
$$f_W(n) = \frac{n f_N(n)}{\sum_1^{\infty} n f_N(n)} = \frac{n f_N(n)}{\mu_1} \quad (2.36)$$

If we compute the mean of this distribution we obtain the weight average of the CLD:

$$\bar{n}_W = \frac{1}{\mu_1} \sum_1^{\infty} n^2 f_N(n) = \frac{\mu_2}{\mu_1} \quad (2.37)$$

Note that the moments used in the last two expressions refer to f_N . Using equations (2.30) and (2.36) we obtain:

$$\bar{n}_W \approx \frac{2(\gamma + \frac{3}{2}\beta)}{(\gamma + \beta)^2} \text{ for } \alpha \ll 1 \quad (2.38)$$



which, when multiplied by the molecular weight of the monomer, M_M , leads to the so-called *weight average molecular weight*:

$$M_w = \frac{\mu_2}{\mu_1} M_M \quad (2.39)$$

To summarize, we defined two different means \bar{n}_N and \bar{n}_w of only one distribution f_N . The reason for this is given in the following subsection.

2.2.3 Polydispersity

The polydispersity index (PDI) is a widely used quantity to characterize distributions in general and the CLD in particular. This is defined as follows:

$$\sigma = \frac{\bar{n}_w}{\bar{n}_N} \geq 1 \quad (2.40)$$

$$\Rightarrow \sigma = \frac{\mu_2/\mu_1}{\mu_1/\mu_0} = \frac{\mu_2\mu_0}{\mu_1^2} \quad (2.41)$$

Thus, $\sigma = 1$ means that all chains have exactly the same length. The polydispersity index describes the width of a distribution and is therefore an alternative way to represent its variance v :

$$\begin{aligned} v &= \sum_{n=1}^{\infty} (n - \bar{n}_N)^2 f_N(n) = \mu_2 - 2\mu_1\bar{n}_N + \bar{n}_N^2\mu_0 \\ &= \mu_2 - 2\frac{\mu_1^2}{\mu_0} + \frac{\mu_1^2}{\mu_0^2}\mu_0 = \mu_2 - \frac{\mu_1^2}{\mu_0} \\ &= \frac{\mu_1^2}{\mu_0}(\sigma - 1) \end{aligned} \quad (2.42)$$

Note that $v = 0$ corresponds to $\sigma = 1$. The usage of the polydispersity to characterize the width of CLD of polymers is justified by the fact that equation (2.40) is particularly convenient in practice. We have in fact various techniques available that can measure either the number average or the weight average of polymer chains.

2.2.4 Summary

For the reaction scheme of the free-radical polymerization system described in section 1.4.1 we can write the following relationships for the instantaneous properties of the CLD (if $\alpha \ll 1$):

$$\bar{n}_N = \frac{1}{\gamma + \frac{\beta}{2}} \quad (2.43)$$

$$\bar{n}_W = \frac{2(\gamma + \frac{3}{2}\beta)}{(\gamma + \beta)^2} \quad (2.44)$$

$$\sigma = \frac{2(\gamma + \frac{3}{2}\beta)(\gamma + \frac{1}{2}\beta)}{(\gamma + \beta)^2} \quad (2.45)$$

Chapter 3

Cumulative Properties of Polymers

3.1 Cumulative Chain Length Distribution, Moments, and Properties

In order to compute the cumulative number-CLD, $f_N^c(n)$ from the instantaneous one, $f_N(n)$ we use the following relation:

$$f_N^c(n, t) = \frac{1}{P(t)} \underbrace{\int_0^t f_N(n, t) \left(\frac{dP}{dt} \right) dt}_{\text{total number of polymer chains of length } n \text{ produced until time } t} \overbrace{\quad}^{\text{number of polymer chains of length } n \text{ produced per unit time}} \quad (3.1)$$

which multiplying both sides by n^j and summing for $n = 1$ to ∞ gives the following expression for the moments of the cumulative distribution:

$$\sum_{n=1}^{\infty} n^j \cdot f_N^c(n, t) = \frac{1}{P(t)} \int_0^t \sum_{n=1}^{\infty} \left(n^j \cdot f_N(n, t) \frac{dP}{dt} \right) dt \quad (3.2)$$

which leads to:

$$\mu_j^c = \frac{1}{P(t)} \int_0^t \mu_j \left(\frac{dP}{dt} \right) dt = \frac{1}{P(t)} \int_0^{P(t)} \mu_j dP \quad (3.3)$$

Note that since P represents the total number of dead polymer chains per unit volume, from equation (2.24) we have:

$$\frac{dP}{dt} = \sum_{n=1}^{\infty} \frac{dP_n}{dt} = \alpha R_p \sum_{n=1}^{\infty} \left[\frac{\gamma + \frac{1}{2}(n-1)\alpha\beta}{(1+\alpha)^n} \right] \quad (3.4)$$

which using equation (2.29) reduces to:

$$\frac{dP}{dt} = \alpha R_p \frac{1}{\alpha} \left(\gamma + \frac{\beta}{2} \right) = R_p \left(\gamma + \frac{\beta}{2} \right) \quad (3.5)$$

The total number of chains per unit volume produced at time t , is then given by:

$$P(t) = \int_0^t R_p \left(\gamma + \frac{\beta}{2} \right) dt \quad (3.6)$$

Examples

Let us calculate now a few moments:

- μ_0^c

$$\mu_0^c = \frac{1}{P(t)} \int_0^{P(t)} \mu_0 dP = \frac{P(t)}{P(t)} = 1 \quad (3.7)$$

- μ_1^c and μ_2^c

$$\mu_1^c = \frac{1}{P(t)} \int_0^{P(t)} \mu_1 dP \quad (3.8)$$

$$\mu_2^c = \frac{1}{P(t)} \int_0^{P(t)} \mu_2 dP \quad (3.9)$$

In both cases we get the weighted average of the instantaneous properties.

- cumulative number average of the MWD, \bar{n}_N^c

$$\bar{n}_N^c = \frac{\mu_1^c}{\mu_0^c} = \frac{1}{P(t)} \int_0^{P(t)} \mu_1 dP = \frac{1}{P(t)} \int_0^{P(t)} \frac{\mu_1}{\mu_0} dP = \frac{1}{P(t)} \int_0^{P(t)} \bar{n}_N dP \quad (3.10)$$

Again we obtain the weighted average of the instantaneous property.

- cumulative weight average of the MWD, \bar{n}_W^c

$$\bar{n}_W^c = \frac{\mu_2^c}{\mu_1^c} = \frac{\int_0^{P(t)} \mu_2 dP}{\int_0^{P(t)} \mu_1 dP} \neq \frac{1}{P(t)} \int_0^{P(t)} \frac{\mu_2}{\mu_1} dP = \frac{1}{P(t)} \int_0^{P(t)} \bar{n}_W dP \quad (3.11)$$

- polydispersity index, σ^c

$$\sigma^c = \frac{\mu_2^c \mu_0^c}{(\mu_1^c)^2} = \frac{\int_0^{P(t)} \mu_2 dP}{\frac{1}{P(t)} \left[\int_0^{P(t)} \mu_1 dP \right]^2} \neq \frac{1}{P(t)} \int_0^{P(t)} \sigma dP \quad (3.12)$$

Note that \bar{n}_W^c and σ^c are not anymore the weighted averages of the corresponding instantaneous quantities. To obtain them, the integrals in equations (3.11) and (3.12) have to be solved.

In conclusion, when computing the averages of a cumulative CLD it is convenient to integrate the following ODE to get the cumulative moments

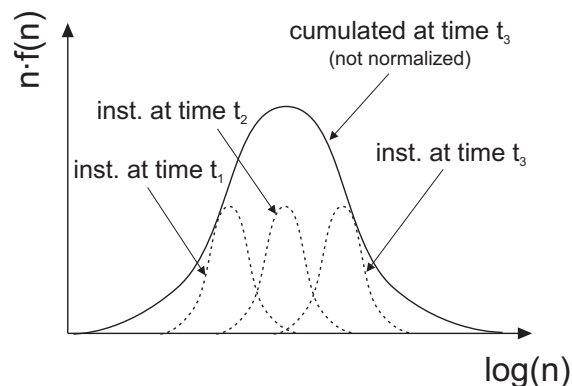
$$\frac{d(\mu_j^c P)}{dt} = \mu_j \frac{dP}{dt} \quad (3.13)$$

and from this compute the desired averages.

3.1.1 Width of the Cumulative Distribution

The width of the cumulative CLD can be regarded as determined by two factors:

- the width of the instantaneous CLD which is given by the kinetics of the process
- the shifting of the instantaneous average chain length with time.



If the instantaneous CLD is constant in time, so as its average \bar{n} , then the cumulative CLD superimposes the instant one and the two have the same polydispersity. However, if the instantaneous \bar{n} changes in time the cumulative polydispersity is certainly larger than the instantaneous one, that is:

$$\sigma^c \geq \sigma \quad (3.14)$$

3.2 Designing Polymerization Processes with Respect to Desired CLDs

3.2.1 Case I: Termination by Combination is Negligible

If termination by combination is negligible with respect to at least one of the other chain termination reactions we have $\beta \ll \gamma$, and then from equations (2.43) to (2.45):

$$\bar{n}_N = \frac{1}{\gamma} \quad (3.15)$$

$$\bar{n}_W = \frac{2}{\gamma} \quad (3.16)$$

$$\sigma = 2 \quad (3.17)$$

For $f_N(n)$ we obtain:

$$f_N(n) = \frac{\gamma}{(1 + \gamma)^n} \approx \gamma \exp(-\gamma n) \quad (3.18)$$

This result corresponds to the so-called *most probable* or *Flory distribution*. The expression for $f_W(n)$ is then:

$$f_W(n) = \frac{nf_N(n)}{\mu_1} = \frac{n\gamma^2}{(1 + \gamma)^n} \approx n\gamma^2 \exp(-\gamma n) \quad (3.19)$$

Thus, in order to control the CLD we have to play with the parameter γ .

Chain Transfer to Monomer Dominates

Let us assume that chain transfer to monomer is the dominating chain termination in the entire polymerization system. In this case we have:

$$\gamma = \frac{\tau_p}{\tau_{fm}} + \frac{\tau_p}{\tau_{fs}} + \frac{\tau_p}{\tau_{td}} \approx \frac{\tau_p}{\tau_{fm}} = \frac{k_{fm}}{k_p} \quad (3.20)$$

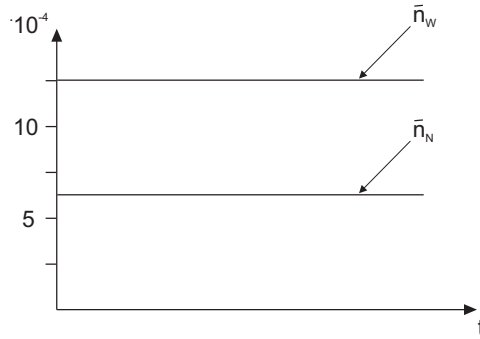
$$\Rightarrow \gamma = f(\text{temp.}) \quad (3.21)$$

For an isothermal batch reactor we obtain therefore:

$$\gamma = \text{const.} \Rightarrow \bar{n}_N = \text{const.} \quad (3.22)$$

and

$$\sigma^c = \sigma = 2 \quad (3.23)$$



A typical example for this case is the polymerization of vinyl chloride to PVC. If we want to produce the narrowest possible CLD, the only problem is therefore to control the temperature during the entire process. In addition, we note that:

- in order to increase \bar{n}_N , the temperature has to be reduced $\Rightarrow \gamma$ decreases
- in order to decrease \bar{n}_N , the temperature has to be increased $\Rightarrow \gamma$ increases.

This follows from the observation that the activation energy is typically larger for chain transfer to monomer than for propagation, so that $\gamma = k_{\text{fm}}/k_p$ is an increasing function with temperature. Note that since the temperature can only be changed to a certain extent, only modest changes in the average chain length can be achieved. In order to achieve a significant reduction in the average chain length it is more effective to add a chain transfer agent which results in a new dominating termination step, i.e., $\tau_{\text{fs}} \ll \tau_{\text{fm}}$. On the other hand a significant increase in the average chain length would be difficult to achieve.

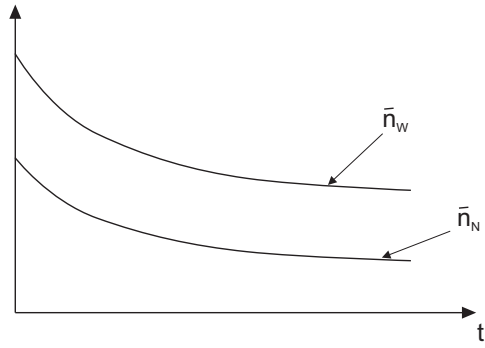
Termination by Disproportionation Dominates

In the case where termination by disproportionation is the dominating chain termination reaction, γ becomes:

$$\gamma \approx \frac{\tau_p}{\tau_{\text{td}}} = \frac{k_{\text{td}} R^{\bullet}}{k_p M} = \frac{\sqrt{k_{\text{td}} R_I}}{k_p M} \quad (3.24)$$

In order to keep γ constant, we have to keep the constant monomer concentration, M , the temperature, T , as well as the rate of radical production, R_I . This is obviously difficult in batch systems. Therefore, the value of \bar{n}_N will most likely decrease with M and therefore

$$\sigma^c > \sigma = 2 \quad (3.25)$$



A typical example for this case is the polymerization of methyl methacrylate to PMMA where $\sigma^c \approx 5$. To obtain a lower value of σ^c we have two possibilities:

- work in semi-batch reactors where monomer is continuously added in order to keep constant its concentration in the reactor
- use emulsion polymerization.

Industrially, PVC is produced mainly in suspension whereas PMMA is usually produced in emulsion.

3.2.2 Case II: Termination by Combination Dominates

In the case where bimolecular combination is the dominating chain termination reaction we have $\beta \gg \gamma$ and therefore from equations (2.43)-(2.45) we have:

$$\bar{n}_N = \frac{2}{\beta} \quad (3.26)$$

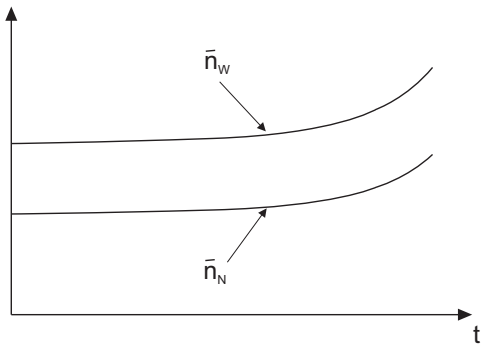
$$\bar{n}_W = \frac{3}{\beta} \quad (3.27)$$

$$\sigma = 1.5 \quad (3.28)$$

Note that termination by combination potentially leads to the narrowest CLD.

$$\beta = \frac{\tau_p}{\tau_{tc}} = \frac{k_{tc} R^\bullet}{k_p M} = \frac{\sqrt{k_{tc} R_I}}{k_p M} \quad (3.29)$$

CHAPTER 3. CUMULATIVE PROPERTIES OF POLYMERS



Thus, we can draw the same conclusion as in the previous case (section 3.2.1). As a typical example the low-temperature polymerization of styrene can be mentioned ($T = 50^\circ\text{C}$).

In a batch system we would again expect a decreasing \bar{n}_N with conversion. However, experimentally the opposite is observed. This is due to the fact that, although M decreases, because of the gel effect k_{tc} decreases even more, resulting in a decreasing value of β .

Chapter 4

Copolymerization

4.1 Kinetics of Copolymerization

4.1.1 Involved Chemical Reactions

Initiation	$I_2 + M \longrightarrow 2 R_1^\bullet$	$r = 2fk_d I_2 \equiv R_I$
Propagation	$A_{m,n}^\bullet + A \xrightarrow{k_{pAA}} A_{m+1,n}^\bullet$ $A_{m,n}^\bullet + B \xrightarrow{k_{pAB}} B_{m,n+1}^\bullet$ $B_{m,n}^\bullet + A \xrightarrow{k_{pBA}} A_{m+1,n}^\bullet$ $B_{m,n}^\bullet + B \xrightarrow{k_{pBB}} B_{m,n+1}^\bullet$	$r = k_{pAA} A A_{m,n}^\bullet$ $r = k_{pAB} B A_{m,n}^\bullet$ $r = k_{pBA} A B_{m,n}^\bullet$ $r = k_{pBB} B B_{m,n}^\bullet$
Chain Transfer	$A_{m,n}^\bullet + S \xrightarrow{k_{fsA}} R_1^\bullet + P_{m,n}$ $B_{m,n}^\bullet + S \xrightarrow{k_{fsB}} R_1^\bullet + P_{m,n}$	$r = k_{fsA} S A_{m,n}^\bullet$ $r = k_{fsB} S B_{m,n}^\bullet$
Termination	$A_{m,n}^\bullet + A_{r,q}^\bullet \xrightarrow{k_{tAA}} P_{m+r,n+q} \text{ or } P_{m,n} + P_{r,q}$ $A_{m,n}^\bullet + B_{r,q}^\bullet \xrightarrow{k_{tAB}} P_{m+r,n+q} \text{ or } P_{m,n} + P_{r,q}$ $B_{m,n}^\bullet + B_{r,q}^\bullet \xrightarrow{k_{tBB}} P_{m+r,n+q} \text{ or } P_{m,n} + P_{r,q}$	$r = k_{tAA} A_{m,n}^\bullet A_{r,q}^\bullet$ $r = k_{tAB} A_{m,n}^\bullet B_{r,q}^\bullet$ $r = k_{tBB} B_{m,n}^\bullet B_{r,q}^\bullet$

where $n, m, r, q = [1 \dots \infty]$ and $k_t = k_{tc} + k_{td}$

Note that a similar notation as for homopolymerization has been used above with, for example, $A_{m,n}^\bullet$ indicating the concentration of active chains containing m units of monomer A and n units of monomer B, and terminating with a monomer A unit. The latter unit, where the radical is located, defines the reactivity of the active chains, and accordingly determines the rate constant of all the reactions above. This is usually referred to as the terminal kinetic model. So for example, k_{pAB} represents the rate constant for the propagation of radical chain of type A and any length with a monomer B.

4.1.2 Long-Chain Approximation

The long-chain approximation (LCA) starts from the observation that the following equality holds along a polymer chain:

$$(\text{number of transitions } A \rightarrow B) = (\text{number of transitions } B \rightarrow A) \pm 1 \quad (4.1)$$

These geometrical considerations lead to the following condition on reaction rates:

$$k_{pAB}A^\bullet B = k_{pBA}B^\bullet A \quad (4.2)$$

Let us define

$$R^\bullet = A^\bullet + B^\bullet \quad (4.3)$$

where A^\bullet represents the total concentration of radicals of type A, that is radicals terminating with a monomer of type A:

$$A^\bullet = \sum_{m=1}^{\infty} \sum_{n=1}^{\infty} A_{m,n}^\bullet \quad (4.4)$$

Therefore we obtain:

$$k_{pAB}A^\bullet B = k_{pBA}(R^\bullet - A^\bullet)A \quad (4.5)$$

$$\Rightarrow A^\bullet = \frac{k_{pBA}A}{(k_{pAB}B + k_{pBA}A)} R^\bullet = p_A R^\bullet \quad (4.6)$$

$$\Rightarrow B^\bullet = \frac{k_{pAB}B}{(k_{pAB}B + k_{pBA}A)} R^\bullet = p_B R^\bullet \quad (4.7)$$

where p_A is the probability of having a radical of type A. Now, let us write the mass balance for A^\bullet and B^\bullet :

$$\frac{dA^\bullet}{dt} = R_{IA} + k_{pBA}B^\bullet A - k_{pAB}A^\bullet B - k_{tAA}A^{\bullet 2} - k_{tAB}A^\bullet B^\bullet \quad (4.8)$$

$$\frac{dB^\bullet}{dt} = R_{IB} + k_{pAB}A^\bullet B - k_{pBA}B^\bullet A - k_{tBB}B^{\bullet 2} - k_{tAB}A^\bullet B^\bullet \quad (4.9)$$

The rates of initiation for the monomers A and B are defined as the product of the overall rate of initiation and the respective monomer mole fractions in the monomer phase, i.e., $R_{IA} = R_I X_A$ and $R_{IB} = R_I X_B$, where

$$X_A = \frac{A}{A + B} \quad \text{and} \quad X_B = \frac{B}{A + B} \quad (4.10)$$

CHAPTER 4. COPOLYMERIZATION

The summation of equation (4.8) and (4.9) gives:

$$\frac{dR^\bullet}{dt} = \frac{dA^\bullet}{dt} + \frac{dB^\bullet}{dt} = R_{IA} + R_{IB} - k_{tAA}A^{\bullet 2} - k_{tBB}B^{\bullet 2} - 2k_{tAB}A^\bullet B^\bullet \quad (4.11)$$

Applying the pseudo steady state assumption to R^\bullet and using $R_I = R_{IA} + R_{IB}$ we obtain:

$$R_I - k_{tAA}p_A^2 R^{\bullet 2} - k_{tBB}p_B^2 R^{\bullet 2} - 2k_{tAB}p_A p_B R^{\bullet 2} = 0 \quad (4.12)$$

and therefore

$$R^\bullet = \sqrt{\frac{R_I}{k_t^*}} \quad (4.13)$$

where k_t^* is defined as follows:

$$k_t^* = k_{tAA}p_A^2 + 2k_{tAB}p_A p_B + k_{tBB}p_B^2 \quad (4.14)$$

To conclude, we obtain the same result as in the case of homopolymerization with a pseudo-termination rate constant, k_t^* defined by equation (4.14) replacing the actual termination rate constant, k_t .

4.1.3 Rate of Monomer Consumption

Since propagation reactions dominate monomer consumption, we have:

$$R_{pA} = k_{pAA}A^\bullet A + k_{pBA}B^\bullet A = (k_{pAA}p_A + k_{pBA}p_B)AR^\bullet \quad (4.15)$$

$$R_{pB} = k_{pBB}B^\bullet B + k_{pBA}A^\bullet B = (k_{pBB}p_B + k_{pAB}p_A)BR^\bullet \quad (4.16)$$

$$\Rightarrow \begin{cases} R_{pA} = k_{pA}^* AR^\bullet \\ R_{pB} = k_{pB}^* BR^\bullet \end{cases} \Rightarrow R_{p,tot} = R_{pA} + R_{pB} = \overline{k_p M}^* R^\bullet \quad (4.17)$$

$$\Rightarrow R_{p,tot} = R_{pA} + R_{pB} = \overline{k_p M}^* R^\bullet \quad (4.18)$$

Introducing the pseudo-propagation rate constants k_{pA}^* and k_{pB}^* we obtain again a similar expression as in the case of homopolymerization.

4.2 Chain Length Distribution of Copolymers

4.2.1 Population Balance Equation

In this section we calculate the CLD in the case of a copolymerization process. Let us therefore consider the population balance of chain radicals terminating with a monomer unit A and containing r units of any type (A or B):

$$\begin{aligned} \frac{dA_r^{\bullet}}{dt} = & k_{pAA} \cdot A \cdot A_{r-1}^{\bullet} + k_{pBA} \cdot A \cdot B_{r-1}^{\bullet} \\ & - (k_{pAA} \cdot A + k_{pAB} \cdot B) A_r^{\bullet} \\ & - k_{fsA} \cdot S \cdot A_r^{\bullet} - (k_{tAA} \cdot A^{\bullet} + k_{tAB} \cdot B^{\bullet}) A_r^{\bullet} \end{aligned} \quad (4.19)$$

and similarly for the radicals terminating with a B unit:

$$\begin{aligned} \frac{dB_r^{\bullet}}{dt} = & k_{pBB} \cdot B \cdot B_{r-1}^{\bullet} + k_{pAB} \cdot B \cdot A_{r-1}^{\bullet} \\ & - (k_{pBB} \cdot B + k_{pBA} \cdot A) B_r^{\bullet} \\ & - k_{fsB} \cdot S \cdot B_r^{\bullet} - (k_{tBB} \cdot B^{\bullet} + k_{tBA} \cdot A^{\bullet}) B_r^{\bullet} \end{aligned} \quad (4.20)$$

Applying the long-chain approximation and using $R_r^{\bullet} = A_r^{\bullet} + B_r^{\bullet}$ we obtain:

$$\begin{aligned} \frac{dR_r^{\bullet}}{dt} = & [(k_{pAA} \cdot p_A + k_{pBA} \cdot p_B) \cdot A + (k_{pBB} \cdot p_B + k_{pAB} \cdot p_A) \cdot B] \cdot R_{r-1}^{\bullet} \\ & - [(k_{pAA} \cdot p_A + k_{pBA} \cdot p_B) \cdot A + (k_{pBB} \cdot p_B + k_{pAB} \cdot p_A) \cdot B] \cdot R_r^{\bullet} \\ & - (k_{fsA} \cdot p_A + k_{fsB} \cdot p_B) \cdot S \cdot R_r^{\bullet} \\ & - (k_{tAA} \cdot p_A^2 + 2k_{tAB} \cdot p_A \cdot p_B + k_{tBB} \cdot p_B^2) \cdot R_r^{\bullet} \cdot R^{\bullet} \end{aligned} \quad (4.21)$$

A further simplification can be achieved when using the pseudo-homopolymerization rate constants:

$$\frac{dR_r^{\bullet}}{dt} = \overline{k_p M}^* R_{r-1}^{\bullet} - \overline{k_p M}^* R_r^{\bullet} - k_{fs}^* S R_r^{\bullet} - k_t^* R_r^{\bullet} R^{\bullet} \quad (4.22)$$

This expression is identical to the population balance equation (PBE) for a homopolymer containing r monomer units. We can extrapolate this result to all PBEs involved in computing the CLD for copolymers. This method is the so-called pseudo-homogeneous approach, it will be discussed in the next section.

4.2.2 Pseudo-Homogeneous Approach

From the results above we can conclude as follows:

CHAPTER 4. COPOLYMERIZATION

When using the long chain approximation, the PBE for the CLD of a copolymerization process can be reduced to the corresponding ones of a homopolymerization process, where the actual polymerization rate constants are replaced by suitable averages (pseudo-kinetic parameters) of the actual copolymerization rate constants.

These averages are different depending upon the reaction order with respect to the radical species:

- zero-order processes

$$R_I = R_{IA} + R_{IB} \quad (4.23)$$

- first-order processes

$$\overline{k_p M}^* = (k_{pAA} p_A + k_{pBA} p_B) \cdot A + (k_{pBB} p_B + k_{pAB} p_A) \cdot B \quad (4.24)$$

$$k_{fs}^* = k_{fsA} p_A + k_{fsB} p_B \quad (4.25)$$

- second-order processes

$$k_t^* = k_{tAA} p_A^2 + 2k_{tAB} p_A p_B + k_{tBB} p_B^2 \quad (4.26)$$

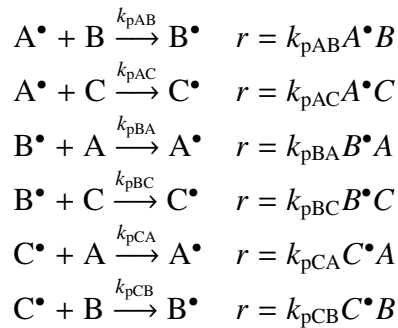
This implies that in order to compute the CLD of a copolymer we can use the same equations developed above for a homopolymer, by simply replacing the actual homopolymerization constants with the pseudo-homopolymerization ones (function of the actual copolymerization rate constants). This procedure is referred to as the pseudo-homopolymerization approach. Note that all rate constants of the pseudo-homopolymerization are functions of the composition of the monomer phase which in principle changes during the reaction.

4.2.3 Kinetics of Multi-Monomer Polymerization

The current polymer technology requires, for applications of increasing complexity, the production of chains containing two or more monomer. As the long chain assumption cannot be extended to the case where more than two monomers are involved one has to take a different approach.

Let us consider the case of three monomer polymerization, and write the molar balances of the radical chains with the same terminal unit and any chain length. Since the cross propagation reactions dominate these balances we consider the following reactions:

CHAPTER 4. COPOLYMERIZATION



The following balances follow:

$$\frac{dA^\bullet}{dt} = k_{pBA}B^\bullet A + k_{pCA}C^\bullet A - (k_{pAB}B + k_{pAC}C)A^\bullet \quad (4.27)$$

$$\frac{dB^\bullet}{dt} = k_{pAB}A^\bullet B + k_{pCB}C^\bullet B - (k_{pBA}A + k_{pBC}C)B^\bullet \quad (4.28)$$

$$R^\bullet = A^\bullet + B^\bullet + C^\bullet \quad (4.29)$$

Note that the last equation has been introduced to replace the molar balance of C^\bullet which would have been a linear combination of the first two. We cannot compute the absolute values of A^\bullet , B^\bullet and C^\bullet but only their ratios. Thus, introducing the probabilities (or mole fractions):

$$p_A = A^\bullet/R^\bullet, \quad p_B = B^\bullet/R^\bullet, \quad p_C = C^\bullet/R^\bullet$$

we get:

$$\begin{cases} k_{pBA}Ap_B + k_{pCA}Ap_C - (k_{pAB}B + k_{pAC}C)p_A = 0 \\ k_{pAB}Bp_A + k_{pCB}Bp_C - (k_{pBA}A + k_{pBC}C)p_B = 0 \\ p_A + p_B + p_C = 1 \end{cases} \quad (4.30)$$

which is a linear system with three unknowns. Note that in the case of binary copolymerization, the system above reduces to:

$$\begin{cases} k_{pBA}Ap_B - k_{pAB}Bp_A = 0 \\ p_A + p_B = 1 \end{cases} \quad (4.31)$$

which leads to the same solution

$$p_A = \frac{k_{pBA}A}{k_{pBA}A + k_{pAB}B} \quad (4.32)$$

obtained earlier using LCA. Which means that LCA is simply a short-cut form of the pseudo steady state approximation in the case of binary copolymers. This procedure can be generalized to any number of monomer species greater or equal than three.

CHAPTER 4. COPOLYMERIZATION

Note that in equation (4.27) and (4.28) we have assumed that the cross propagation reactions are much faster than all terminations. This is generally the case in polymerization systems, with the only exception of block polymerization.

The pseudo-homopolymerization rate constants are then computed using the same rules indicated above:

- zero-order average

$$R_I = R_{IA} + R_{IB} + R_{IC} + \dots \quad (4.33)$$

- first-order average

$$k_{fs}^* = k_{fsA}p_A + k_{fsB}p_B + k_{fsC}p_C + \dots \quad (4.34)$$

$$k_{pA}^* = k_{pAA}p_A + k_{pBA}p_B + k_{pCA}p_C + \dots \quad (4.35)$$

$$k_{pB}^* = k_{pAB}p_A + k_{pBB}p_B + k_{pCB}p_C + \dots \quad (4.36)$$

$$\dots \quad (4.37)$$

- second-order average

$$\begin{aligned} k_t^* = & k_{tAA}p_A^2 + k_{tBB}p_B^2 + k_{tCC}p_C^2 \\ & + 2k_{tAB}p_Ap_B + 2k_{tAC}p_Ap_C + 2k_{tBC}p_Bp_C \\ & + \dots \end{aligned} \quad (4.38)$$

4.3 Chain Composition Distribution of Copolymers

4.3.1 Instantaneous Chain Composition

The mole fraction of A in the differential amounts of polymer produced at a given instant of time is given by:

$$F_A = \frac{R_{pA}}{R_{pA} + R_{pB}} \quad (4.39)$$

where the rate of polymerization of A and B can be computed using equation (4.17):

$$F_A = \frac{(k_{pAA}p_A + k_{pBA}p_B) \cdot A}{(k_{pAA}p_A + k_{pBA}p_B) \cdot A + (k_{pBB}p_B + k_{pAB}p_A) \cdot B} \quad (4.40)$$

CHAPTER 4. COPOLYMERIZATION

As seen in equation (4.6) and (4.7) the probability of having a radical of type A or B is given by:

$$p_A = \frac{k_{pBA}A}{k_{pBA}A + k_{pAB}B}$$

$$p_B = \frac{k_{pAB}B}{k_{pBA}A + k_{pAB}B}$$

If we now introduce the reactivity ratios, which are defined as the ratio between the direct and the cross propagation rate constant for a given radical,

$$r_A = \frac{k_{pAA}}{k_{pAB}} \quad \text{and} \quad r_B = \frac{k_{pBB}}{k_{pBA}} \quad (4.41)$$

we can rewrite equation (4.40) as follows:

$$\begin{aligned} F_A &= \frac{(r_A A + B) \cdot A}{(r_A A + B) \cdot A + (r_B B + A) \cdot B} \\ &= \frac{(r_A X_A + X_B) \cdot X_A}{(r_A X_A + X_B) \cdot X_A + (r_B X_B + X_A) \cdot X_B} \end{aligned} \quad (4.42)$$

Equation (4.42) is the so-called Mayo-Lewis equation which contains only two kinetic parameters, r_A and r_B . In order to understand the effect of the reactivity ratios on the Mayo-Lewis equation we will derive the expression for dF_A/dX_A . Therefore we rewrite equation (4.42) using the expression $X_B = 1 - X_A$

$$F_A = \frac{(r_A - 1)X_A^2 + X_A}{(r_A - 2)X_A^2 + 2X_A + r_B(1 - X_A)^2} \quad (4.43)$$

and then differentiate with respect to X_A

$$\frac{dF_A}{dX_A} = \frac{[2(r_A - 1)X_A + 1]den - nom[2(r_A - 2)X_A + 2 - 2r_B(1 - X_A)]}{den^2} \quad (4.44)$$

where den and nom are the denominator and nominator of equation (4.43), respectively. Now we will consider the limits of dF_A/dX_A for $X_A \rightarrow 0$ and $X_A \rightarrow 1$:

$$\left. \frac{dF_A}{dX_A} \right|_{X_A \rightarrow 0} = \frac{1}{r_B} \quad (4.45)$$

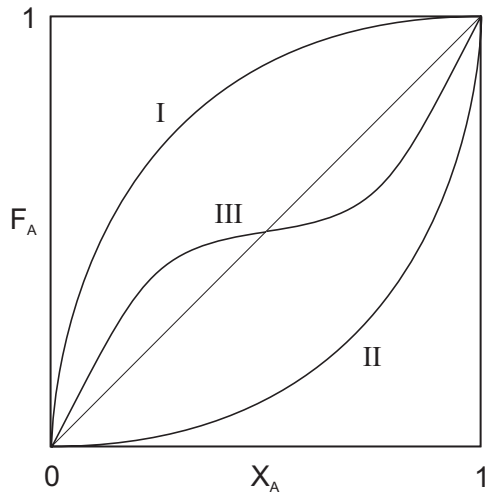
$$\left. \frac{dF_A}{dX_A} \right|_{X_A \rightarrow 1} = \frac{1}{r_A} \quad (4.46)$$

In the following we want to distinguish three different cases:

CHAPTER 4. COPOLYMERIZATION

- I $(r_A > 1) \wedge (r_B < 1)$: $\left(\frac{dF_A}{dX_A} \Big|_{X_A \rightarrow 0} > 1 \right) \wedge \left(\frac{dF_A}{dX_A} \Big|_{X_A \rightarrow 1} < 1 \right)$
 both radicals "prefer" to propagate with A
 (A is more reactive)
- II $(r_A < 1) \wedge (r_B > 1)$: $\left(\frac{dF_A}{dX_A} \Big|_{X_A \rightarrow 0} < 1 \right) \wedge \left(\frac{dF_A}{dX_A} \Big|_{X_A \rightarrow 1} > 1 \right)$
 both radicals "prefer" to propagate with B
 (B is more reactive)
- III $(r_A < 1) \wedge (r_B < 1)$: $\left(\frac{dF_A}{dX_A} \Big|_{X_A \rightarrow 0} > 1 \right) \wedge \left(\frac{dF_A}{dX_A} \Big|_{X_A \rightarrow 1} > 1 \right)$
 both radicals "prefer" to propagate with the other monomer

The Mayo-Lewis plot represents the instantaneous composition of a polymer, F_A produced from a given monomer phase composition, X_A and it can be represented by the following plot.

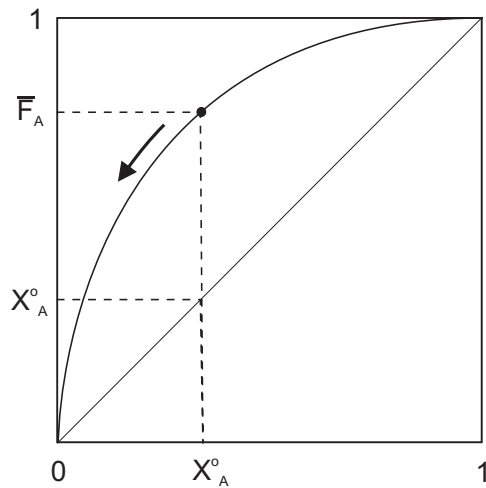


4.3.2 Composition Drift

Let us analyze the behavior of the chain composition distribution in a batch reactor using the Mayo-Lewis diagram. Suppose that we charge initially in the reactor a monomer mixture where the molar fraction of A is X_A^0 . As soon as the reaction starts we produce polymer chains with mole fraction of A equal to \bar{F}_A . However, since $\bar{F}_A > X_A^0$ the monomer phase

CHAPTER 4. COPOLYMERIZATION

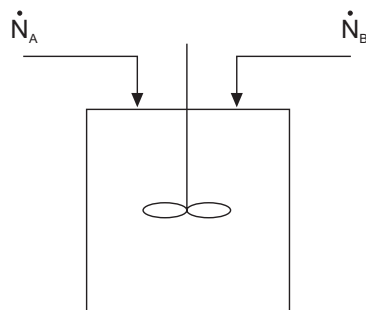
becomes poorer of A, and X_A decreases below the initial value X_A^0 . With the progress of the polymerization the X_A value decreases further, leading to the production of polymer chains continuously poorer in A, as indicated by the arrow in the plot.



Note that the composition drift produces substantial variations in the chain compositions. This can be appreciated by noting that complete monomer conversion, the average composition of all chains has to be equal to the initial monomer composition.

4.3.3 Chain Composition Control

In order to avoid the composition drift we have to use a semibatch reactor, where we introduce a flow rate \dot{N} of the two monomers in order to keep constant the monomer phase mole fraction, X_A and consequently also the composition of the produced polymer chains.



For this we consider the mass balances in a semibatch reactor where \dot{N}_A and \dot{N}_B are the molar

CHAPTER 4. COPOLYMERIZATION

flow rates of the two monomers:

$$\frac{dN_A}{dt} = \dot{N}_A - R_{pA}V \quad (4.47)$$

$$\frac{dN_B}{dt} = \dot{N}_B - R_{pB}V \quad (4.48)$$

where N_i represents the moles of the i -th monomer in the reactor, V is the volume of the reactor content, and R_{pA} and R_{pB} the monomer polymerization rate given by $R_{pA} = k_{pA}^* AR^\bullet$ and $R_{pB} = k_{pB}^* BR^\bullet$, respectively, so that:

$$\frac{dN_A}{dt} = \dot{N}_A - k_{pA}^* R^\bullet N_A \quad (4.49)$$

$$\frac{dN_B}{dt} = \dot{N}_B - k_{pB}^* R^\bullet N_B \quad (4.50)$$

where $N_A = AV$ and $N_B = BV$. Let us now introduce the dimensionless time $\tau = t/t_f$, where t_f is the duration of the process. So that we get:

$$\frac{dN_A}{d\tau} = t_f (\dot{N}_A - k_{pA}^* R^\bullet N_A) \quad (4.51)$$

$$\frac{dN_B}{d\tau} = t_f (\dot{N}_B - k_{pB}^* R^\bullet N_B) \quad (4.52)$$

with the initial conditions $N_A(0) = N_A^0$ and $N_B(0) = N_B^0$. Assuming that the pseudo kinetic propagation rate constants do not change during the process we can integrate the equations above to obtain:

$$N_A = \left(N_A^0 - \frac{\dot{N}_A}{k_{pA}^* R^\bullet} \right) \exp(-k_{pA}^* R^\bullet t_f \tau) + \frac{\dot{N}_A}{k_{pA}^* R^\bullet} \quad (4.53)$$

$$N_B = \left(N_B^0 - \frac{\dot{N}_B}{k_{pB}^* R^\bullet} \right) \exp(-k_{pB}^* R^\bullet t_f \tau) + \frac{\dot{N}_B}{k_{pB}^* R^\bullet} \quad (4.54)$$

The question is now how to operate the reactor in order to keep the monomer phase composition constant, i.e., $N_A/N_B = \text{const}$. There are two possible operation modes.

Starved Operation

This operation modus, which is frequent in reaction engineering, is based on the observation that the reactor under consideration is a self-regulated system, in the sense that it admits only

CHAPTER 4. COPOLYMERIZATION

one stable pseudo-steady state. Accordingly, as $\tau \rightarrow \infty$ the system autonomously approaches such a steady state, defined as follows:

$$\dot{N}_A = k_{pA}^* R^\bullet N_A^{pss} = R_{pA} V \quad (4.55)$$

$$\dot{N}_B = k_{pB}^* R^\bullet N_B^{pss} = R_{pB} V \quad (4.56)$$

This means that the system adjusts itself in order to satisfy the above pseudo-steady state condition, which means that the monomer amounts inside the reactor change from the initial values N_A^0 and N_B^0 , to the values N_A^{pss} and N_B^{pss} defined by the equations above which are such that the rate of consumption of each monomer by the polymerization process is equal to the rate of monomer feed to the reactor which we can of course control. Accordingly, in order to produce a copolymer with composition \bar{F}_A , in these conditions, we simply need to take $\dot{N}_A / (\dot{N}_A + \dot{N}_B) = \bar{F}_A$ constant in time so as to have $R_{pA} / (R_{pA} + R_{pB}) = \bar{F}_A$ and than produce a copolymer with instantaneous composition equal to the desired value. Note that the values N_A^{pss} and N_B^{pss} are such that the monomer mole fraction $X_A^{pss} = N_A^{pss} / (N_A^{pss} + N_B^{pss})$ is equal to the value that according to the Mayo-Lewis plot leads to the desired copolymer composition, \bar{F}_A . This is done autonomously by the system, we do not need to know this plot for the particular copolymer under examination.

The problem is that this condition is satisfied only at the pseudo-steady state, i.e., at $\tau \rightarrow \infty$, while during the transient period the copolymer composition is not equal to the desired value. However, by looking at the exponential functions in equations (4.53) and (4.54), we see that the pseudo-steady state condition is achieved at the time

$$\tau = \frac{1}{k_{pA}^* R^\bullet t_f} \quad \text{and} \quad \frac{1}{k_{pB}^* R^\bullet t_f} \quad (4.57)$$

for the two monomers. Thus, if we take a very long process time, i.e.,

$$t_f \gg \frac{1}{k_{pA}^* R^\bullet} \quad \text{or} \quad \frac{1}{k_{pB}^* R^\bullet} \quad (4.58)$$

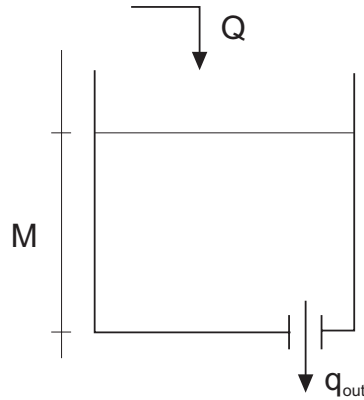
we have that the pseudo-steady state conditions are achieved after a very short fraction of the process time, i.e., $\tau \ll 1$, so that the amount of polymer produced in the transient condition is small, and we can actually make it negligible by increasing t_f at will. The starved equation made is then based on the second condition, that is the feed time should be sufficiently long,

CHAPTER 4. COPOLYMERIZATION

in particular such as to satisfy the condition above. A more intuitive explanation of the mechanism of this operation mode can be obtained by looking directly at the mass balances (4.51) and (4.52). By considering the first one in the form

$$\frac{dN_A}{d\tau} = t_f k_{pA}^* R^\bullet [N_A^{pss} - N_A] \quad (4.59)$$

we see that if we have $N_A < N_A^{pss} = \dot{N}_A / (k_{pA}^* R^\bullet)$ then $dN_A/d\tau > 0$ and N_A increases, while if $N_A > N_A^{pss}$ then $dN_A/d\tau < 0$ and N_A decreases. This means that N_A is always attracted towards the pseudo-steady state value N_A^{pss} (auto regulated system) with a "speed" which is higher the larger is the value of $t_f k_{pA}^* R^\bullet$. A similar argument holds true for B.



A simple example of an auto regulated system, which admits only one stable steady state is that of a tank with a hole, where feed the volumetric flow rate, Q of water. The mass balance leads to:

$$A \frac{dM}{dt} = Q - q_{out} \quad (4.60)$$

where M is the level of the liquid, A the cross section and the outlet flow rate is given by Bernoulli equation as $q_{out} = A_h \sqrt{2gM}$, where A_h is the cross section of the hole. The mass balance above can be rewritten as follows:

$$\frac{dM}{dt} = \frac{Q}{A} - \frac{A_h}{A} \sqrt{2gM} \quad (4.61)$$

Introducing the steady state value

$$\sqrt{M^{ss}} = \frac{Q}{A_h \sqrt{2g}} \quad (4.62)$$

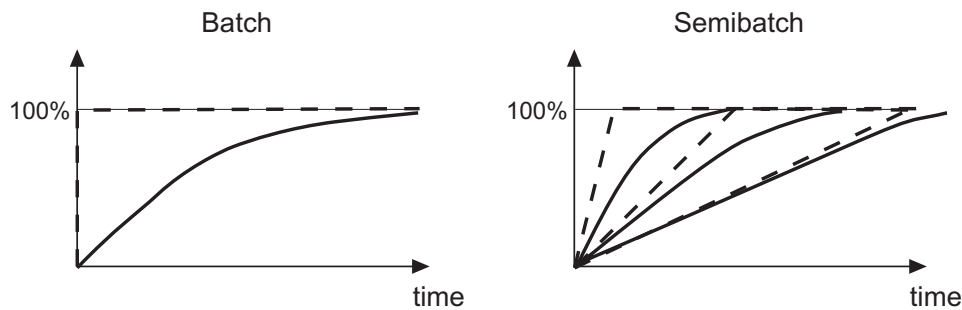
this reduces to:

$$\frac{dM}{dt} = \frac{A_h \sqrt{2g}}{A} (\sqrt{M^{ss}} - \sqrt{M}) \quad (4.63)$$

CHAPTER 4. COPOLYMERIZATION

which indicates that whatever is the initial level in the tank, this changes in order to reach the steady state value, which is the one that makes $q_{\text{out}} = Q$. This is in perfect analogy with the starved reactor, which is however a semibatch and not a continuous system, and therefore does not admit a real steady state.

Note that by taking the feed time $t_f \gg 1/(k_{pA}^* R^\bullet)$ or $1/(k_{pB}^* R^\bullet)$ we are imposing to the system a dynamics much slower than its intrinsic one, which is the dynamics of monomer consumption (whose characteristic times are $1/(k_{pA}^* R^\bullet)$ and $1/(k_{pB}^* R^\bullet)$ for the two monomers). Accordingly, we do not allow the monomer accumulation in the reactor, and this is the reason why this operation modus is referred to as starved. The time evolutions of conversion (solid line) and amount of monomer introduced in the reactor (dashed line) are shown in the figures below.



In other words we are forcing the reactor to produce much less than its potential in order to have a narrow chain composition distribution.

Power Feed Operation

In this operation modus we try to realize two objectives simultaneously:

- narrow chain composition distribution
- maximum productivity of the reactor

We can consider that we have two scalar and two reactor optimization variables, that is the amounts of the two monomers initially introduced in the reactor, N_A^0 and N_B^0 , and the two flow rates as a function of time, i.e., $\dot{N}_A(t)$ and $\dot{N}_B(t)$ for $t > 0$. We need to define them in order to satisfy the two objectives above. For the first objective function, i.e., chain composition equal to \bar{F}_A , we can first impose to have initially in the reactor the monomer phase composition,

CHAPTER 4. COPOLYMERIZATION

\bar{X}_A which leads to the desired polymer composition, \bar{F}_A . For this we need first to know the Mayo-Lewis relation to compute \bar{X}_A and then we impose:

$$\frac{N_A^0}{N_A^0 + N_B^0} = \bar{X}_A \quad (4.64)$$

Next we operate on the flow rates \dot{N}_A and \dot{N}_B in order to keep the monomer phase composition constant during the entire process, that is:

$$\frac{d(N_A/N_B)}{dt} = 0 \quad , \text{ for } t > 0 \quad (4.65)$$

or:

$$N_B \frac{dN_A}{dt} = N_A \frac{dN_B}{dt} \quad , \text{ for } t > 0 \quad (4.66)$$

which from the mass balances (4.49) and (4.50) leads to:

$$N_B (\dot{N}_A - k_{pA}^* R^\bullet N_A) = N_A (\dot{N}_B - k_{pB}^* R^\bullet N_B) \quad , \text{ for } t > 0 \quad (4.67)$$

This constraint allows keeping constant the composition of the produced polymer. A third constraint is on the total weight of the polymer produced in one batch, W_P which is imposed by the volume of the reactor:

$$\left(N_A^0 + \int \dot{N}_A dt \right) M_A^m + \left(N_B^0 + \int \dot{N}_B dt \right) M_B^m = W_P \quad (4.68)$$

We can now use the last degree of freedom to reach the second objective, that is maximum polymerization rate at any time during the process. This is a complex problem of demanding calculations whose simple solution is that the less reactive monomer (B in our case) should all be introduced at the beginning of the process, that is

$$\dot{N}_B = 0 \quad , \text{ for } t > 0 \quad (4.69)$$

which introduced in equation (4.67) leads to:

$$\dot{N}_A = (k_{pA}^* - k_{pB}^*) R^\bullet N_A \quad , \text{ for } t > 0 \quad (4.70)$$

which indicates that we have to add to the reactor the amount of A needed to equilibrate the change in composition induced by its higher reactivity with respect to B.

Thus, summarizing, if we need to produce a total amount of polymer W_P with uniform chain composition \bar{F}_A , we proceed as follows. Using the corresponding weight fractions \bar{F}_A^w and

CHAPTER 4. COPOLYMERIZATION

\bar{F}_B^w , we compute the total amounts (weights) of the two monomers needed W_A and W_B . From Mayo-Lewis relation we compute the monomer phase mole fraction \bar{X}_A which corresponds to \bar{F}_A . From this we compute the total moles of the two monomers to be initially introduced in the reactor:

$$N_B^0 = \frac{W_B}{M_B^m} \quad (4.71)$$

$$\frac{N_A^0}{N_A^0 + N_B^0} = \bar{X}_A \quad (4.72)$$

The remaining amount of A, given by $W_A/M_A^m - N_A^0$, is fed during the process according to the \dot{N}_A value given by equation (4.70).

This operation modus is economically more convenient than the starved operation but it requires to know the kinetics of the process (cf. Mayo-Lewis) and to be able to implement the condition (4.65) which requires either to measure on-line or to model the kinetic of the process. An additional problem which often arises with this procedure is that the very high productivity leads to a very large heat production which may be difficult to handle with a given heat exchange area. If the reactor cooling capacity is insufficient and fixed, one should reconsider the above optimization process and substitute the maximum productivity objective with the condition that the heat production rate should never exceed the potential heat cooling of the reactor, so as to be able to maintain isothermal operating conditions. This would be of the following form:

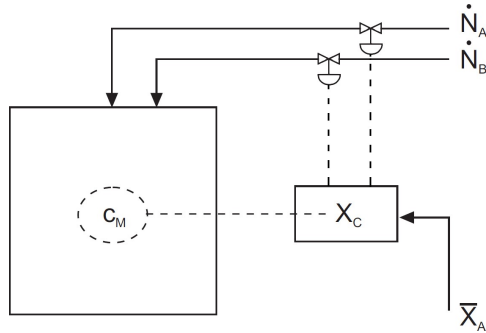
$$R_{pA}(-\Delta H_A) + R_{pB}(-\Delta H_B) \leq US(T - T_c) \quad (4.73)$$

where ΔH_i is the polymerization enthalpy of the i -th monomer, U and S are the reactor heat transfer coefficient and surface, respectively and T_c is the temperature of the cooling medium.

4.3.4 Reactor Monitoring and Control

The composition control problem can be solved with a closed-loop controller, provided that we have a reliable on-line sensor for the monomer phase composition. The measured composition could be compared to the set-point (\bar{X}_A) and then a proper action taken on the manipulated variables \dot{N}_A and \dot{N}_B . Such a sensor could be a gas chromatograph for the liquid phase or for the phase in the head space. The second is probably faster and more robust, but definitely not sufficiently for its routine use in a production environment. More easy is to measure on-line the global rate of polymerization in the reactor. For this we can use the reactor heat balance

CHAPTER 4. COPOLYMERIZATION



as follows:

$$(-\Delta H) R_p V = \dot{N}_c c_{pc} (T_c^{\text{out}} - T_c^{\text{in}}) \quad (4.74)$$

where \dot{N}_c and c_{pc} are the flow rate and the heat capacity of the cooling medium, and ΔH is the global reaction enthalpy. From this equation, by measuring on-line the outlet and inlet temperatures of the cooling medium, we can compute the instantaneous global rate of polymerization. Clearly, we have no way to distinguish the individual contribution of the two monomers from this energy balance. The above equation is approximate and in applications we should account for heat losses and for the heat accumulations. In addition, it is generally difficult to use a reactor as a calorimeter. On one hand in fact we need T_c^{out} and T_c^{in} to be very close so as to have a uniform cooling of the reactor. On the other hand, we need to have an appreciable difference of T_c^{out} and T_c^{in} in order to avoid an excessive propagation of the temperature measurement error in the estimated value of the global rate of polymerization. Other equivalent sensors are used in applications which estimate the rate of reaction from density measurements which are obtained by measuring the ultrasound propagation velocity in the reacting system. The complementary information needed to compute the rate of polymerization of the two individual monomers can be obtained using a kinetic model. The rate of monomer consumption is in fact given by:

$$\frac{dN_A}{dt} = -R_{pA} = -k_{pA}^* R^\bullet A V \quad (4.75)$$

In practice, the difficulty in using this equation is the evaluation of R^\bullet which is the source of many irreducibilities, due to unpredictable impurities, inhibitors or others. On the other hand, the polymer composition

$$F_A = \frac{R_{pA}}{R_{pA} + R_{pB}} = \frac{k_{pA}^* A}{k_{pA}^* A + k_{pB}^* B} \quad (4.76)$$

CHAPTER 4. COPOLYMERIZATION

does not depend on R^{\bullet} and therefore can be evaluated a priori with much higher reliability. The best way to monitor the reactor behavior is therefore to combine a sensor for measuring on-line the global polymerization rate with the equation above to split the total monomer consumption into the contributions of the two monomers.

Chapter 5

Heterogeneous Free-Radical Polymerization

We refer in particular to suspension and emulsion polymerization. In both cases we start from a suspension of monomer droplets ($d_d = 100 - 1000 \mu\text{m}$) in an aqueous solution obtained by rigorous stirring with the addition of some surfactant or emulsifier.

We then add an initiator which is monomer soluble for suspension and water soluble for emulsion polymerization.

Suspension Polymerization: At the end of the reaction we obtain a suspension of polymer particles with the same size as the original monomer droplets, i.e., $d_p \approx 100 - 1000 \mu\text{m}$. The radicals produced inside the particles promote the polymerization which proceeds just like in a bulk, thus following the kinetics described earlier for homogeneous polymerization.

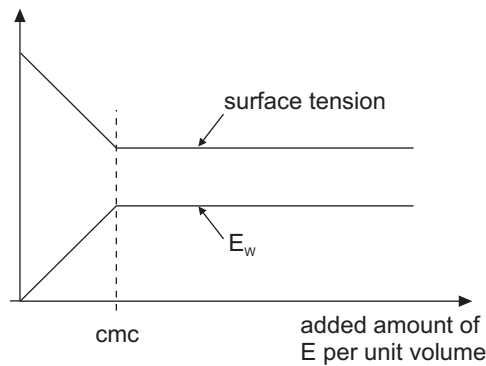
Emulsion Polymerization: In this case the final size of the polymer particles is $d_p \approx 100 \text{ nm}$, that is much smaller than the original monomer droplets. The mechanism of this process and the corresponding kinetic behavior are more complex and have to be treated separately.

5.1 Concept of Micellar Particle Nucleation

Emulsifier molecules form in water solution aggregates called micelles, when the total concentration of emulsifier tends to exceed a given concentration, the so-called critical micellar concentration (cmc).

This can be seen from surface tension measurements or from measurements of the free emulsifier concentration in the water phase, E_w .

The radicals produced in solution are initially hydrophilic, but after adding a few monomer units by solution polymerization, become enough hydrophobic to diffuse into the organic phase. There are two possibilities, the monomer droplets or the micelles, which in their core



solubilize some monomer. The choice depends upon the surface area available for transport:

$$\begin{aligned} \text{monomer droplets} &\Rightarrow \phi_M \frac{6}{d_d} \approx 0.50 \cdot \frac{6}{100} \approx 0.03 \mu\text{m}^{-1} \\ \text{micelles} &\Rightarrow \phi_E \frac{6}{d_m} \approx 0.01 \cdot \frac{6}{10^{-2}} \approx 6 \mu\text{m}^{-1} \end{aligned}$$

It follows that most of the radicals enter the micelle, and there start the polymerization with the monomer. At this point we say that a new polymer particle has been formed (nucleated).

5.2 Radical Segregation

The very small size of the polymer particles leads to the radical segregation which is the characteristic feature of emulsion polymerization.

Let us consider the minimum possible radical concentration in an emulsion polymer particle where bimolecular termination can occur:

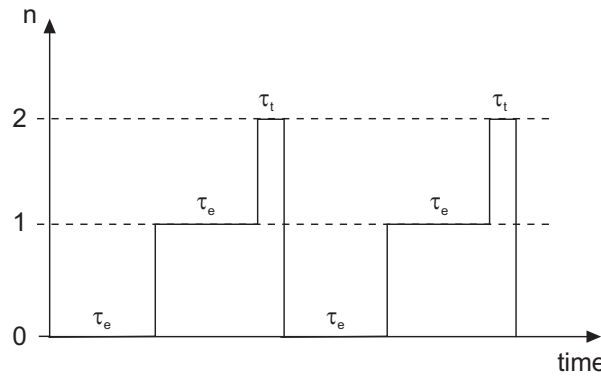
$$R^\bullet = \frac{2}{v_p N_A} = \frac{2}{10^{-18} \cdot 6 \cdot 10^{23}} \approx 0.3 \cdot 10^{-5} \text{ mol/L} \quad (5.1)$$

By considering a typical value for the termination rate constant, $k_t = 5 \cdot 10^7 \text{ L/mol/s}$, leads to a characteristic time for termination equal to:

$$\tau_t = \frac{1}{k_t R^\bullet} = 10^{-2} \text{ s} \quad (5.2)$$

Comparing this with the characteristic time for propagation, $\tau_p \approx 10^{-3} \text{ s}$ we conclude that the two radicals can add only a few monomer units before terminating.

We can now consider the number of radicals in a particle, n as a function of time:



We see that this follows a periodic evolution, where τ_e represents the characteristic time of entry of a radical from water phase in the polymer particle. We can then compute an approximate value of time average number of radicals per particle:

$$\bar{n} = \frac{0 \cdot \tau_e + 1 \cdot \tau_e + 2 \cdot \tau_t}{2 \cdot \tau_e + \tau_t} = \frac{\tau_e + 2 \cdot \tau_t}{2 \cdot \tau_e + \tau_t} \quad (5.3)$$

which since $\tau_t \ll \tau_e$, leads to:

$$\bar{n} \approx 0.5 \quad (5.4)$$

Note that most of the propagation of the radicals occurs when the radical is alone in the particle, and this lasts for a time equal to τ_e . Thus, in order to have sufficiently high molecular weights the initiator concentration is adjusted so that $\tau_e \gg \tau_p$. From this it follows that $\tau_e \gg \tau_t$.

The radical segregation has an important consequence on the quality of the produced polymer:

- Non-segregated system (homogeneous)

$$\begin{aligned} \text{rate of termination} &= k_t R^{\bullet 2} \\ \text{rate of propagation} &= k_p M R^{\bullet} \end{aligned} \Rightarrow \begin{cases} n_N \propto \frac{k_p M}{k_t R^{\bullet}} \\ R_p \propto k_p M R^{\bullet} \end{cases}$$

We have a conflict: in order to have high molecular weights, n_N we need low R^{\bullet} , but this leads to low rate of polymerization, R_p . This is because of the coupling between termination and propagation through the radical concentration, the first one having larger reaction order.

- Segregated system (emulsion)

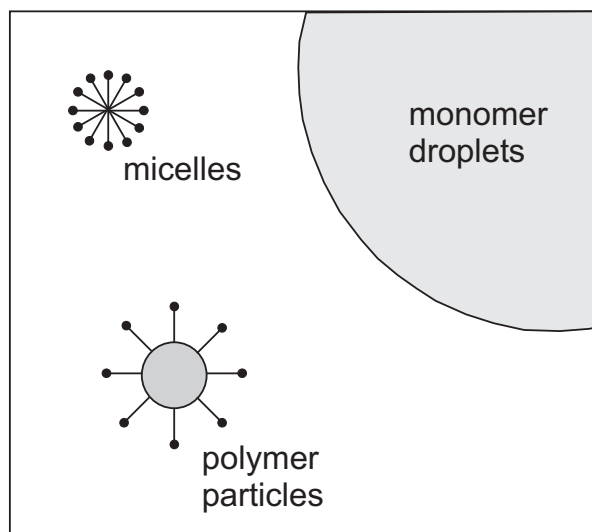
$$\begin{aligned}
 n_N &= (\text{rate of monomer addition}) \cdot \tau_e \\
 &= k_p M_p \cdot \frac{1}{k_e R_w^\bullet s_p N_A} \\
 R_p &= k_p M_p R_w^\bullet v_p N_p = k_p M_p \frac{\bar{n}}{v_p N_A} v_p N_p = k_p M_p \frac{\bar{n}}{N_A} N_p
 \end{aligned}$$

where k_e is the mass transfer coefficient of the radicals in the water phase, R_w^\bullet into the polymer particles with surface s_p and volume v_p ; M_p and R_p^\bullet are the monomer and radical concentrations in the polymer particles, and N_p is their number per unit volume of water.

It is seen that the quantities are now decoupled, and we can obtain high molecular weights with high productivity.

5.3 Phase Partitioning

During an emulsion polymerization process we have polymer particles, micelles and monomer droplets dispersed in the water phase. Monomer and free emulsifier are partitioned among these phases according to equilibrium. Since the external surfaces are very large (very small particles) the transport kinetics is in fact much faster than the polymerization reaction.



5.3.1 Monomer

As long as monomer droplets are present, $M_w + M_d > M_w^{\text{sat}}$ (where the indices refer to water and to the monomer droplets and M_w^{sat} is the concentration at saturation conditions), three phases are present, namely water, polymer particles, and monomer droplets. In this case we have:

$$a_w^M = a_p^M = a_d^M \quad (5.5)$$

where a_j^M is the activity of the monomer in phase j . Since the monomer droplets consist of pure monomer $a_d^M = 1$. Therefore the activity and concentration in the water and the polymer, M_w and M_p , remain constant, as long as monomer droplets are present. As the monomer is hardly soluble in water and its amount in the core of the micelles is usually negligible, most of the monomer is partitioned between the monomer droplets as well as in the swollen polymer particles (up to 60% in volume).

When the monomer droplets are consumed we have:

$$a_w^M = a_p^M \quad (5.6)$$

The activities can be computed using suitable thermodynamic models (FLORY HUGGINS, UNIQUAC, equation of states), to provide the concentration of the monomer in the two phases, M_w and M_p .

5.3.2 Emulsifier

Similarly, as in the previous case we have:

$$a_w^E = a_p^E \quad (5.7)$$

If $E_w > \text{cmc}$, then we have the formation of a third phase, the micelles. As long as micelles are present, the value of E_w does not change and we have $E_w = \text{cmc}$.

The above activity equality is in general represented by the Langmuir isotherm, which better describes the adsorption of the emulsifier on the surface of the polymer particles. Γ_E , the adsorbed emulsifier concentration [mol/vol] is given by:

$$\Gamma_E = \Gamma_E^\infty \frac{K_E E_w}{1 + K_E E_w} \quad (5.8)$$

where K_E is the adsorption equilibrium constant and Γ_E^∞ is the saturation concentration, which is achieved when the entire surface of the particle per unit volume, $a_p = s_p/v_p$ is covered by

CHAPTER 5. HETEROGENEOUS FREE-RADICAL POLYMERIZATION

the emulsifier. By defining a_E the surface area covered by a single emulsifier molecule we get:

$$\Gamma_E^\infty = \frac{a_p}{a_E N_A} \quad (5.9)$$

The emulsifier amount adsorbed on the monomer droplets is usually negligible.

5.4 Colloidal Stability

Besides its role in the nucleation process, the emulsifier is also very important in providing colloidal stability to the polymer particles. Let us consider an ionic surfactant (steric surfactants can also be used) where the surfactant molecule carries a net charge on the polymer particles, thus making them to repel each other and prevent coagulation.

As a rule of thumb, in order to avoid coagulation we have to keep most of the particle surface covered by the surfactant. Since the particles grow during polymerization, this can be achieved by adding the emulsifier during reaction and proportionally to the increase of the total polymeric surface.

5.5 Kinetic Mechanism of Emulsion Polymerization (Smith & Ewart, 1954)

The process is typically divided in three intervals.

Interval I: Nucleation

As soon as the radicals produced by the initiator enter the micelles we have the formation of new polymer particles. Other nucleation mechanisms are possible, but we now restrict only to the micellar one. In principle, we have that some of the radicals can terminate in the aqueous solution, some may enter the monomer droplets and some the previously formed polymer particles. However, particularly for fast nucleation the vast majority of radicals produced by the initiator enter the micelles, and therefore as a first approximation we have:

$$\frac{dN_p}{dt} = R_I \quad (5.10)$$

The nucleated polymer particles (increasing in number) grow by taking monomer from the aqueous solution (and eventually from the monomer droplets), their surface grows and adsorbs more and more surfactant. The surfactant available in the water phase decreases until all

micelles disappear and the concentration of emulsifier E_w starts dropping below cmc. This indicates the end of the nucleation interval, and the number of particles will thereafter remain constant.

Interval II: Growth

In this stage of the process the number of particles remains constant but their volume grows over time. The volume of a single particle, v_p , consist of polymer and monomer, $v_p = v_{\text{mon}} + v_{\text{pol}}$. The volume fraction of the monomer and the polymer in the particle can be written as follows:

$$\phi = \frac{v_{\text{mon}}}{v_p} \quad (5.11)$$

and

$$1 - \phi = \frac{v_{\text{pol}}}{v_p} \quad (5.12)$$

As long as monomer droplets are present (interval I and II) the volume fraction of monomer dissolved in the particle stays constant, $\phi = \text{const.} \equiv \phi^*$ (can reach values up to 0.6). First we will consider the volume growth of polymer in a single particle, v_{pol} :

$$\frac{dv_{\text{pol}}}{dt} = k_p M_p R_p^\bullet v_p \frac{M_{\text{mon}}^m}{\rho_{\text{pol}}} \quad (5.13)$$

with

$$M_p = \phi^* \frac{\rho_{\text{mon}}}{M_{\text{mon}}^m}$$

and

$$R_p^\bullet = \frac{\bar{n}}{N_A v_p}$$

one obtains

$$\begin{aligned} \frac{dv_{\text{pol}}}{dt} &= k_p \phi^* \frac{\rho_{\text{mon}}}{M_{\text{mon}}^m} \frac{\bar{n}}{v_p N_A} v_p \frac{M_{\text{mon}}^m}{\rho_{\text{pol}}} \\ &= k_p \phi^* \frac{\bar{n}}{N_A} \frac{\rho_{\text{mon}}}{\rho_{\text{pol}}} \end{aligned} \quad (5.14)$$

where the first three factors represents the moles of monomer reacted per unit time and per unit volume, M_{mon}^m is the monomer molecular weight and ρ_{mon} and ρ_{pol} the monomer and polymer densities respectively. From this, the volumetric growth of a single particle can be derived as

follows:

$$\begin{aligned}\frac{dv_p}{dt} &= \frac{d}{dt} \left(\frac{v_{\text{pol}}}{1 - \phi^*} \right) = \frac{dv_{\text{pol}}}{dt} \frac{1}{1 - \phi^*} \\ &= k_p \frac{\phi^*}{1 - \phi^*} \frac{\bar{n}}{N_A} \frac{\rho_{\text{mon}}}{\rho_{\text{pol}}}\end{aligned}\quad (5.15)$$

Note that v_{pol} is always increasing, whereas v_p is only increasing, when $\phi = \text{const.}$ (interval I and II).

Since $\bar{n} = 0.5$ and ϕ^* is kept constant by the presence of the monomer droplets, it follows that:

$$\frac{dv_p}{dt} = \text{const.} \equiv c \quad (5.16)$$

The overall reactor productivity

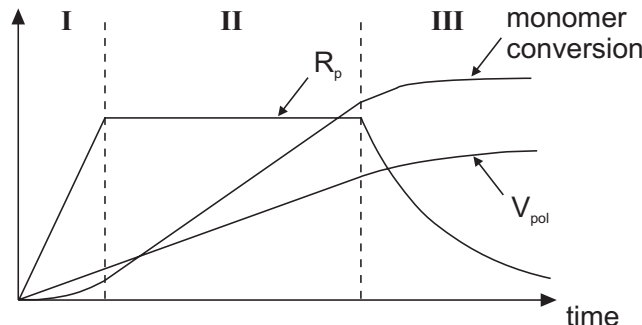
$$R_p \propto \frac{d}{dt} (v_p N_p) = N_p \frac{dv_p}{dt} = N_p c \quad (5.17)$$

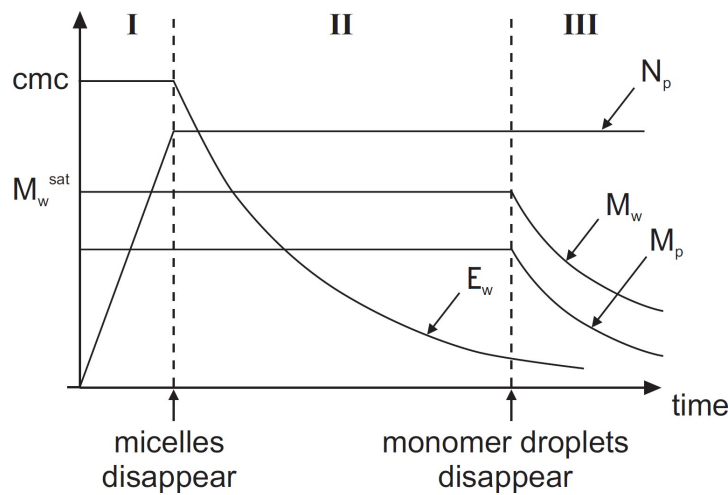
remains also constant during this interval.

This interval continuous as long as monomer droplets are present, after this the monomer concentration in the water phase drops below its saturation value, indicating the end of the growth interval.

Interval III: Monomer Depletion

The polymerization process continues in the polymer particles. The monomer concentrations M_w and M_p decrease in parallel, and the rate of polymerization consequently decreases up to the end of the process.





Comments

- The rate of polymerization increases in interval I due to the increase of N_p :

$$R_p \propto N_p \frac{dv_p}{dt} = (R_I t) c \quad (5.18)$$

while it remains constant in interval II and decreases to zero in interval III. This leads to the sigmoidal behavior of the monomer conversion curve, whose derivative is proportional to R_p .

- We assumed that the polymer particles do not coagulate, since they are kept colloidally stable through the addition of surfactant during the polymerization. If we add all the emulsifier at the beginning we make a lot of micelles, therefore many small particles with a large surface that most likely leads to coagulation.

5.6 Kinetics of Micellar Particle Nucleation

During intervals I and II, the growth of the volume of a single particle, v_p is given by 5.15:

$$\frac{dv_p}{dt} = k_p \frac{\phi^*}{1 - \phi^*} \frac{\bar{n}}{N_A} \frac{\rho_{\text{mon}}}{\rho_{\text{pol}}}$$

Since in these intervals $\phi^* = \text{const.}$ and we can assume $\bar{n} = 0.5$, the quantity above is equal to a constant:

$$\frac{dv_p}{dt} = c \quad (5.19)$$

CHAPTER 5. HETEROGENEOUS FREE-RADICAL POLYMERIZATION

If we assume that the nucleation interval is very short, we can approximate that all the radicals produced by the initiator, R_I enter the micelles, so that:

$$\frac{dN_p}{dt} = R_I \quad (5.20)$$

where neglecting the initiator consumption we have that R_I is constant.

The nucleation stops when the micelles disappear, that is when all emulsifier is adsorbed on the polymer particles. By taking $K_E \gg 1$, the emulsifier adsorption isotherm simplifies to $\Gamma_E = \Gamma_E^\infty$ and the condition for the end of the nucleation interval reduces to:

$$N_{pf} v_{pf} \Gamma_E^\infty = E^0 - cmc \approx E^0 \quad (5.21)$$

where E^0 is the overall concentration of emulsifier originally introduced in the reactor while N_{pf} is the final value of the number of polymer particles per unit volume of water, N_p , and t_f is the time at the end interval I. Since $\Gamma_E^\infty = a_p/a_E N_A$ we obtain:

$$N_{pf} v_{pf} a_{pf} = N_{pf} s_{pf} = E^0 a_E N_A \quad (5.22)$$

Using equations (5.19) and (5.20) we have:

$$N_{pf} = R_I t_f \quad v_{pf} = c t_f \quad (5.23)$$

Note that

$$\left. \begin{aligned} s_p &= 4\pi r_p^2 \\ v_p &= \frac{4}{3}\pi r_p^3 \end{aligned} \right\} \Rightarrow s_p = (36\pi)^{\frac{1}{3}} v_p^{\frac{2}{3}} \quad (5.24)$$

$$\Rightarrow N_{pf} (36\pi)^{\frac{1}{3}} v_{pf}^{\frac{2}{3}} = E^0 a_E N_A \quad (5.25)$$

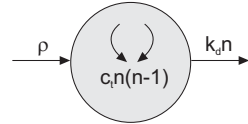
$$v_{pf} = c t_f = c \frac{N_{pf}}{R_I} \quad (5.26)$$

$$\begin{aligned} N_{pf} (36\pi)^{\frac{1}{3}} c^{\frac{2}{3}} \left(\frac{N_{pf}}{R_I} \right)^{\frac{2}{3}} &= E^0 a_E N_A \\ \Rightarrow N_{pf}^{\frac{5}{3}} &= E^0 a_E N_A \left(\frac{R_I}{c} \right)^{\frac{2}{3}} \frac{1}{(36\pi)^{\frac{1}{3}}} \\ \Rightarrow N_{pf} &= \left(E^0 a_E N_A \right)^{\frac{3}{5}} \left(\frac{R_I \rho_p N_A}{k_p \bar{n} M_p M_{mon}^m} \right)^{\frac{2}{5}} \frac{1}{(36\pi)^{\frac{1}{5}}} \end{aligned} \quad (5.27)$$

We conclude that the final number of particles per unit volume of water grows with the power of 0.6 of the initial emulsifier concentration, E^0 and the power 0.4 of the initial initiator concentration, I^0 .

5.7 Distribution of Active Radicals in the Polymer Particles

The following physicochemical steps are involved in the process:



- Radical entry from the aqueous phase:

$$\frac{\text{rad.}}{\text{time} \times \text{part.}} = k_e R_w^\bullet s_p N_A \equiv \rho \quad (5.28)$$

where k_e is the mass transfer coefficient of the radicals from the water into the polymer particles.

- Radical desorption from the polymer particles:

$$\frac{\text{rad.}}{\text{time} \times \text{part.}} = k_d \frac{n}{v_p N_A} v_p N_A \equiv k_d n \quad (5.29)$$

where k_d is the mass transfer coefficient of the radicals exiting the particles. Note that this is usually associated with a chain transfer to monomer event, which, if the monomer is water soluble, produces a soluble radical.

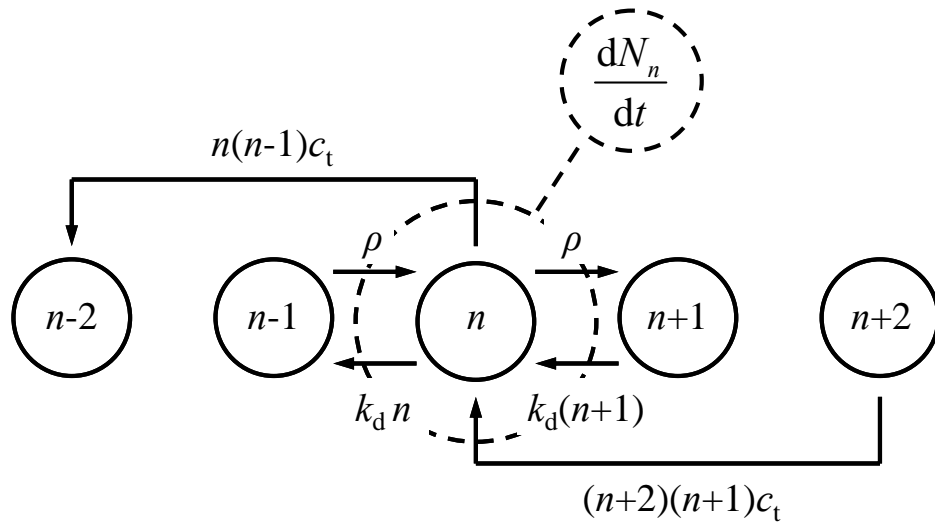
- Radical termination in polymer particles:

$$\frac{\text{events}}{\text{time} \times \text{part.}} = k_t \frac{n}{v_p N_A} \frac{(n-1)}{v_p N_A} \frac{1}{2} v_p N_A \equiv c_t (n-1) n \quad (5.30)$$

where c_t is the inverse of the termination characteristic time in the polymer particles.

Now we consider a population balance for polymer particles that at time t contain n active radicals:

$$\begin{aligned} \frac{dN_n}{dt} &= \rho N_{n-1} + k_d (n+1) N_{n+1} + c_t (n+2)(n+1) N_{n+2} \\ &\quad - \rho N_n - k_d n N_n - c_t n (n-1) N_n \end{aligned} \quad (5.31)$$



Let us introduce the PSSA for N_n and two new parameters:

$$m = \frac{k_d}{c_t} \quad \text{and} \quad \alpha = \frac{\rho}{c_t} \quad (5.32)$$

so we get:

$$\begin{aligned} \alpha N_{n-1} + m(n+1)N_{n+1} + (n+2)(n+1)N_{n+2} \\ = (\alpha + mn + n(n-1)) N_n \end{aligned} \quad (5.33)$$

The solution has been found in terms of modified Bessel functions (Stockmayer, 1957):

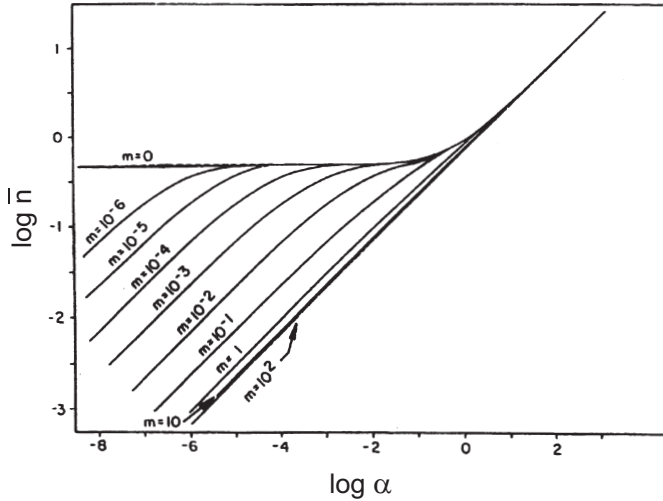
$$N_n = N_p a^n 2^{(m-1-3n)/2} \left(\frac{I_{m+n-1}(a/\sqrt{2})}{n! I_{m-1}(a)} \right) \quad (5.34)$$

with $a = \sqrt{8\alpha}$, and the average number of radicals per particle:

$$\bar{n} = \frac{\sum_{n=0}^{\infty} n N_n}{\sum_{n=0}^{\infty} N_n} \quad (5.35)$$

Let us first consider the case with no desorption, i.e., $m = 0$. We see that as $\alpha \rightarrow 0$ or $\rho \ll c_t$ (which is equivalent to $\tau_e \gg \tau_t$ in section 5.2) we have $\bar{n} \rightarrow 0.5$. From the PBE above for $m = \alpha = 0$ we have:

$$N_{n+2} = \frac{n(n-1)}{(n+2)(n+1)} N_n \quad (5.36)$$



which implies, for $n = 0, 1, 2 \dots$ that $N_2 = N_3 = \dots = 0$. For computing N_0 and N_1 we use the closure equation:

If a radical enters a particle with the maximum number of radicals, then it terminates immediately.

$$\begin{cases} \frac{dN_0}{dt} = -\rho N_0 + \rho N_1 \\ \frac{dN_1}{dt} = \rho N_0 - \rho N_1 \end{cases} \Rightarrow N_0 = N_1 = \frac{1}{2}N_p \quad (5.37)$$

that is $\bar{n} = 0.5$. In this case we have a so-called 0-1 system, that is one where half of the particles have zero radicals and the other half one.

In order to appreciate the influence of radical segregation on its average number, let us consider a bulk model, where we assume $n \gg 1$, and then $n(n - 1) \approx n^2$. In this case the balance of the radicals in a particle reduces to:

$$\frac{dn}{dt} = \rho - 2c_t n^2 - k_d n \quad (5.38)$$

and using the PSSA for n and introducing the above dimensionless parameters we obtain:

$$\alpha - 2n^2 - mn = 0 \quad (5.39)$$

which in turn leads to:

$$n = \frac{-m \pm \sqrt{m^2 + 8\alpha}}{4} \quad (5.40)$$

CHAPTER 5. HETEROGENEOUS FREE-RADICAL POLYMERIZATION

where the negative root is meaningless. The bulk model approximation above is valid when termination is low, so that we can have radical accumulation in the particle. In this case:

$$-m + \sqrt{m^2 + 8\alpha} \rightarrow \sqrt{8\alpha} \quad (5.41)$$

and therefore

$$n \rightarrow \sqrt{\alpha/2} \quad (5.42)$$

which is independent of the desorption rate and approaches the straight line emerging for $\alpha \rightarrow \infty$ appearing in the plot above, computed in the case of radical segregation. We conclude that for $\bar{n} \geq 3$ the polymer particles behave like a bulk (non segregated) system.

Thus depending on the value of α the system can approach a segregated behavior ($\alpha \ll 1$) or a bulk one ($\alpha \gg 1$). The first one occurs because, even if termination is very fast ($c_t \rightarrow \infty$), as a single radical in a particle cannot terminate. Accordingly, the limit for $\alpha \rightarrow 0$ is $\bar{n} = 0.5$ and not $\bar{n} = 0$. However, this is not true when desorption is present, since even a radical which is alone in the particle can desorb. Desorption becomes important when $m > \alpha$, as it is indicated in the figure where it is seen that straight lines indicating \bar{n} deviate from the segregated value $\bar{n} = 0.5$ at α values below the specific m under examination. Note that since in these conditions bimolecular termination cannot occur we can use the bulk model:

$$\frac{dn}{dt} = \rho - k_d n \approx 0 \quad (5.43)$$

which leads to

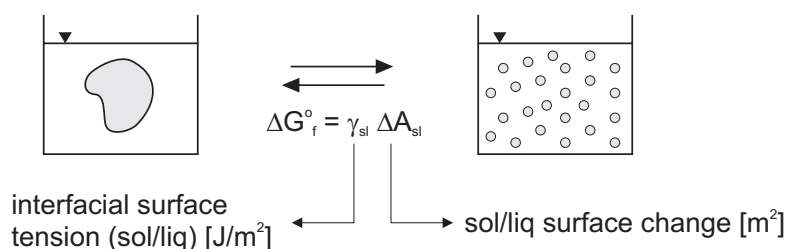
$$n = \frac{\alpha}{m} \quad (5.44)$$

which justifies the straight lines with slope equal to one in the figure above which describe the system behavior in the region dominated by radical desorption.

Chapter 6

Stability of Colloidal Suspensions

6.1 Kinetic Stability of Colloidal Suspensions



$\gamma_{sl} > 0 \Rightarrow$ colloid state is unstable, i.e., lyophobic (in water: hydrophobic); you need work to create a dispersion (\Rightarrow mixing)

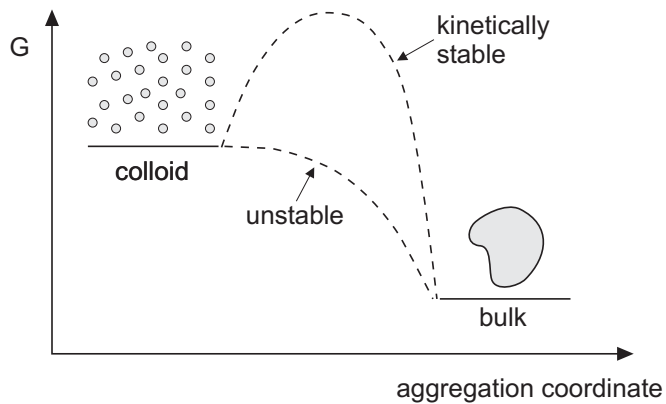
$\gamma_{sl} < 0 \Rightarrow$ colloid state is stable, i.e., lyophilic (in water: hydrophilic)

Lyophobic colloids can be made kinetically stable by building an energy barrier sufficiently large with respect to the thermal energy of the particles, kT . Two stabilization mechanisms are possible:

- electrostatic: the particles are electrically charged
- steric: the particles are coated with some material (e.g. polymer) which prevents their close approach.

Concept of Kinetic Stability

Thermal energy provides kinetic energy to the colloidal particles which collide with energy (kT). The charges on the particle surface provide an energy barrier to be overcome in order to have aggregation.



6.2 Interaction between two Charged Bodies

The interaction between two bodies is dominated by two forces, an attractive van der Waals force and a repulsive electrostatic force.

6.2.1 van der Waals Forces

The origin of these forces is the attraction between a temporary dipole and the corresponding induced dipoles (London theory). The following semi-quantitative argument provides a reasonably accurate picture of the physics underlying these interactions. Let us use the Bohr model for a hydrogen atom, where electrons are regarded as traveling in well defined orbits around nuclei. As a result of the electrons motion, every atom has an instantaneous dipole moment p approximately equal to $p = a_0 * e$, where e is the electron charge and a_0 is the Bohr radius, which is a good estimate of the radius of a hydrogen atom. Let us consider two hydrogen atoms, referred to as atom 1 and atom 2, positioned at a distance R . The electric field E generated by the instantaneous dipole 1 at distance R is given by:

$$E = \frac{p_1}{4\pi\epsilon_0 R^3} \quad (6.1)$$

where ϵ_0 is the vacuum dielectric permeability. Atom 2, will be polarized by the electric field generated by atom 1, which generates an induced dipole of strength:

$$p_2 = \alpha E = \frac{\alpha p_1}{4\pi\epsilon_0 R^3} \quad (6.2)$$

CHAPTER 6. STABILITY OF COLLOIDAL SUSPENSIONS

where α is the polarizability of the second atom, and is approximately equal to $\alpha = 4\pi\epsilon_0 a_0^3$. Since the energy of interaction of two dipoles equals:

$$V_{\text{int}} = -\frac{p_1 p_2}{4\pi\epsilon_0 R^3} = -\frac{\alpha a_0^2 e^2}{(4\pi\epsilon_0)^2 R^6} = -\frac{C}{R^6} \quad (6.3)$$

Equation (6.3) shows that van der Waals interactions between pairs of particles in vacuum are always attractive, and decay very strongly with the distance. However, they become considerable at short distances.

When the overall van der Waals interactions between macroscopic objects needs to be computed, one assumes that equation (6.3) holds for all pairs of molecules contained in the two objects. This theory has been developed by Hamaker. In this case, the van der Waals interaction between macroscopic object 1 and macroscopic object 2 is given by:

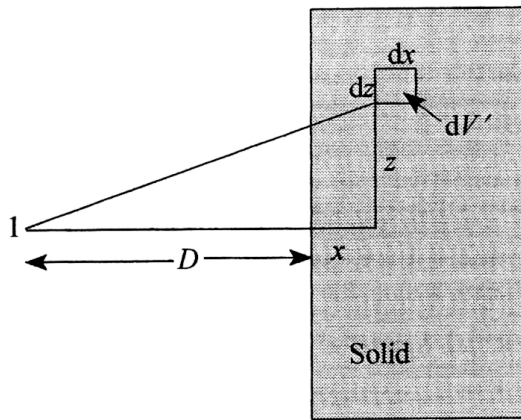
$$V_A = -C \int_{V_1} \int_{V_2} \frac{dV_1 dV_2}{R^6} \quad (6.4)$$

where the two integrations run over the entire volumes V_1 and V_2 of the two bodies, and R is the distance between two arbitrary points, one located within the first object, the other one within the second object. Generally, the two integrals are difficult to compute, and explicit formulas are available only for very simple geometries. As an example, let us perform the integration for the case of a semi-infinite solid and a point. Equation (6.4) reduces in this case to one single volume integral, over the semi-infinite body. If we indicate with d the distance between the point (named 1) and the surface of the semi-infinite body, and we define a coordinate system with the x -axis along the direction of the distance d , with the zero on the surface of the body and pointing inwards the body and both other axes parallel to its surface, one can immediately recognize that the system has a rotational symmetry around the x -axis. It is therefore convenient to perform the volume integration using cylindrical coordinates. The distance R in equation (6.4) is equal to the distance between point 1 and an arbitrary point having coordinates x and z inside the body, as shown in the next Figure. By making use of Pitagora's theorem, the volume integral in equation (6.4) reduces to:

$$V_A = -C \int_0^\infty dx \int_0^\infty \frac{2\pi z dz}{(z^2 + (d+x)^2)^3} = -\frac{\pi C}{2} \int_0^\infty \frac{dx}{(d+x)^4} = -\frac{\pi C}{6d^3} \quad (6.5)$$

From equation (6.5) one can observe that the dependence of the van der Waals interactions between a point and an infinite solid decreases as the reverse third power of the distance.

The simple calculation shows the effect of summing in a pair additive manner the interactions of all pairs of molecules belonging to two macroscopic objects. Even though the



interactions of two molecules are very weak, the overall interactions between the bodies can become significant at short distances, for example at distances comparable to the size of the two objects.

There are two important cases where the integrations in equation (6.4) can be performed analytically: (1) two infinite slabs and (2) two spheres having arbitrary size and distance. The corresponding interaction potentials can be computed as follows:

- For two infinite slabs at distance D :

$$V_A(D) = -\frac{A}{12\pi D^2} \quad (6.6)$$

- For two spheres of radius a_1 and a_2 at distance R :

$$V_A(R) = -\frac{A}{6} \left[\frac{2a_1 a_2}{R^2 - (a_1 + a_2)^2} + \frac{2a_1 a_2}{R^2 - (a_1 - a_2)^2} + \ln \left(\frac{R^2 - (a_1 + a_2)^2}{R^2 - (a_1 - a_2)^2} \right) \right] \quad (6.7)$$

where A is the Hamaker constant which depends on the physical characteristics, e.g., polarizability and density, of the materials involved. In the case of two spheres, one can perform Taylor expansions of this last equation and observe that at distances much smaller than the particle radius, the interactions decay with the first power of the distance. On the other hand, for distances much larger than the particle radius the interaction energy decays with the sixth power of the distance, as one could expect.

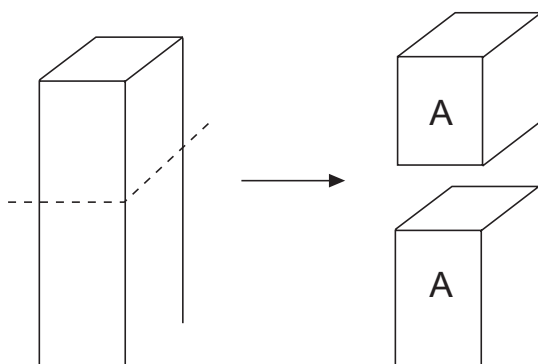
The Hamaker constant depends not only on the physical properties of the materials the macroscopic objects are made of, but also on the dielectric properties of the medium surrounding the particles. The effect of this medium can be extremely important in some cases.

CHAPTER 6. STABILITY OF COLLOIDAL SUSPENSIONS

In fact, even though Hamaker constants are usually positive, there are some cases where negative values can be found for some specific types of materials/medium pairs. A negative value of Hamaker constant implies that van der Waals interactions are repulsive.

One final caveat about Hamaker's treatment of van der Waals interactions. A much more rigorous approach of dispersion forces and van der Waals forces is available in the literature, which has been pioneered by Lifshitz. It is based on rigorous quantum mechanical calculations, but the final equations are far more complex than the Hamaker theory. However, some general features can be quickly discussed, which are necessary to point out the limitations of the simpler Hamaker theory. First of all, Lifshitz' theory shows that the pairwise addition of interactions is not rigorously correct, as van der Waals interactions a truly many-body problem. This effect can be simply accounted for by adjusting the values of the Hamaker constant. The second limitation is given by the so-called retardation effect. Since atoms are fluctuating dipoles, as the distance between two molecules increases beyond a certain threshold, the time required for a molecule to feel the effect of the electric field produced by another dipole becomes significant. This implies that the interactions of the different dipoles are retarded, and the energy of interaction decays even stronger with the distance, i.e., with the seventh power of the distance, and not anymore with the sixth power. This effect weakens van der Waals interactions for large bodies as their distance increases, compared to the predictions of the Hamaker theory. However, due to its simplicity and good accuracy, Hamaker constants are still commonly used in colloidal science.

Concept of Surface Tension



W_{AA} = work per unit area needed to separate up to ∞ two parts of liquid column

$$W_{AA} = 2\gamma_{Av} \quad (6.8)$$

where γ_{Av} is the surface tension of A in contact with vapor (vacuum). We compute W_{AA} as the interaction energy between two flat bodies and get (for hydrocarbons):

$$\gamma_{Av} = \frac{1}{2} W_{AA} = \frac{1}{2} \cdot \frac{A}{12\pi L^2} \quad (6.9)$$

Since it is difficult to postulate L , we compute it from experimental values of γ_{Av} and calculated A .

Alkane C_nH_{2n+2}

n	$10^{20} \times A$ (J)	$10^3 \times \gamma_{Av}$ (J/m ²)	$10^{-3} \times \rho$ (kg/m ³)	L (nm)
5	3.75	16.05	0.626	0.176
6	4.07	18.40	0.660	0.171
8	4.50	21.62	0.702	0.166
10	4.82	23.83	0.730	0.164
12	5.03	25.35	0.749	0.162
14	5.05	26.56	0.763	0.159
16	5.23	24.47	0.773	0.159

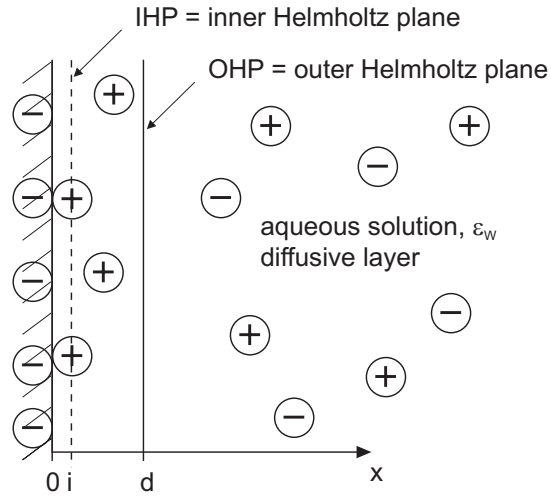
We observe that L :

- i) has dimension of molecular radius
- ii) $L \propto 1/\sqrt{\rho}$.

6.2.2 Electrostatic Forces

Electrical Double Layer

- Outside of the outer Helmholtz plane, the ions move freely, therefore this is the plane of closest approach of (hydrated) ions (≈ 0.5 nm).
- The inner Helmholtz plane constitutes the locus of the centers of adsorbed (dehydrated) ions (≈ 0.1 nm).



For $x > 0$:

$$\left. \begin{array}{l} \rho = \text{div}(\varepsilon E) \\ E = -\text{grad}(\psi) \end{array} \right\} \Rightarrow \nabla^2(\psi) = -\frac{\rho}{\varepsilon} \quad \left(\begin{array}{l} \text{Poisson} \\ \text{equation} \end{array} \right) \quad (6.10)$$

where $\rho = \sum_{\text{all ions}} n_i z_i e$, with n_i = number ion concentration, z_i = valance, e = electron charge;

E = electric field

ε = permittivity

ψ = potential referred to bulk, i.e., $\psi = 0$ at $x = \infty$.

For $x > d$:

The ions are free to diffuse and are influenced by the local electrostatic potential, so that:

$$n_i = n_i^0 \exp\left(-\frac{z_i e \psi}{kT}\right) \quad \left(\begin{array}{l} \text{Boltzmann} \\ \text{equation} \end{array} \right) \quad (6.11)$$

where n_i^0 is n_i in the bulk. In the diffusive layer, $x > d$, we have $\varepsilon = \varepsilon_w$ and:

$$\nabla^2(\psi) = -\frac{1}{\varepsilon_w} \sum n_i^0 z_i e \exp\left(-\frac{z_i e \psi}{kT}\right) \quad \left(\begin{array}{l} \text{Poisson-Boltzmann} \\ \text{equation} \end{array} \right) \quad (6.12)$$

with B.C.: $\psi = 0$ at $x = \infty$, $\psi = \psi_d$ at $x = d$.

Let us consider a few specific cases for which we have analytical solutions.

- The Debye-Hückel approximation:

Applies when the electrical energy is small compared to the thermal energy: $|z_i e \psi| < kT$.

Then,

$$\exp\left(-\frac{z_i e \psi}{kT}\right) \approx 1 - \frac{z_i e \psi}{kT} \quad (6.13)$$

which leads to

$$\nabla^2 \psi = -\frac{1}{\varepsilon_w} \left(\sum n_i^0 z_i e - \frac{\sum n_i^0 z_i^2 e^2}{kT} \psi \right) \quad (6.14)$$

According to the principle of electroneutrality for the bulk $\sum n_i^0 z_i = 0$ and, therefore, we get

$$\nabla^2 \psi = \kappa^2 \psi \quad (6.15)$$

where

$$\kappa^2 = \frac{1}{\varepsilon_w} \frac{\sum n_i^0 z_i^2 e^2}{kT} \quad (6.16)$$

is the Debye-Hückel parameter. The solution has the form

$$\psi = A_1 \exp(\kappa x) + A_2 \exp(-\kappa x) \quad (6.17)$$

but since $\psi = 0$ as $x \rightarrow \infty$, $\Rightarrow A_1 = 0$ and imposing $\psi = \psi_d$ at $x = d \Rightarrow A_2 = \psi_d \exp(\kappa d)$, so that

$$\psi = \psi_d \exp[-\kappa(x - d)] \quad , \text{ for } x > d \quad (6.18)$$

The distance $1/\kappa$ where $\psi = \psi_d \exp(-1)$ is defined as the thickness of the diffusive layer. At 25°C in water

$$\kappa = 3.29 \sqrt{I} \quad [\text{nm}^{-1}] \quad (6.19)$$

with $I = 1/2 \sum c_i z_i^2$ is the ionic strength and c_i is in mol/L. For example, for a 10^{-3} M, 1:1 electrolyte is $1/\kappa = 9.6$ nm.

- Flat surface:

We consider a symmetric electrolyte, $z_+ = -z_- = z$ and $n_+^0 = n_-^0 = n^0$, so that the Poisson-Boltzmann equation becomes

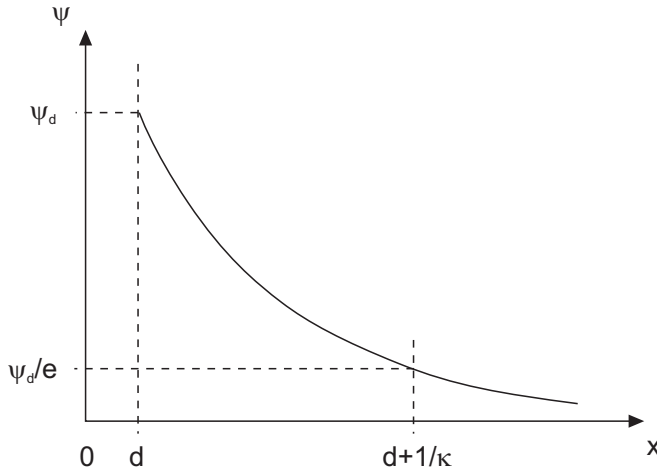
$$\begin{aligned} \nabla^2 \psi &= -\frac{1}{\varepsilon_w} n^0 z e \exp\left(-\frac{ze\psi}{kT}\right) + \frac{1}{\varepsilon_w} n^0 z e \exp\left(+\frac{ze\psi}{kT}\right) \\ &= \frac{2n^0 z e}{\varepsilon_w} \sinh\left(\frac{ze\psi}{kT}\right) \end{aligned} \quad (6.20)$$

and then for a flat geometry

$$\frac{d^2 \psi}{dx^2} = \frac{2n^0 z e}{\varepsilon_w} \sinh\left(\frac{ze\psi}{kT}\right) \quad (6.21)$$

Multiplying both sides by $(2d\psi/dx)$ and integrating in x :

$$\int 2 \frac{d\psi}{dx} \frac{d^2 \psi}{dx^2} dx = \frac{4n^0 z e}{\varepsilon_w} \int \sinh\left(\frac{ze\psi}{kT}\right) \frac{d\psi}{dx} dx \quad (6.22)$$



$$\int_{\infty}^x \frac{d}{dx} \left(\frac{d\psi}{dx} \right)^2 dx = \frac{4n^0 ze}{\varepsilon_w} \int_0^\psi \sinh \left(\frac{ze\psi}{kT} \right) d\psi \quad (6.23)$$

where we account for the B.C.: $\psi = 0$ and $d\psi/dx = 0$ at $x = \infty$

$$\left(\frac{d\psi}{dx} \right)^2 = \frac{4n^0 ze}{\varepsilon_w} \left| \frac{kT}{ze} \cosh \left(\frac{ze\psi}{kT} \right) \right|_0^\psi \quad (6.24)$$

$$\left(\frac{d\psi}{dx} \right)^2 = \frac{4n^0 kT}{\varepsilon_w} \left[\cosh \left(\frac{ze\psi}{kT} \right) - 1 \right] \quad (6.25)$$

Recalling that $\sqrt{\cosh(a\psi) - 1} = -\sqrt{2} \sinh(a\psi/2)$, we get

$$\frac{d\psi}{dx} = - \left(\frac{8n^0 kT}{\varepsilon_w} \right)^{\frac{1}{2}} \sinh \left(\frac{ze\psi}{2kT} \right) \quad (6.26)$$

This can be integrated by variable separation as follows:

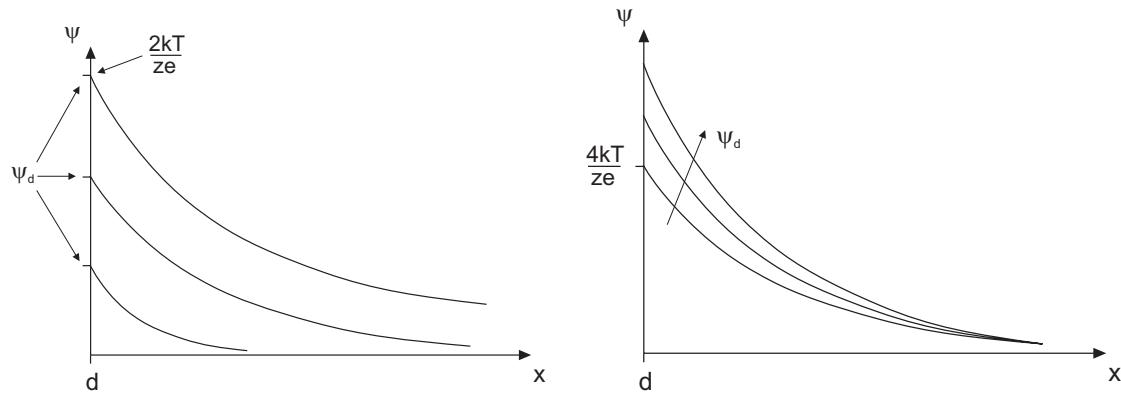
$$\int_{\psi_d}^\psi \frac{d\psi}{\sinh(z\psi/2kT)} = - \frac{2\kappa kT}{ze} \int_d^x dx \quad (6.27)$$

$$\Rightarrow \tanh \left(\frac{ze\psi}{4kT} \right) = \tanh \left(\frac{ze\psi_d}{4kT} \right) \exp [-\kappa(x-d)] \quad (6.28)$$

In the case where $ze\psi < kT$, we can approximate $\tanh(ze\psi/4kT) \approx ze\psi/4kT$, and the solution above becomes

$$\psi = \psi_d \exp [-\kappa(x-d)] \quad (6.29)$$

which is the Debye-Hückel approximate solution.



a) Approximate behavior:

$$\text{for } \psi_d < 2 \frac{kT}{ze} \Rightarrow \psi \approx \psi_d \exp[-\kappa(x-d)]$$

$$\text{for } \psi_d > 4 \frac{kT}{ze} \Rightarrow \tanh\left(\frac{ze\psi}{4kT}\right) \approx \exp[-\kappa(x-d)]$$

(since $\tanh(y) \rightarrow 1$ as $y \rightarrow \infty$)

which sufficiently away from the surface, where ψ is small, leads to

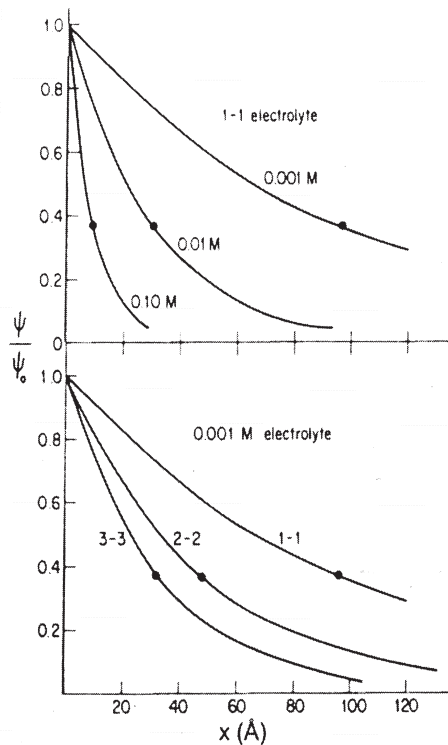
$$\psi = \frac{4kT}{ze} \exp[-\kappa(x-d)] \quad (6.30)$$

that is away from the surface the potential behaves like in the case where $\psi_d = 4kT/ze$, although ψ_d is much larger.

b) If we take $d = 0$, and ignore the IHP and OHP, this treatment corresponds to the Gouy and Chapman model. The figures show the effect of electrolyte charge and concentration on the potential behavior predicted by Debye-Hückel. The points indicate the value $\psi/\psi_d = \exp(-1)$ and the corresponding Debye thickness $1/\kappa$.

$1/\kappa$	$C_{\text{electrolyte}}$
9.60 nm	0.001 M
3.00 nm	0.01 M
0.96 nm	0.1 M

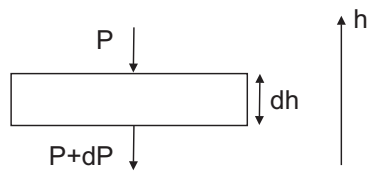
It is seen that both the electrolyte concentration and its charge can strongly affect the thickness of the double layer. This is known as double layer compression and is widely used in applications to destabilize colloids. However, the predictions of this model on a quantitative basis are often unrealistic. For example in the case of $\psi_d = 100$ mV with



$n^0 = 0.001 \text{ M}$, a surface concentration value $n_d = n^0 \exp(ze\psi_d/kT) = 0.001 \exp(12) = 160 \text{ M}$ is obtained. This result can be corrected introducing the Stern layer, where some counterions are strongly associated with the surface, thus also neutralizing some of the surface ions.

Simple Example for a BOLTZMANN Distribution

Let us consider the molecules in the atmosphere which are free to move according to Brownian motion but are also subject to the gravitational field.



By applying Newton law to a thin slice of atmosphere dh we get:

$$dP = -\rho g dh \quad (6.31)$$

CHAPTER 6. STABILITY OF COLLOIDAL SUSPENSIONS

where ρ is the mass density which using the ideal gas law can be expressed as follows:

$$\rho = nM = \frac{PM}{RT} \quad (6.32)$$

where M is the molecular weight and n is the number molecule concentration. Substituting in the previous equation this leads to:

$$\frac{dP}{P} = -\frac{Mg}{RT} dh \quad (6.33)$$

which integrated with I.C.: $P = P_0$ at $h = 0$ yields:

$$P = P_0 \exp\left(-\frac{Mg}{RT} h\right) \quad (6.34)$$

Recalling that $M = mN_A$, where m is the molecule mass and N_A the Avogadro number, while $R = kN_A$ and pressure is proportional to the number molecule concentration the above equation leads to:

$$n = n_0 \exp\left(-\frac{mgh}{kT}\right) \quad (6.35)$$

which, since (mgh) is the gravitational potential, coincides with the Boltzmann equation (6.6).

A More Rigorous Derivation of the BOLTZMANN Distribution

In order to fully justify the use of the Boltzmann distribution to describe the dependence of the concentration of ions on the electrostatic potential, let us consider the following thermodynamic argument. In the presence of a charged surface, which generates an electric field, the thermodynamic function which determines the equilibrium condition of the ions is the electrochemical potential $\tilde{\mu}$, defined as:

$$\tilde{\mu} = \mu + z e \psi \quad (6.36)$$

where z is the valence of the ion, ψ is the electrostatic potential at the location considered and μ is the chemical potential. The significance of the electrochemical potential is that of free energy per molecule in the presence of electric field. For every ion, the electrochemical potential has to be constant in the entire space in order to guarantee the thermodynamic equilibrium. Therefore, by considering two different locations, one at distance x from the surface, where the electrostatic potential is $\psi(x)$, and the other one in the bulk of the solution, at infinite distance from the surface, where the electrostatic potential is equal to zero, the equilibrium conditions reads:

$$\tilde{\mu}(x) = \mu(x) + z e \psi(x) = \tilde{\mu}(x = \infty) = \mu(x = \infty) \quad (6.37)$$

CHAPTER 6. STABILITY OF COLLOIDAL SUSPENSIONS

By using the definition of chemical potential:

$$\mu(x) = \mu_0 + kT \ln(a(x)) \quad (6.38)$$

where $a(x)$ is the activity of the species at a distance x from the surface and μ_0 is a reference chemical potential. By neglecting concentration effects, we can replace the activity by the number concentration, i.e., $a(x) \approx n(x)$. Therefore, by calling n_0 the number concentration of the ion in the bulk of the solution, equation (6.37) becomes:

$$kT \ln(n(x)) + ze\psi = kT \ln(n_0) \quad (6.39)$$

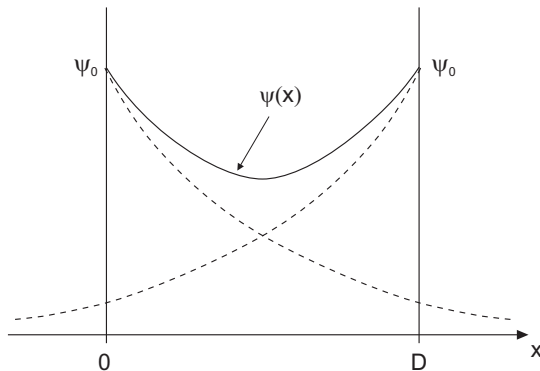
which leads to the Boltzmann distribution of the ion:

$$n(x) = n_0 \exp\left(-\frac{ze\psi}{kT}\right) \quad (6.40)$$

Therefore, the Boltzmann distribution arises naturally (at least for dilute electrolyte solutions) as a consequence of thermodynamic equilibrium in the presence of an electric field.

Electrostatic Potential of Interaction

When two charged bodies approach each other the corresponding double layers overlap, the local ion concentration increases compared to the bulk, thus creating an osmotic pressure and therefore a corresponding repulsive force.



Depending on the kinetics of the approach we can have that the ions may have or not time enough to equilibrate. We distinguish three limiting situations:

- constant surface potential, $\psi_0 \Rightarrow$ slow approach;

- constant surface charge, $\sigma_0 \Rightarrow$ fast approach or ions covalently bound to the surface;
- charge regulation \Rightarrow the surface groups can dissociate to an extent which depends on the interaction, as for example:

$$\text{SH} \rightleftharpoons \text{S}^- + \text{H}^+ \Rightarrow \sigma_0 = -eS_s^- = \frac{-e\kappa_d N_s}{\kappa_d + \text{H}^{+0} \exp(-e\psi_0/kT)} \quad (6.41)$$

In order to compute the repulsive force between two charged infinite planar surfaces at a distance h , let us consider the following simple argument. At equilibrium, all forces acting on a volume element located between the two plates must balance. The only two forces acting are the electrostatic forces and the osmotic pressure. The osmotic pressure force per unit volume is equal to:

$$F_p = -\frac{dp}{dx} \quad (6.42)$$

where x is the coordinate perpendicular to the two surfaces. On the other hand, the electrostatic force per unit volume equals the product of the charge density with the electric field, and can be written as:

$$F_{el} = -\rho \frac{d\psi}{dx} \quad (6.43)$$

By using the Poisson equation, this force balance can be recast in the following form:

$$\frac{dp}{dx} - \epsilon \frac{d^2\psi}{dx^2} \frac{d\psi}{dx} = 0 \quad (6.44)$$

The integration of this equation gives:

$$p - \frac{\epsilon}{2} \left(\frac{d\psi}{dx} \right)^2 = \text{const.} \quad (6.45)$$

This last equation implies that the sum of the osmotic pressure and the so-called Maxwell pressure, $\epsilon/2 \cdot (d\psi/dx)^2$, are constant in the whole domain. Due to the symmetry of the system considered here, at the midplane the electrostatic potential profile has to have an extremum (minimum if the surface are positively charged, maximum otherwise). Therefore $(d\psi/dx)_{x=h/2} = 0$, and the constant in equation (6.45) is equal to the osmotic pressure at the midplane. Therefore, once the pressure at midplane is known, the force acting on the planes can be computed, and by integrating the force, the energy of interaction can be derived. In order to determine the pressure at midplane, we can once again use the force balance written as:

$$dp = -\rho d\psi \quad (6.46)$$

CHAPTER 6. STABILITY OF COLLOIDAL SUSPENSIONS

In order to simplify the calculations, let us assume to have a solution containing just a symmetric $z-z$ electrolyte. By making use of the Boltzmann distribution for the ions concentration, one obtains:

$$dp = 2zen_0 \sinh\left(-\frac{ze\psi}{kT}\right) d\psi \quad (6.47)$$

This equation can be easily integrated between the following limits: $p = p_0$ in the bulk (when $\psi = 0$), and $p = p_{h/2}$ at $\psi = \psi_{h/2}$. The result is the following:

$$p_{h/2} - p_0 = 2kTn_0 \left[\cosh\left(-\frac{ze\psi_{h/2}}{kT}\right) - 1 \right] = F_R \quad (6.48)$$

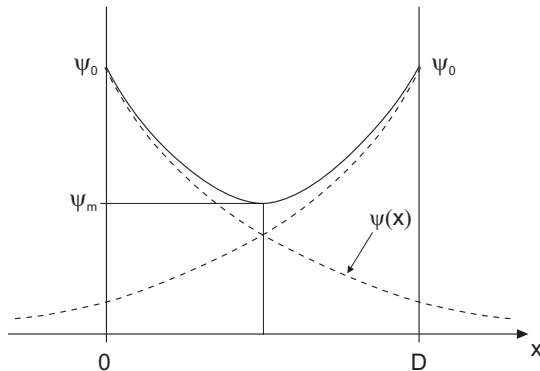
The conclusion is that the repulsive force between the planes can be computed if the potential at midplane is known. This can be obtained by integrating the Poisson-Boltzmann equation. One should then notice that the electrostatic repulsive energy (per unit surface) is obtained from the repulsive force per unit surface as follows:

$$dV_{el} = -F_R dh \quad (6.49)$$

The physical interpretation is that the potential energy per unit surface of two plates at a distance h is equal to minus the work done to bring the plates from infinite distance to the current distance h .

Several approximate relations have been developed to compute the electrostatic repulsive potentials between two bodies.

- For small degree of double layer overlap (any geometry), $D \gg 1/\kappa$:



$$V_R^\psi = \frac{64n^0 k T Z^2}{\kappa} \exp(-\kappa D) \quad (6.50)$$

$$Z = \tanh\left(\frac{ze\psi_0}{4kT}\right) \quad (6.51)$$

In this case $V_R^\sigma \approx V_R^\psi$ since the discharge remains anyway small due to the small overlap. This corresponds to the case where the potential at midplane is approximated by the sum of the potentials of two isolated charged infinite planes. This approximation is only valid for small overlapping.

- For small potentials of the two surfaces, $ze\psi_0 \ll kT$:

In this case we can apply the Debye-Hückel approximation

$$V_R^\psi = \frac{2n^0 kT}{\kappa} \left(\frac{ze\psi_0}{kT} \right)^2 \left[1 - \tanh\left(\frac{\kappa D}{2}\right) \right] \quad (6.52)$$

- Most convenient in applications are:

$$V_R^\psi = \frac{32n^0 kT}{\kappa} z^2 \left[1 - \tanh\left(\frac{\kappa D}{2}\right) \right] \quad (6.53)$$

$$V_R^\sigma = \frac{2n^0 kT}{\kappa} \left(2y_0 \ln \left[\frac{B + y_0 \coth(\kappa D/2)}{1 + y_0} \right] \right. \quad (6.54)$$

$$\left. - \ln \left[y_0^2 + \cosh(\kappa D) + B \sinh(\kappa D) + \kappa D \right] \right) \quad (6.55)$$

where $y_0 = ze\psi_0/kT$ and $B = [1 + y_0^2 \cosh^2(\kappa D/2)]^{1/2}$

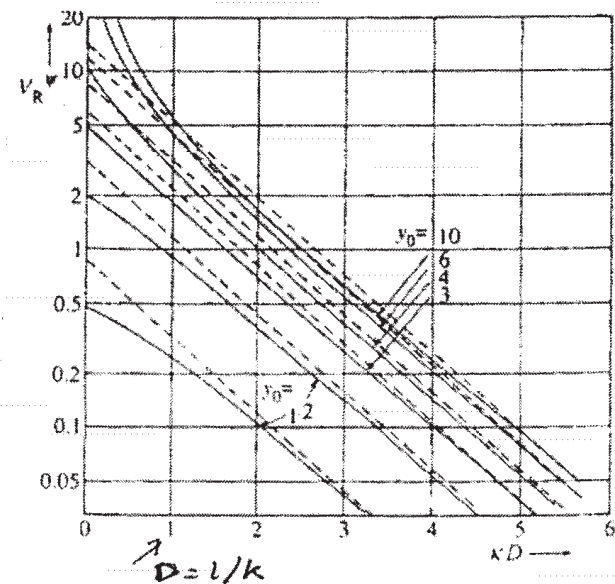
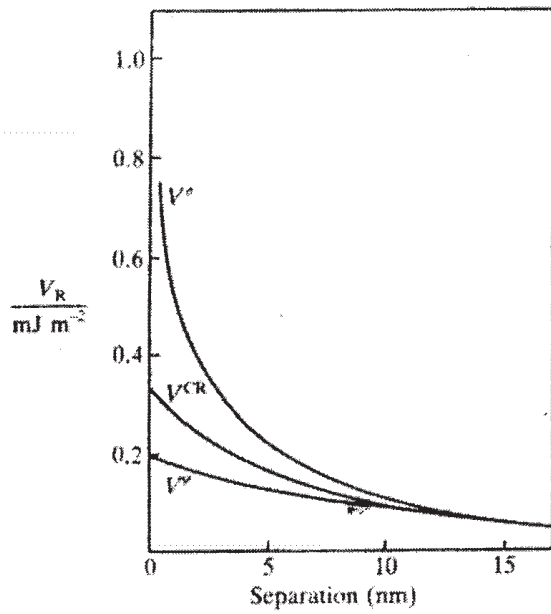
- Illustrations:

The figure above shows a comparison of the three repulsive potentials. The one for constant charge is clearly the largest, while the charge regulation solution is somehow intermediate. The next figure shows that V_R^ψ decreases with distance and with $y_0 = ze\psi_0/kT$. The approximate expression for $D \gg 1/\kappa$ (dotted) is compared with exact solution (solid).

Electrical Charge of a Surface

The most common way to bring charges on the surface of particles is to adsorb ionic surfactants. These can be salts which are fully dissociated (e.g. sodium dodecylsulfonate) or weak acids (e.g. carboxylic acids) that dissociate to an extent which depends upon the solution pH.

CHAPTER 6. STABILITY OF COLLOIDAL SUSPENSIONS



Another possibility is to act on the concentration of the so-called potential determining ions, as we discuss next.

When considering a dispersion of solid AgI particles in water, since the solution is saturated

CHAPTER 6. STABILITY OF COLLOIDAL SUSPENSIONS

we have:

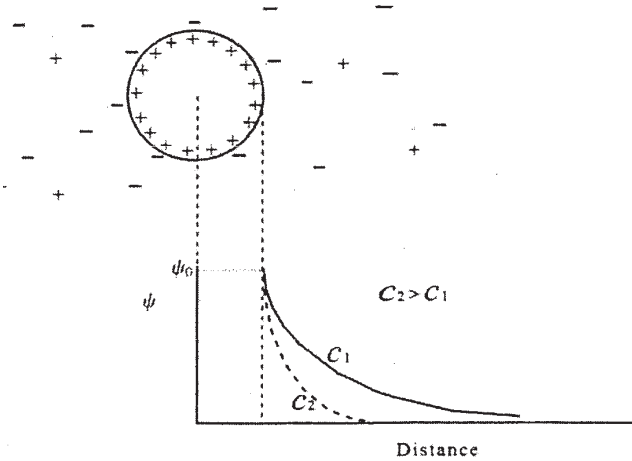
$$a_{\text{Ag}^+}^e a_{\text{I}^-}^e = K_s \quad (6.56)$$

where K_s is the solubility product. In addition, due to the solid-liquid equilibrium we have that the activities of each ion are equal in the two phases:

$$a_{\text{Ag}^+}^e = a_{\text{Ag}^+}^s \quad (6.57)$$

$$a_{\text{I}^-}^e = a_{\text{I}^-}^s s_{\text{I}^-} \quad (6.58)$$

This in general implies that, since the affinity of Ag^+ and I^- to the solid and solution is different, the particle acquires a charge. We can affect such particle charge by acting on the activity of the ions in the solution. If we add AgNO_3 , then a_{Ag^+} in solution increases and a_{I^-} has to decrease, thus increasing the positive particle charge. In this case Ag^+ and I^- are the potential-determining ions, and we can use them to control the particle charge and potential. The figure below shows the potential profile and the counterion distribution around a charged particle: they have to follow the potential distribution but thermal diffusion tends to uniformize them, the result is the diffusive electrical double layer. The thickness of this layer can be decreased by adding some other electrolyte, i.e., indifferent ions, as shown in the figure. This is the double layer compression which decreases the particle stability.



6.2.3 Total Interaction Energy

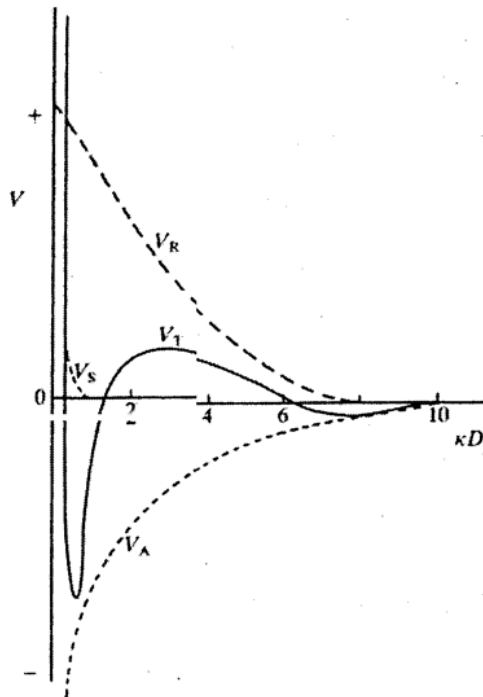
The total potential energy of interaction is given by the sum of the attractive and the repulsive contributions derived earlier:

$$V_T = V_A + V_R \quad (6.59)$$

Using expressions developed for flat surfaces and symmetric electrolyte, we get:

$$V_T = -\frac{A}{12\pi D^2} + \frac{32n^0 kT}{\kappa} z^2 \left[1 - \tanh\left(\frac{\kappa D}{2}\right) \right] \quad (6.60)$$

which is illustrated in the figure on the next page. It is seen that the van der Waals forces dominate at low distances, where however V_T does not go to $-\infty$, but contrary increases due to the occurrence of Born repulsion forces, which are very short-range and come into play when the atom of the two surfaces come in contact. This leads to the very deep attractive well, referred to as primary minimum. At high distances, the van der Waals forces prevail again, often leading to the formation of a secondary minimum.



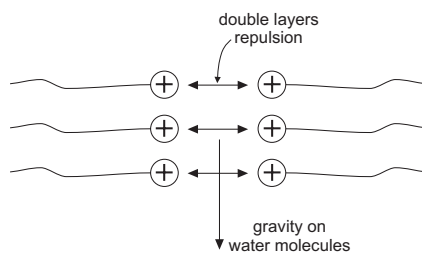
CHAPTER 6. STABILITY OF COLLOIDAL SUSPENSIONS

Note

Because of the large depth of the primary minimum the energy barrier for separating two particles is much larger, often substantially infinite, compared to that corresponding to the reverse process.

6.2.4 Simple Manifestation of Electrical Double Layers: Soap Films

The figure shows a soap film, where the water molecules are kept in the film by the repulsive forces between the layers of surfactant molecules adsorbed at the air-liquid interface.



For the film formed with a wire frame in the figure, at each height, H the hydrostatic pressure ($H\rho g$) which tends to drain the water molecules have to be balanced by the double-layer pressure, which corresponds to a certain thickness of the film, D that can be measured. For example at height of about $H = 10$ cm, the repulsive double-layer pressure has to be of the order of 10^3 N/m². Soap film thickness of about 20 nm were stabilized by the overlapping diffusive double layers with $\psi_0 \approx 30$ mV.

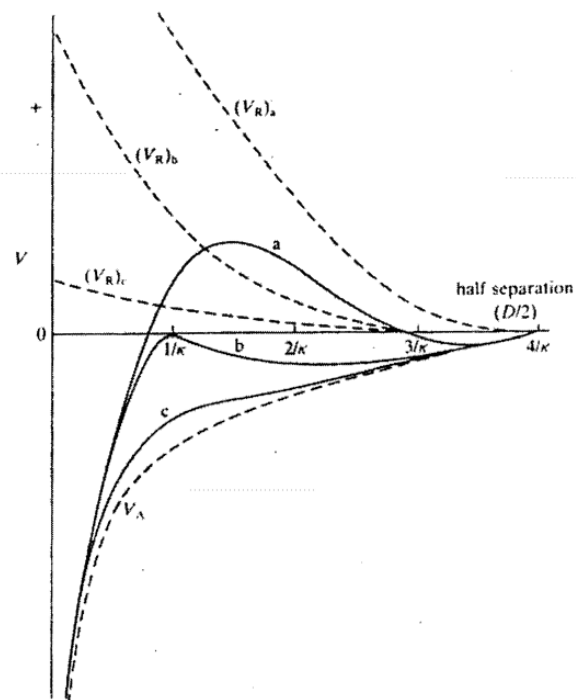
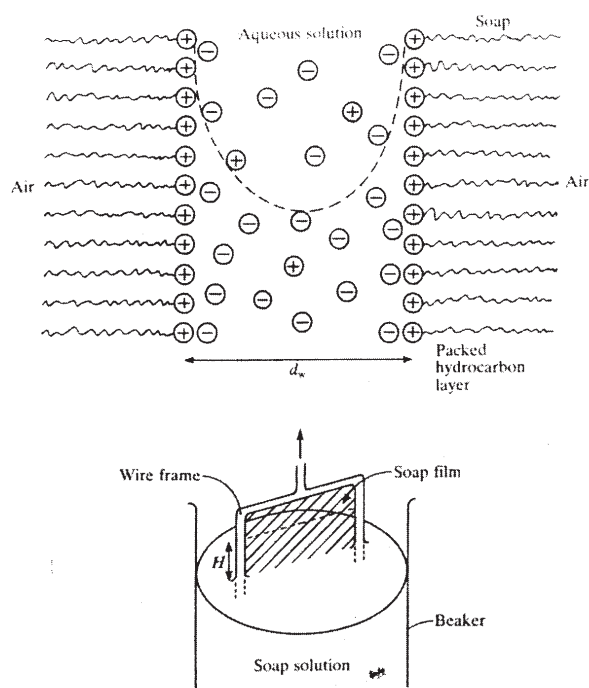
6.3 Coagulation of Colloidal Suspensions

From the shape of the total interaction potential curve as a function of particle distance we can define the stability of a colloid or a latex. This is illustrated in the figure below, where we have:

- a = kinetically stable or meta-stable colloid;
- b = marginally unstable (critical condition)
- c = unstable

The loss of stability, or particle aggregation, can be induced in two ways as described in the following.

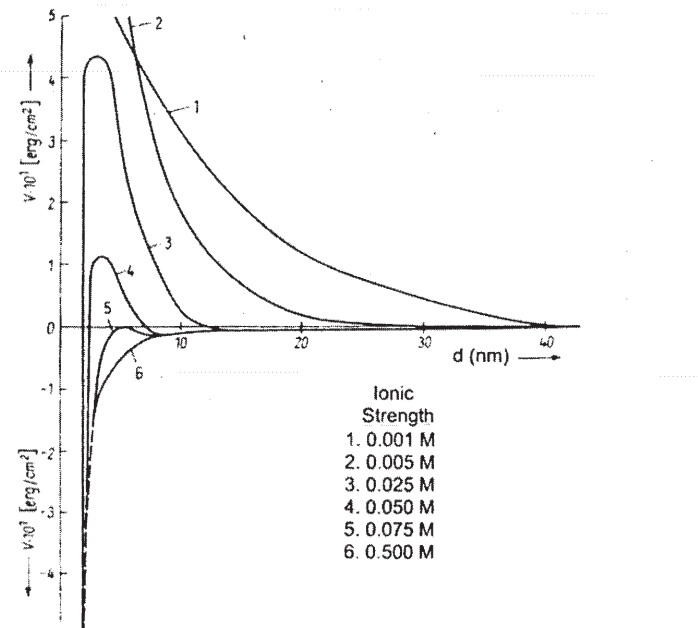
CHAPTER 6. STABILITY OF COLLOIDAL SUSPENSIONS



6.3.1 Aggregation by Potential Control

We can change the particle charge, and then its potential, as shown by the curves in the previous figure. This can be done by changing the activity of the potential determining ions. An example is given by the titration of a solution containing I^- using $AgNO_3$, based on the very low solubility of AgI . The first particles of AgI precipitated are in equilibrium with an excess of I^- in solution, therefore have a strong negative charge and are small and stable. This leads in fact to a milky dispersion. As we add more $AgNO_3$, more AgI precipitates and therefore the excess of I^- in solution decreases, together with the particle negative charge and stability. The colloidal particles start to aggregate leading to large flocs of AgI , which become visible. At some point the charge of the particle becomes zero, and after that they acquire a positive charge. By measuring particle migration in an electric field the potential at zero particle charge is found to be at $Ag^+ = 3.2 \times 10^{-6} M$, which being $K_s = 8 \times 10^{-17}$, corresponds to $I^- = 2.5 \times 10^{-11} M$ which is very small as required for titration.

6.3.2 Aggregation by Electrolyte Addition



Even if the concentrations of the potential determining ions are such as to give a good sur-

CHAPTER 6. STABILITY OF COLLOIDAL SUSPENSIONS

face charge, and therefore stability to the particles, we can induce aggregation acting on the indifferent ions, that is causing the double layer compression. This is shown in the figure above, where we see that as the concentration of the indifferent electrolyte increases, the energy barrier decreases and eventually becomes zero. At this point there is no opposition to aggregation, which becomes very fast and controlled by Brownian diffusion. The smallest electrolyte concentration leading to such a fast coagulation is called critical coagulation concentration. Typical values for three different colloids are reported in the table below:

Valency of counterions	Sol of As_2S_3 negatively charged		Sol of Au negatively charged		Sol of Fe(OH)_3 positively charged	
Monovalent	LiCl	58			NaCl	9.25
	NaCl	51	NaCl	24	$1/2\text{BaCl}_2$	9.65
	KNO_3	50	KNO_3	23	KNO_3	12
Divalent	MgCl_2	0.72	CaCl_2	0.41	K_2SO_4	0.205
	MgSO_4	0.81	BaCl_2	0.35	MgSO_4	0.22
	ZnCl_2	0.69			$\text{K}_2\text{Cr}_2\text{O}_7$	0.195
Trivalent	AlCl_3	0.093				
	$1/2\text{Al}_2(\text{SO}_4)_3$	0.096	$1/2\text{Al}_2(\text{SO}_4)_3$	0.009		
	$\text{Ce}(\text{NO}_3)_3$	0.080	$\text{Ce}(\text{NO}_3)_3$	0.003		

It is seen that the ccc values seem to be independent of the electrolyte type but strongly affected by the charge of the counterion. The value of the ccc can be computed from a suitable expression of $V_T(D)$ by imposing the two conditions for criticality:

$$V_T = 0 \quad \text{and} \quad \frac{dV_T}{dD} = 0 \quad (6.61)$$

Let us consider the case of flat surfaces with small overlapping ($\kappa D > 1$):

$$V_T = -\frac{A}{12\pi D^2} + \frac{64n^0 k T Z^2}{\kappa} \exp(-\kappa D) \quad (6.62)$$

By setting

$$V'_T = \frac{2A}{12\pi D^3} - \kappa \frac{64n^0 k T Z^2}{\kappa} \exp(-\kappa D) = 0 \quad (6.63)$$

and substituting in the equation $V_T = 0$, we get

$$\frac{2A}{12\pi D^3} - \kappa \frac{A}{12\pi D^2} = 0 \Rightarrow \frac{2}{D} - \kappa = 0 \Rightarrow \kappa D = 2 \quad (6.64)$$

CHAPTER 6. STABILITY OF COLLOIDAL SUSPENSIONS

Substituting in the relation $V_T = 0$, we get the critical κ :

$$\kappa^3 = \frac{(4 \cdot 12 \cdot 64)\pi n^0 k T Z^2 \exp(-2)}{A} \quad (6.65)$$

and recalling for symmetrical electrolytes $z = z_+ = z_-$

$$\kappa^2 = \frac{\sum n_i^0 z_i^2 e^2}{\varepsilon_w k T} = \frac{2 N_A z^2 e^2}{\varepsilon_w k T} C_s \quad (6.66)$$

where $C_s = n_i^0 / N_A$ is the molar electrolyte concentration, it follows

$$ccc[\text{mol/L}] = \frac{(384)^2 (4\pi)^2}{2 \exp(4)} \frac{\varepsilon_w^3 (kT)^5 Z^4}{N_A A^2 (ze)^6} \quad (6.67)$$

which at 25°C in water for relatively high potential so that $Z \approx 1$, reduces to

$$ccc = \frac{87 \cdot 10^{-40}}{z^6 A^2} \quad [\text{mol/L}] \quad (6.68)$$

This relation, although approximated, correctly predicts that the ccc value depends only on the charge of the electrolyte and in a rather strong way. This is known as the Schultz-Hardy rule. Its reliability is clearly demonstrated by the data shown in the table, where for the colloid As_2S_3 we have that the ccc values for mono, di and trivalent electrolytes can be scaled as follows:

$$50 : 0.7 : 0.09 \approx 1 : 0.014 : 0.0018 \quad (6.69)$$

which compare well with the equation prediction $1 : 2^{-6} : 3^{-6} = 1 : 0.016 : 0.0014$. It is confirmed that the type of electrolyte, if the valency is the same, plays a minor role.

Note

Since the stability behavior of colloids is dominated by the concentration of the counterion, we can restrict our attention to symmetric electrolytes. Then, $MgCl_2$ would behave like a 2:2 electrolyte in the presence of negatively charged surfaces, and like a 1:1 electrolyte in the presence of positively charged surfaces. This is confirmed by the ccc data reported in the previous table.

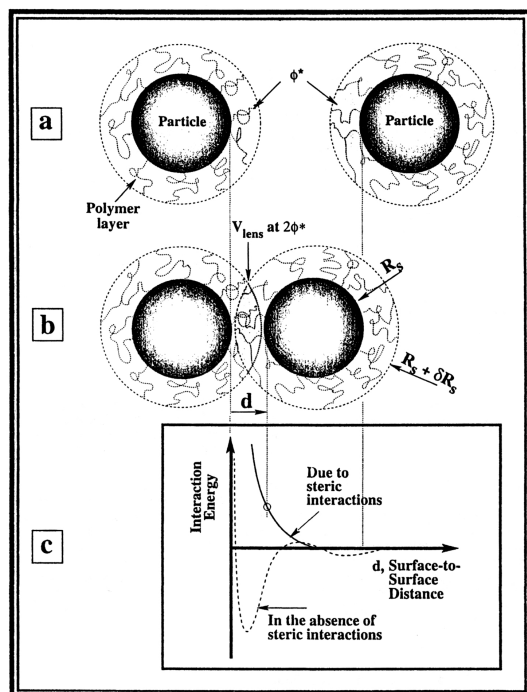
6.4 Steric Interactions

Steric interactions are the third important type of interactions between colloidal particles. Steric interactions are commonly used to stabilize particles when long term stability is required. The most common way to achieve steric stabilization is to graft some polymer on

CHAPTER 6. STABILITY OF COLLOIDAL SUSPENSIONS

the particle surface. The grafting can be achieved in various ways. The most common is to add polymer to a solution of particles and let it attach onto the particle surface. However, the amount of polymer to be added has to be accurately chosen, otherwise unwanted destabilization effects (instead of stabilization) such as depletion induced flocculation or bridging flocculation can arise. Recently, another method has been developed, which consists in growing a polymer brush directly from the particle surface.

The physical mechanism underlying steric stabilization is strongly related to the thermodynamic behavior of polymers in solutions. The simplest theory used to explain this mechanism is the Flory-Krigbaum theory. As two particles coated with a polymer layer approach each other, when the center-to-center distance is small enough there is an overlap between the polymer layers. This overlap generates a change in the free energy of the polymer layers. There are two contributions of the free energy of the solution: the first one is a mixing contribution, the second one is an elastic contribution to the free energy. For the first case, if the polymer volume fraction in an isolated layer is equal to ϕ , then the overlapping leads to a concentration of 2ϕ in the lens region, as depicted in the figure.



Polymer chains, if soluble in a solvent, occupy a large amount of volume, and their conformation is that of a random coil. If the degree of polymerization of the coil is equal to n , the

CHAPTER 6. STABILITY OF COLLOIDAL SUSPENSIONS

size of the coil scales as $R \sim n^{0.5}$. Therefore, if a chain is trying to occupy the same volume already occupied by another chain, there is usually an increase in the free energy of the system. The change in free energy resulting from the overlap of two sterically stabilized particles is equal to:

$$\Delta G = \Delta G_{\text{ov}} V_{\text{lens}} \quad (6.70)$$

The first term on the right hand side is the free energy change per unit volume, while the second term is the volume of the lens where the overlap occurs. The volume of the lens is a pure geometrical term, and is equal to:

$$V_{\text{lens}} = \frac{2\pi}{3} \left(\delta R_s - \frac{d}{2} \right)^2 \left(3R_s + 2 * \delta R_s + \frac{d}{2} \right) \quad (6.71)$$

where d is the surface to surface distance between the cores of the particles, δR_s is the outer radius of the shell and R_s is the radius of the core (see the previous Figure). The free energy of overlap per unit volume is equal to:

$$\Delta H_{\text{ov}} = 2kT \left(\frac{\overline{V_2}^2}{\overline{V_1} V_d^2} \right) \left(\frac{1}{2} - \chi \right) \quad (6.72)$$

where V_d is the volume occupied by a polymer coil, $\overline{V_1}$ is the solvent molar volume, and $\overline{V_2}$ is the polymer molar volume. It is important to note that the sign of the free energy of mixing per unit volume depends on the parameter χ . In units of kT , the parameter χ is a measure of the energy change between solvent-monomer interactions and solvent-solvent and monomer-monomer interactions. Mathematically this is expressed as follows:

$$\chi = \frac{z}{2kT} (2w_{12} - w_{11} - w_{22}) \quad (6.73)$$

where z is the coordination number of a monomer (or solvent) molecule, and w_{ij} is the energy of interaction between molecule i and molecule j . Here 1 are solvent molecules and 2 are monomer molecules. Therefore, depending on whether the monomer units like more solvent molecules rather than other monomer units, the χ parameter can become smaller or larger than 1/2. When $\chi > 1/2$ we are in the presence of a bad solvent, i.e., the monomer units prefer to stay close to each other because the polymer is not soluble under those conditions in that solvent. This means that the free energy given by equation (6.72) is negative. In this case, interpenetration of polymer shells is favored, and the polymer does not provide a good stabilization. If instead $\chi < 1/2$ the free energy given by equation (6.72) is positive,

CHAPTER 6. STABILITY OF COLLOIDAL SUSPENSIONS

and interpenetration is unfavorable. In that case, steric stabilization is effective. It is quite common that the quality of solvent can be changed for many polymers by simply playing with the temperature. In fact, the following temperature dependence of the χ parameter on the temperature is usually observed:

$$\frac{1}{2} - \chi = \psi \left(1 - \frac{\Theta}{T} \right) \quad (6.74)$$

where Θ is the famous Theta temperature. $T > \Theta$ implies a good solvent, while $T < \Theta$ implies a poor solvent. $T = \Theta$ is the critical solubility temperature for many solvents.

The second contribution to steric stabilization, arising when two polymer shells try to interpenetrate, is the elastic contribution. This mechanism underlying elastic stabilization is actually an entropic one, since polymer coils tend to assume in absence of any constraint a rather swollen configuration. By compressing a polymer, one limits their degrees of freedom and this reduction in configurational entropy generates a force that for small compressions can be approximated as obeying Hook's law, with an elastic constant equal to:

$$\Delta S_{ov} \propto k_H d, \text{ where } k_H = \frac{3kT}{nl^2} \quad (6.75)$$

where n is the degree of polymerization of a chain and l is approximately the length of a monomer unit. The contribution to the total free energy given by this mechanism is always positive, which means that compression of a polymer coil is always an unfavorable process.

When both contributions to steric stabilization are considered together, it turns out that in the case of a good solvent, steric interactions are always strongly repulsive. In the case of bad solvents, instead, attractive interactions dominate initially, but when the distance between the particle surface is further reduced, repulsion due to elastic compression eventually prevails.

Chapter 7

Kinetics and Structure of Colloidal Aggregates

7.1 Diffusion Limited Cluster Aggregation – DLCA

7.1.1 Aggregation Rate Constant – DLCA

In the case where no repulsive barrier exists between the particles, i.e., $V_T(D)$ is a monotonously increasing function with no maximum, the rate of particle aggregation is entirely controlled by Brownian motion. Let us compute the flow rate F of particles aggregating on a single reference particle. For this, we note that the flow rate, F of identical particles diffusing through a sphere centered around a given particle, is given by:

$$F = \left(4\pi r^2\right) D_{11} \frac{dN}{dr} \quad \text{with } N = N_0 \text{ at } r = \infty \text{ (bulk)} \quad (7.1)$$

where N is the particle concentration, r the sphere radius and D_{11} the mutual diffusion coefficient, which since both colliding particles undergo Brownian motion is equal to twice the self diffusion coefficient, i.e., $D_{11} = 2D$. At steady state, i.e., $F = \text{const.}$, the particle concentration profile is given by:

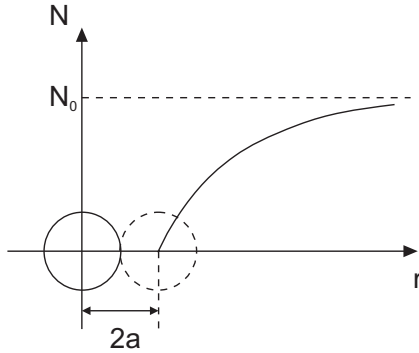
$$N = N_0 - \frac{F}{4\pi D_{11}} \frac{1}{r} \quad (7.2)$$

If we now assume that upon contact the second particle disappears (because of coagulation), that is $N = 0$ at $r = R_{11}$ where $R_{11} = 2a$ is the collision radius, we have:

$$F = 4\pi D_{11} R_{11} N_0 \quad (7.3)$$

which is the flow rate of particles aggregating on the single particle under consideration.

If we now consider only the beginning of the aggregation process, we can compute the rate of



decrease of the particle concentration in bulk due to the aggregation process, R_{agg}^0 as follows:

$$R_{\text{agg}}^0 = -\frac{1}{2}N_0F = -\frac{1}{2}4\pi DR_{11}N_0^2 = -\frac{1}{2}\beta_{11}N_0^2 \quad (7.4)$$

where the factor 1/2 is needed to count each event only once. In the above expression we have introduced the aggregation rate constant $\beta_{11} = 4\pi D_{11}R_{11}$, which plays the same role as the reaction rate constant in a second order kinetics.

In the case of two particles of equal size, a this reduces to:

$$\beta_{11} = 16\pi Da \quad (7.5)$$

and using the Stokes-Einstein equation to compute $D = kT/(6\pi\eta a)$, where η is the dynamic viscosity of the medium, we obtain:

$$\beta_{11} = \frac{8}{3} \frac{kT}{\eta} \quad (7.6)$$

which is size independent. In the case of two particles of different radius, R_i and R_j , we have:

$$\begin{aligned} \beta_{ij} &= 4\pi(D_i + D_j)(R_i + R_j) \\ &= \frac{2}{3} \frac{kT}{\eta} (R_i + R_j) \left(\frac{1}{R_i} + \frac{1}{R_j} \right) \end{aligned} \quad (7.7)$$

It is interesting to investigate the behavior of the aggregation rate constants for particles of different sizes.

a_i	a_j	$\frac{\beta_{ij}}{4\pi Da}$
\bar{a}	\bar{a}	4 $\Rightarrow \beta$ is size independent
\bar{a}	$\bar{a}/2$	$\left(\frac{1}{\bar{a}} + \frac{2}{\bar{a}}\right)\left(\bar{a} + \frac{\bar{a}}{2}\right) = 3 \cdot \frac{3}{2} = 4.5$
\bar{a}	$\bar{a}/4$	$\left(\frac{1}{\bar{a}} + \frac{4}{\bar{a}}\right)\left(\bar{a} + \frac{\bar{a}}{4}\right) = 5 \cdot \frac{5}{4} = 6.25$
\bar{a}	\bar{a}/n	$\left(\frac{1}{\bar{a}} + \frac{n}{\bar{a}}\right)\left(\bar{a} + \frac{\bar{a}}{n}\right) = (n+1)\frac{(n+1)^2}{n} = \frac{(n+1)^2}{n}$
		$\lim_{n \rightarrow \infty} \frac{(n+1)^2}{n} = \infty$

From the values in the table above it is seen that small/large collisions are more effective than small/small or large/large ones.

7.1.2 Cluster Mass Distribution – DLCA

In order to derive the Cluster Mass Distribution (CMD) of the aggregates containing k primary particles (or of mass k) we need to consider the following population balance equation, also referred to as *Smoluchowski equation*:

$$\frac{dN_k}{dt} = \frac{1}{2} \sum_{i=1}^{k-1} \beta_{i,k-i} N_i N_{k-i} - N_k \sum_{i=1}^{\infty} \beta_{ik} N_i \quad (7.8)$$

where N_k is the number concentration of aggregates of size k , and the first term on the r.h.s. represents all possible collisions leading to the formation of an aggregate of mass k , while the second is the rate of disappearance of the aggregates of mass k due to aggregation with aggregates of any mass. If we now assume that the aggregation rate constant is constant with size, i.e., $\beta_{ij} = \beta_{11}$ and we sum both sides of the equation above to compute the total aggregate concentration of any mass, that is

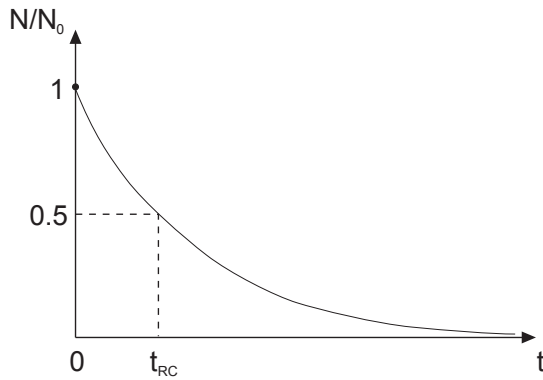
$$N = \sum_{k=1}^{\infty} N_k \quad (7.9)$$

we obtain:

$$\frac{dN}{dt} = \frac{1}{2} \beta_{11} N^2 - \beta_{11} N^2 = -\frac{1}{2} \beta_{11} N^2 \quad (7.10)$$

which integrated with the I.C.: $N(t = 0) = N_0$ leads to:

$$\frac{1}{N} = \frac{1}{N_0} + \frac{1}{2} \beta_{11} t \quad (7.11)$$



If we define the characteristic time of coagulation or of rapid coagulation, t_{RC} the time needed to half the initial value of aggregates we have:

$$t_{RC} = \frac{2}{\beta_{11}N_0} = \frac{1}{2\pi D_{11}R_{11}N_0} \quad (7.12)$$

which for particles of equal size reduces to:

$$t_{RC} = \frac{3\eta}{4kTN_0} \approx \frac{2 \times 10^{11}}{N_0} \quad [\text{s}] \quad (7.13)$$

where a water suspension at room temperature has been considered in the latter equation, with N_0 in cm^{-3} . As an example, for concentrated colloids of a few percent in solid volume, $N_0 = 2 \times 10^{14} \text{ cm}^{-3}$ the t_{RC} is in the range of milliseconds.

The CMD computed from the Smoluchowski equation is given by:

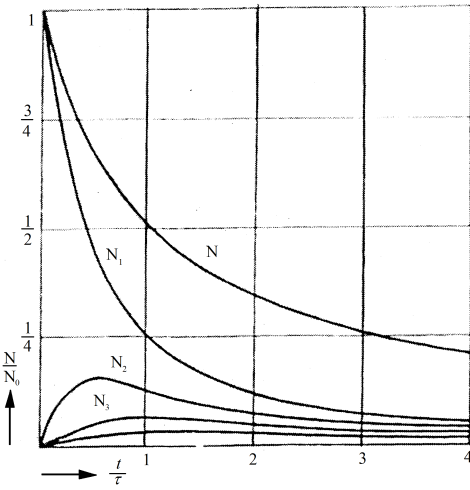
$$N_k = \frac{N_0 (t/\tau)^{k-1}}{(1 + t/\tau)^{k+1}} \quad (7.14)$$

where time has been made dimensionless using the rapid coagulation time, i.e., $\tau = t_{RC}$.

7.1.3 Role of Aggregate Morphology – DLCA

In order to solve the Smoluchowski equation in the general case where the aggregation rate constant is size dependent, that is:

$$\beta_{ij} = \frac{2}{3} \frac{kT}{\eta} (R_i + R_j) \left(\frac{1}{R_i} + \frac{1}{R_j} \right) \quad (7.15)$$



we need to correlate β_{ij} directly to the masses i and j of the two colloid clusters. Accordingly, we need to derive a relation between the size R_i of an aggregate and its mass i , that is to say something about the structure of the aggregate.

If we consider a solid sphere this relation is simple:

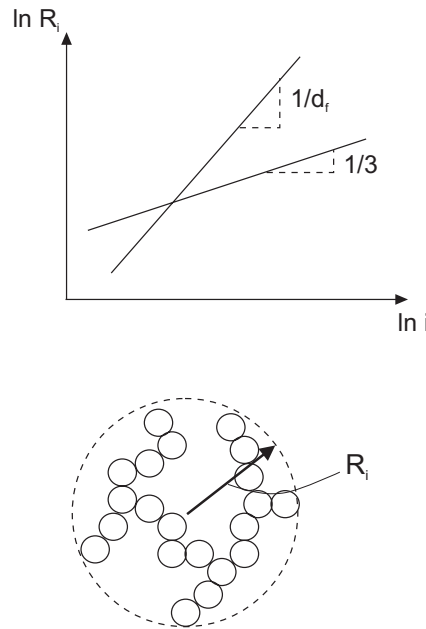
$$i = \rho \frac{4}{3} \pi R_i^3 \quad , \quad \rho = \text{density} \quad (7.16)$$

which reported on a log-log plot leads to a straight line with slope 1/3. This expression can be used in the case of coalescence, where smaller droplets (e.g. of a liquid) aggregate to form a larger drop. In this case, by substituting it in the above equation we get the following expression for the coalescence rate constant:

$$\beta_{ij} = \frac{2 k T}{3 \eta} (i^{1/3} + j^{1/3}) (i^{-1/3} + j^{-1/3}) \quad (7.17)$$

Using Monte Carlo simulations and light scattering measurements it has been shown that a similar straight line is obtained also for the polymer aggregates if we define as aggregate size, R_i the radius of the smallest sphere enveloping the entire cluster. This is the size that we have tacitly used above in computing the self diffusion coefficient of the fractal using Stokes-Einstein equation.

The difference with respect to the solid sphere is that in this case the slope of the straight line is much larger due to the many voids present in the fractal structure, and equal to $1/d_f$, where d_f is defined as the fractal dimension.



In typical applications d_f ranges from 1.5 to 3.0. If we now accept that our aggregates have a fractal structure, then we use the following scaling of their size with mass

$$R_i \propto i^{1/d_f} \quad (7.18)$$

which leads to the following expression for the aggregation rate constant:

$$\beta_{ij} = \frac{2}{3} \frac{kT}{\eta} (i^{1/d_f} + j^{1/d_f}) (i^{-1/d_f} + j^{-1/d_f}) \quad (7.19)$$

which can be used to solve numerically the Smoluchowski equation in diffusion limited conditions.

7.2 Reaction Limited Cluster Aggregation – RLCA

7.2.1 Aggregation Rate Constant – RLCA

In the case where a repulsive energy barrier is present between particles, i.e., $V_T(D)$ exhibits a maximum value, then the aggregation process becomes slower than the diffusion limited described above and becomes controlled by the presence of the interparticle potential. This is often referred to as reaction limited cluster aggregation, RLCA. In this case, in computing the particle flow rate, F entering a sphere of radius, r centered on a given particle, we have

CHAPTER 7. KINETICS AND STRUCTURE OF COLLOIDAL AGGREGATES

to consider not only the particle concentration gradient, i.e., brownian diffusion, but also the potential gradient. The particules are diffusing toward each other while interacting in the potential field $V_T(r)$ whose gradient is producing a force:

$$F_T = -\frac{dV_T}{dr} \quad (7.20)$$

which is contrasted by the friction force given by Stokes law, $F_f = Bu$, where $B = 6\pi\eta a$ represents the friction coefficient for a sphere of radius, a in a medium with dynamic viscosity, η . The two forces equilibrate each other once the particle reaches the relative terminal velocity, u_d so that $F_T = F_f$. This implies a convective flux of particles given by:

$$J_c = u_d N = -\frac{N}{B} \frac{dV_T}{dr} \quad (7.21)$$

which superimposes to the diffusion flux:

$$J_d = -(D_{11}) \frac{dN}{dr} \quad (7.22)$$

where D_{11} is the mutual diffusion coefficient of the particles. The flow rate of particles aggregating on one single particle, F , which at steady state conditions is constant, is given by:

$$F = -(4\pi r^2)(J_c + J_d) = (4\pi r^2) D_{11} \left(\frac{dN}{dr} + \frac{N}{kT} \frac{dV_T}{dr} \right) \quad (7.23)$$

where using the Stokes-Einstein equation the friction factor can be represented in terms of the diffusion coefficient by $B = kT/D_{11}$. Using the B.C.: $V_T = 0$, $N = N_0$ at $r \rightarrow \infty$, and $dN/dr + \frac{N}{kT} dV_T/dr = \exp(-\frac{V_T}{kT}) d(\exp(\frac{V_T}{kT}))/dr$, this equation can be integrated leading to:

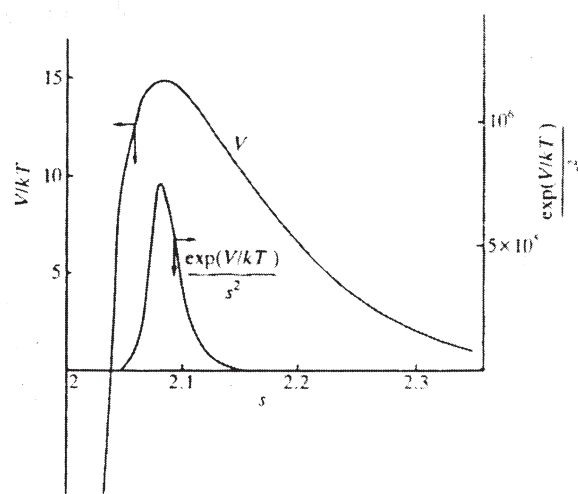
$$N = N_0 \exp\left(-\frac{V_T}{kT}\right) + \frac{F \exp(-V_T/kT)}{4\pi D_{11}} \int_{\infty}^r \exp\left(\frac{V_T}{kT}\right) \frac{dr}{r^2} \quad (7.24)$$

from which, considering $N = 0$ at $r = 2a$ and $D_{11}=2D$, we compute:

$$F = -\frac{8\pi DN_0}{\int_{2a}^{\infty} \exp(V_T/kT) dr / r^2} \quad (7.25)$$

Note that for $V_T = 0$ we obtain $F = 8\pi DN_0(2a)$, which is the same value computed earlier for diffusion limited aggregation. Considering the definition of aggregation rate constant, $\beta = F/N$, we can conclude that $F^{DLCA}/F = \beta^{DLCA}/\beta$. This is a very important parameter in colloidal science and is usually referred to as the Fuchs or stability ratio, W defined as:

$$W = \frac{\beta^{DLCA}}{\beta} = 2a \int_{2a}^{\infty} \exp\left(\frac{V_T}{kT}\right) \frac{dr}{r^2} \quad (7.26)$$



which gives the value of the ratio between the rates of rapid (diffusion limited) and slow (reaction limited) aggregation. By looking at the function $(a/r)^2 \exp[V_T/(kT)]$ shown in the figure above, it is apparent that the value of its integral can be related to the value of only the maximum value of V_T , i.e., $V_{T,\max}$. In particular, the following approximate equation for W has been derived:

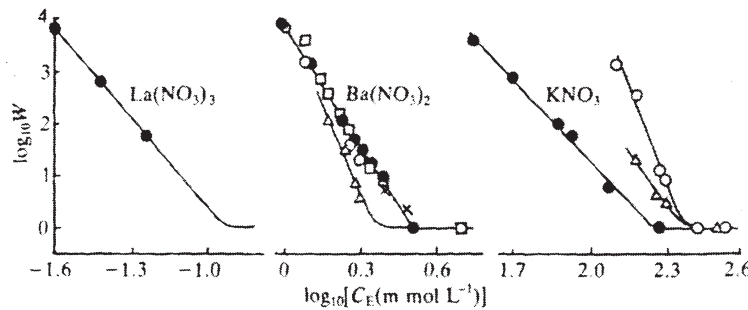
$$W \approx \frac{1}{2\kappa a} \exp\left(\frac{V_{T,\max}}{kT}\right) \quad (7.27)$$

where $1/\kappa$ is the thickness of the diffusive layer as defined in section 6.2.2. Using this relation we can compute the W values corresponding to typical values of $V_{T,\max}$ in applications. From this we can compute the corresponding half coagulation time $t_{1/2} = 2/(\beta_{11}N_0)$ following the same procedure used in section 7.1.2 to compute $t_{RC} = 2/(\beta_{11}^{DLCA}N_0)$. Considering again the case where $N_0 = 2 \cdot 10^{14} \text{ cm}^{-3}$ we obtain the results reported in the following table:

$V_{T,\max}$	≤ 0	$15kT$	$25kT$
W	1	10^5	10^9
$t_{1/2} [\text{s}]$	$t_{RC} = 10^{-3}$	10^2	10^6

These clearly indicate the meaning of kinetic stabilization, since with a modest energy barrier the coagulation process can be delayed from milliseconds to days or months. Note that the value of W tends to be very sensitive to even small changes of the surface charge or potential. In particular, in these conditions we have that a ten-fold variation of W is obtained with an about 15% change in $V_{T,\max}$ and a 7% change in the surface potential, ψ_0 . This makes it unfeasible to compute W from measurements of ψ_0 , while it is recommended to measure it

from direct measurements of the kinetics of particle aggregation, i.e., β_{11} . It can be shown that the relation above for W leads to the plots shown below in the plane $\log W - \log c_E$, where c_E is the concentration of an electrolyte. The region where $W > 1$ has a negative slope, which depends upon the valency of the electrolyte, and is well confirmed by the experimental value. This loss of stability is due to the double layer compression effect, which appears in the above equation through the effect of the ionic strength on the Debye-Hückel parameter, κ .



The second region corresponds to diffusion control, which is unaffected by the presence of an electrolyte, i.e., $W = 1$. The intersection of the two straight lines indicates the ccc, where the energy barrier vanishes.

7.2.2 Role of Cluster Morphology – RLCA

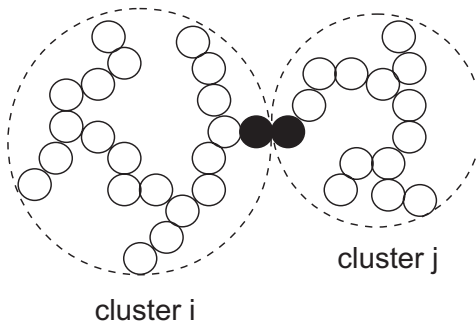
We have seen that in the case of primary particles under RLCA conditions the aggregation rate constant is given by:

$$\beta_{11} = \frac{\beta_{11}^{\text{DLCA}}}{W} \quad (7.28)$$

We now need to extend this to the aggregation of two clusters of size i and j , respectively. One way to consider this problem is to assume that the aggregation of the two clusters occurs through the interaction between the two primary particles, on each aggregate, which first come into contact. This has two relevant consequences:

1. The aggregate-aggregate interaction can be approximated with the interaction between the two colloidizing primary particles, which is described by the stability ratio W . The interactions with the other particles can be assumed to be too short range to be relevant.

2. The rate of aggregation depends upon the probability of collision between the primary particles on the cluster surface, which means the probability of having a primary particle on the external surface of a cluster.



For a given cluster k , the change in the number of primary particles in the cluster with its size, a_k , is given by:

$$k = \left(\frac{a_k}{a}\right)^{d_f} \Rightarrow \frac{dk}{da_k} = \frac{d_f}{a} \left(\frac{a_k}{a}\right)^{d_f-1} = \frac{d_f}{a} k^{(d_f-1)/d_f} \quad (7.29)$$

If we multiply this by the primary particle radius, a we get the number of primary particles added on the last layer of the aggregate:

$$a \frac{dk}{da_k} = d_f k^{(d_f-1)/d_f} \quad (7.30)$$

This means that the aggregation rate constant should be augmented by a factor $k^{(d_f-1)/d_f}$ when we consider the probability of collision of the primary particles instead of that of collision of the clusters. With this result we can derive the final expression for the aggregation rate constant in RLCA conditions:

$$\beta_{ij} = \frac{\beta_{ij}^{\text{DLCA}}}{W} (ij)^\lambda \quad (7.31)$$

where $\lambda = (d_f - 1) / d_f$, which for $d_f \approx 2$ leads to $\lambda \approx 0.5$, which has received some experimental validation.

Upon collision the aggregates formed in RLCA conditions have time to probe many possible configurations for an aggregation event. Due to this, the resulting aggregates are denser than their counterparts in DLCA, and can also penetrate deeper into each other without immediately aggregating. This results in aggregates which are generally denser with fractal dimensions of about 2.1.

7.2.3 Cluster Mass Distribution – RLCA

In RLCA detailed calculations of the CMD using equation 7.8 with the aggregation rate constant shown in equation 7.31 can only be obtained from numerical solutions to the PBE. However, for many aggregation problems in non-sheared colloidal dispersions it has been found that the resulting CMD exhibits some general features. Therefore it is possible to develop scaling solutions of the PBE, which are often sufficient for approximate purposes. A general form of the solution for a wide range of aggregation rate constants is given by

$$N_k(t) = Ak^{-\tau} \exp(-k/k_c), \quad (7.32)$$

where A is a normalization constant determined from the conservation of total mass in the system and is given by

$$A = \frac{N_0 k_c^{\tau-2}}{\Gamma(2-\tau)} \quad (7.33)$$

where $\Gamma(x)$ is the gamma function. k_c is the time dependent cutoff-mass of the distribution which grows with time and determines the kinetics. In RLCA, this growth is exponential, as $k_c(t) = p \exp(t/t_0)$, where t_0 is a sample dependent time constant. τ is a power-law exponent of the CMD describing the shape of the CMD. In RLCA $\tau = 1.5$ has been found to be a reasonable value.

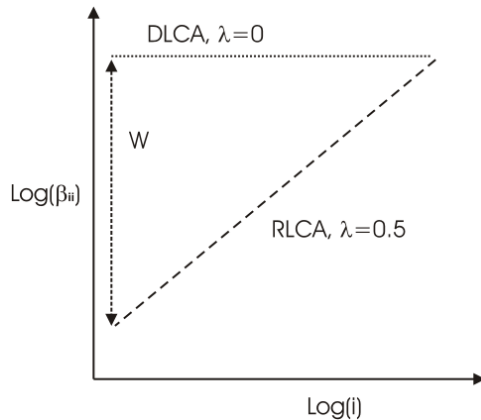
7.3 Comparison of Aggregation Regimes – DLCA vs. RLCA

7.3.1 Aggregation Rate Constant – DLCA vs. RLCA

We now compare the aggregation rate constants of the two aggregation regimes, DLCA and RLCA. The general kernel valid for the two regimes can be written as

$$\begin{aligned} \beta_{ij} &= \beta_{11}^{DLCA} W^{-1} B_{ij} P_{ij} \quad \text{with} \\ \beta_{11}^{DLCA} &= 8kT/(3\eta) \\ W &= \frac{\beta_{11}^{DLCA}}{\beta_{11}} \\ B_{ij} &= \frac{1}{4} (i^{-1/d_f} + j^{-1/d_f}) (i^{1/d_f} + j^{1/d_f}) \\ P_{ij} &= (ij)^\lambda, \text{ with } \lambda = 0 \text{ in DLCA and } \lambda \sim 0.5 \text{ in RLCA,} \end{aligned} \quad (7.34)$$

Most important for the aggregation kinetics is the aggregation rate of equal sized aggregates β_{ii} as a function of aggregate mass i . Therefore the parameter λ is extremely important for the kinetics as it dominates this function, as is displayed below.



In DLCA, as discussed before, $W \approx 1$ and $\lambda = 0$. On the other hand, in RLCA W is large and $\lambda \approx 0.5$, therefore exhibiting a strong mass dependence of β_{ij} . In summary, in DLCA the aggregation of big with small aggregates is favored and the aggregation rate of equal sized aggregates is independent of the aggregate mass, whereas in RLCA big clusters preferably aggregate with big ones such that the aggregation rate of equal sized aggregates strongly increases with the aggregate mass. This is reflected by the aggregation rate constant values β_{ij} , shown in figure 7.1 as a function of the aggregate masses i and j in figure 7.1 for the aggregation regimes DLCA and RLCA.

7.3.2 Cluster Mass Distribution – DLCA vs. RLCA

The mathematical formulation of the cluster mass distributions in DLCA and RLCA has been presented above. The equations were for DLCA

$$N_k = \frac{N_0 (t/\tau)^{k-1}}{(1 + t/\tau)^{k+1}} \quad (7.35)$$

and for RLCA

$$N_k(t) = \frac{N_0 k_c^{\tau-2}}{\Gamma(2-\tau)} k^{-\tau} \exp(-k/k_c), \quad (7.36)$$

The last equation can be shown to give identical results to the CMD for DLCA (equation 7.35) if $\tau = 0$ is chosen. The different shapes of CMD that are obtained during the aggregation

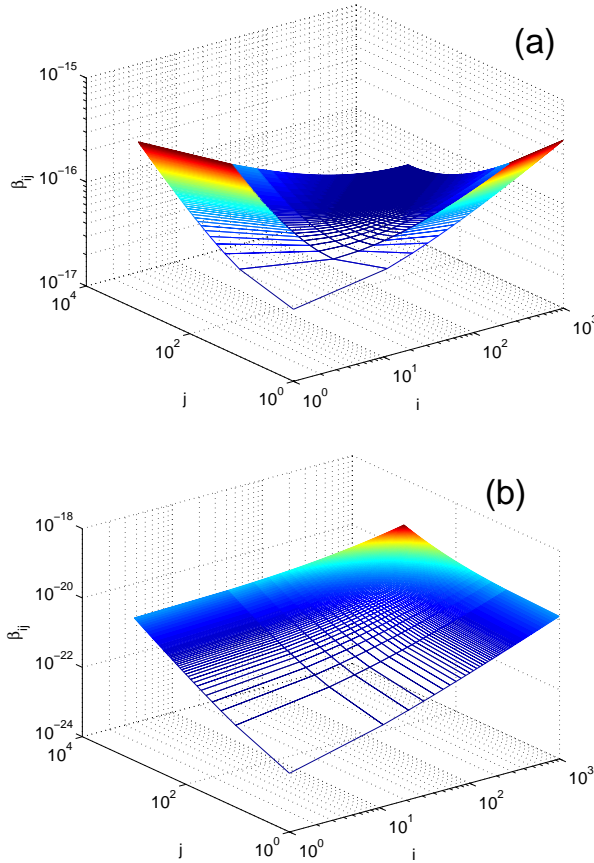


Figure 7.1: (a) DLCA; (b) RLCA

process are plotted in figure 7.2. There we see that the distribution for DLCA is flat when computed with the constant kernel (equation 7.35) or the scaling solution with $\tau = 0$. When using the full DLCA kernel, a bell-shaped CMD is obtained. It is seen that as time is passing by the CMD moves towards larger sizes and its area decreases, as a consequence of the increase in size and decrease in number of the aggregates. After a short transient time, the CMD exhibits the typical self-preserving behaviour due to the fact that the rear of the distribution moves at the same speed as the front.

Typical RLCA distributions are shown in figure 7.3 where we compare a scaling solution with $\tau = 1.5$ and the full numerical solution using the RLCA kernel in equation 7.34. Obviously, in this case the scaling solution is a very powerful tool to obtain good estimates of the CMD without going through the procedure of numerically solving the PBE. In the case of RLCA,

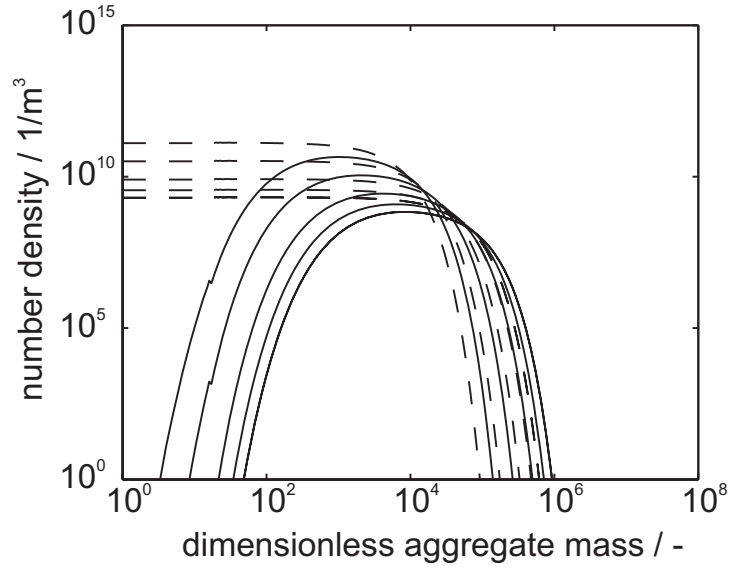


Figure 7.2: The CMDs computed with the DLCA kernel. Constant, not size dependent kernel (dashed line) and full size dependent "fractal" kernel (solid line).

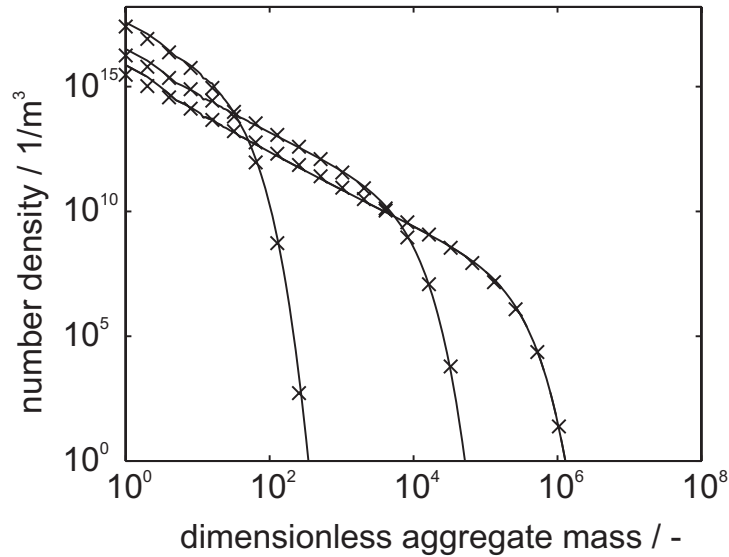


Figure 7.3: Cluster mass distribution (CMD) computed using the aggregation kernel is Eq. (7.34) for RLCA with $W = 2.8 \times 10^4$ (continuous lines). The scaling solution for RLCA in Eq. (7.36) with $\tau = 1.5$ is also plotted for comparison (\times).

the time evolution of the CMD exhibits a fundamental difference with respect to DLCA. Since large-large aggregations dominate in this case, the CMD becomes wider in time, and actually

primary particles remain present in the system up to large aggregation times. The CMD does not exhibit the typical bell shape which causes often problems in the technology.

7.3.3 Aggregate Morphology – DLCA vs. RLCA

We have seen that the kernel and the CMD in the two regimes are rather different. This is also apparent in the aggregate structure that often can be described by the aforementioned fractal dimension d_f . There are several ways to measure the fractal dimension, either by sedimentation experiments, light scattering or image analysis. Such direct images can be obtained, for example, by transmission electron microscopy (TEM) and one example is shown in the picture below. Aggregates of different materials and from computer simulations (the lowest set) are

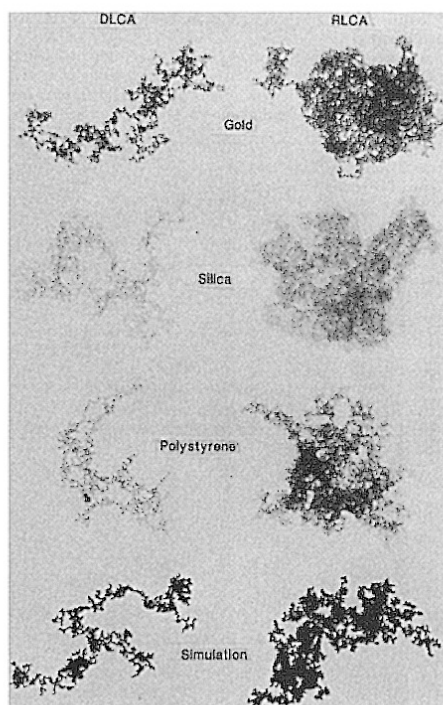


Figure 7.4: left panel: DLCA; right panel: RLCA

shown in figure 7.4 for the two regimes, DLCA and RLCA. Obviously, the clusters for DLCA are much more tenuous and open than the ones formed in RLCA.

In summary, the fractal dimensions for each of the regimes are

Fractal relation: $R \sim i^{1/d_f}$

Regime	Fractal dimension d_f
DLCA	1.6 – 1.9
RLCA	2.0 – 2.2

7.3.4 Comparison to Experimental Data

As has been shown in the TEM images in the previous section the agreement between experimental images and those generated from computer models are very satisfactory and support the fractal concept. However, direct comparison between the CMD computed with the Smoluchowski or PBE equations and experimental data is not straightforward, because direct experimental measurements of the CMD are not or hardly possible. Therefore light scattering techniques are often used, where averages (certain moments of the distribution) are measured. These moments can, with the proper theory, be computed from the CMD and compared to experimental data. This allows to validate the aggregation models presented in this chapter. In figure 7.5 we show two examples of such validation, one for each of the two aggregation regimes. The lines are model calculations and points are the experiments data.

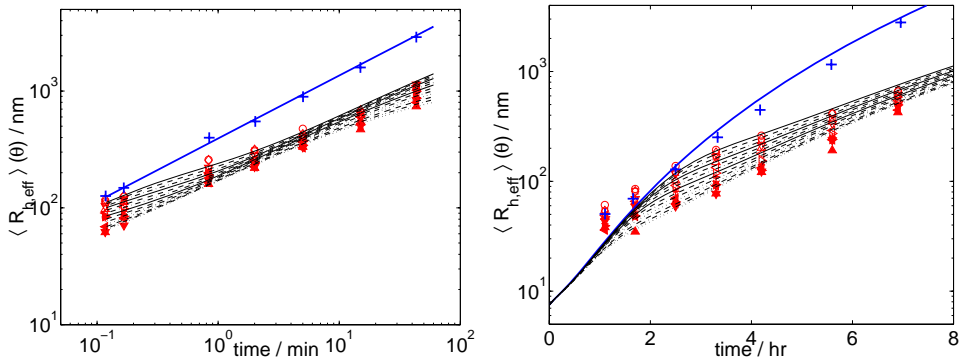


Figure 7.5: Left panel: DLCA regime, comparing the real time evolution of the experimental light scattering data and the model calculations. Right panel: RLCA regime, comparing experimental data and model calculations.

A further experimental support to the models discussed above can be obtained by making

the PBE (Eq. 7.8) dimensionless using the following definition for the dimensionless concentration of the clusters of mass k and the dimensionless time:

$$\phi_k = \frac{N_k}{N_0} \quad (7.37)$$

$$\tau = N_0 \beta_{11}^{DLCA} \frac{t}{W} \quad (7.38)$$

where N_0 is the initial number of primary particles, W the Fuchs stability ratio and β_{11}^{DLCA} the primary particle aggregation rate constant in DLCA conditions as defined by equation 7.34. Thus, the following dimensionless PBE is obtained from equations 7.8 and 7.34.

$$\frac{d\phi_k}{d\tau} = \frac{1}{2} \sum_{i=1}^{k-1} B_{i,k-i} P_{i,k-i} \phi_i \phi_{k-i} - \phi_k \sum_{i=1}^{\infty} B_{i,k} P_{i,k} \phi_i \quad (7.39)$$

with initial conditions: $\phi_0 = 1$, $\phi_k = 0$ for $k \geq 1$.

It is remarkable that in this form, the PBEs depend only on two parameters: the fractal dimension d_f and the parameter λ in equation 7.34. Since these two parameters do not depend on many physical parameters such as ionic strength or primary particle concentration, the above equation can be regarded as a master equation describing some kind of universal behavior of aggregating systems under DLCA and RLCA conditions. Some experimental verification of these conclusions are reported in figure 7.6.

7.4 Cluster Coalescence

Let us consider the case where the particles constituting a cluster can coalesce by polymer interdiffusion, as it is the case for polymers close or above their glass transition temperature.

Figure 7.7 shows cryo-SEM images of elastomer clusters for two limiting cases. If the coalescence process is fast with respect to aggregation, i.e., the characteristic time for particle fusion is much smaller than the characteristic aggregation time, $\tau_{\text{fus}} \ll \tau_{\text{agg}}$ (e.g., with $\tau_{\text{fus}} \propto \eta R_1 / \gamma$, and $\tau_{\text{agg}} \propto 1 / [\beta_{1,1} N_0]$), the newly formed clusters relax to spherical geometry (Figure 7.7a) before being involved in the next aggregation event. On the other hand, if the coalescence process is very slow compared to aggregation, i.e., $\tau_{\text{fus}} \gg \tau_{\text{agg}}$, coalescence is suppressed and ramified, fractal clusters are prevailing (Figure 7.7b).

The influence of the cluster structure on the aggregation kinetics can be well demonstrated under DLCA conditions where the aggregation kernel, β_{ij}^{DLCA} , has only one free parameter,

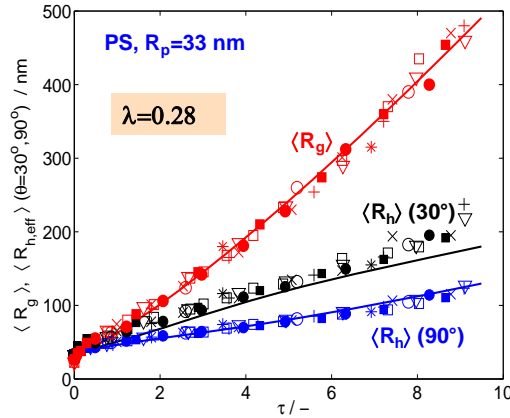


Figure 7.6: Average gyration and hydrodynamic radii, $\langle R_g \rangle$ and $\langle R_h \rangle$, as a function of the dimensionless time, τ , computed from PBE simulations (curves), compared with experimental data, where different symbols indicate data from different salt concentrations and particle volume fractions.

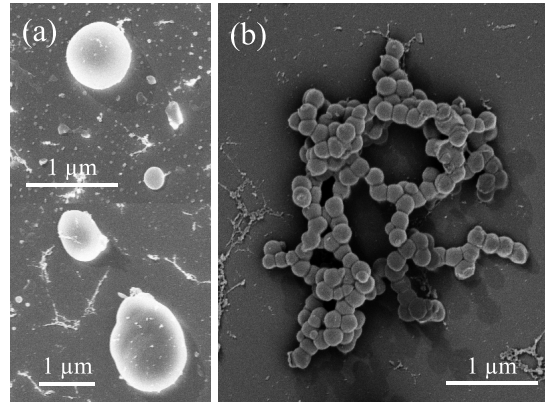


Figure 7.7: Cryo-SEM images of the clusters formed by (a) soft and (b) rigid elastomer latex particles in DLCA at 25 °C.

the fractal dimension d_f . In particular, we can use the result (not shown) that in DLCA the average particle size or radius scales with time as:

$$\langle R \rangle \propto t^{1/d_f} \quad (7.40)$$

Accordingly, when we measure for example the average hydrodynamic radius $\langle R_h \rangle$ for an aggregating system, we can use the scaling at large times to extract information about the

cluster structure. As shown in Figure 7.8, for fully coalescing clusters the time evolution of $\langle R_h \rangle$ follows $\langle R_h \rangle \propto t^{1/3}$, which is clear from the spherical shape, i.e., $d_f = 3.0$. On the other hand, for the cluster growth of rigid particles the scaling is: $\langle R_h \rangle \propto t^{1/1.7}$, i.e., $d_f = 1.7$, as typical for fractal clusters grown in DLCA. It is worth noting that the dimensionless scaling of experimental data obtained under different conditions (e.g., temperature, particle concentration, or coagulant type) leads to unique master-curves characterized in their scaling by the d_f value, as can be taken from Figure 7.8.

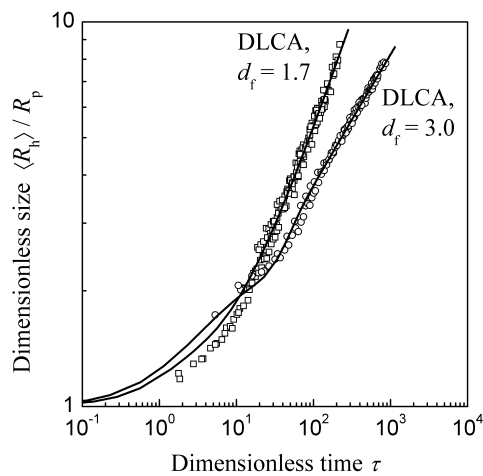


Figure 7.8: Dimensionless scaling of the average hydrodynamic radius $\langle R_h \rangle$ with time under DLCA conditions. Circles are experimental data of coalescing clusters where $d_f = 3.0$. Squares are experimental data of fractal clusters lattices with $d_f = 1.7$. Solid curves are the corresponding simulation results.

Cluster coalescence and colloidal interaction. In contrast to DLCA, where particle repulsion is completely screened, under RLCA conditions the fate of surface charges during coalescence is important for the aggregation kinetics. To account for partial repulsion of spherical clusters of different sizes i and j , one can use the following PBE kernel:

$$\beta_{i,j} = \frac{2kT}{3\eta} \frac{(i^{1/3} + j^{1/3})(i^{-1/3} + j^{-1/3})}{W_{i,j}} \quad (7.41)$$

where the fractal dimension is fixed because of the spherical cluster shape, i.e., $d_f = 3.0$. In addition, the colloidal stability is not anymore determined by the interaction of primary particles as in the case of non coalescing aggregates. The reason is that upon the coalescence

process on one hand the total polymer surface decreases, thus leading to more stable dispersions, but on the other hand some of the surface charges may be entrapped inside the newly formed particles thus having a destabilizing effect.

Using a simple particle sintering model, we can envision the coalescence process in Figure 7.9 as given by a first deformation of the two attached spheres at the point of contact (a), leading to a circular region (b) where a surface area of $2\pi y^2$ is lost. All surface charges located in this region are entrapped. Next, the process proceeds to the final spherical geometry (c) where charge redistribution without further entrapment takes place.

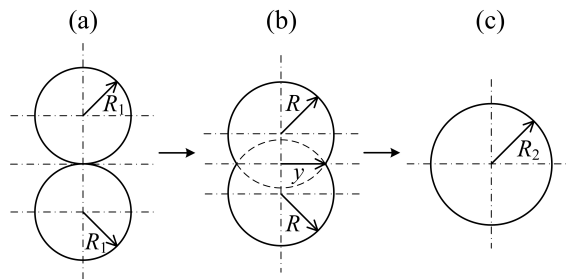


Figure 7.9: Schematic shape evolution of a coalescing doublet.

In this model we can take the neck radius, y to characterize the extent of particle fusion and then the number of charged sites left at the end of the coalescence process. For example, in the case of two coalescing primary particles with radius R_1 , the neck radius y is constrained between zero and $R_2 (= 2^{1/3}R_1)$. Thus, for a given y value, the balance of initial, lost, and remaining surface charges returns the value of the surface charge density $\sigma_{s,2}$ after full doublet coalescence. This calculation can be easily extended to the coalescence of any equal sized clusters with radius $R_{i/2}$ and final radius R_i ($i \geq 2$). The obtained results are shown in Figure 7.10a (open circles) in terms of the relative surface charge density, $\sigma_{s,i}/\sigma_{s,1}$, as a function of the resulting cluster mass i . The solid line represents a power-law fit to these data, i.e., $\sigma_{s,i}/\sigma_{s,1} = i^n$, where n is an adjustable parameter that depends on the y value. The only possibility to estimate y and n is by fitting experimental coalescence data such as those shown in Figure 7.10b. With the obtained $y = 1.005R_{i/2}$, it is seen from Figure 7.10a that as clusters increase in size i their surface charge density $\sigma_{s,i}$ decreases due to the charge entrapment during coalescence. However, we find that at least in this case $W_{i,j}$ is nevertheless increasing with cluster size (due to the increase of the particle size), which causes the slow down in the $\langle R_h \rangle$ and $\langle R_g \rangle$ time evolutions, shown in Figure 7.10b, if we compare the RLCA to the DLCA data

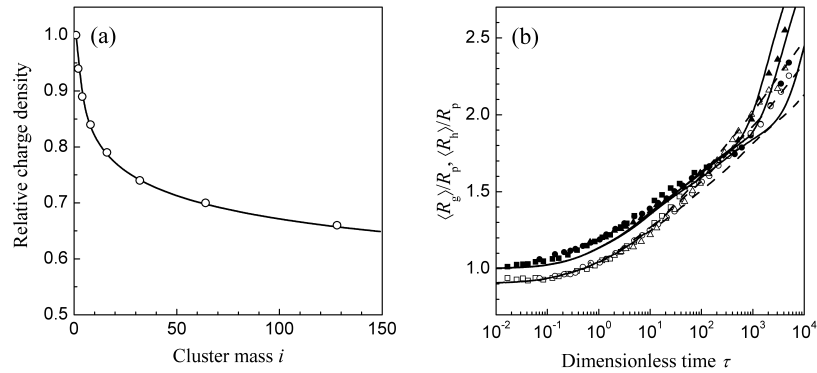


Figure 7.10: (a) Relative surface charge density of clusters of mass i , $\sigma_{s,i}/\sigma_{s,1}$. Discrete values (circles) are calculated assuming entrapment of fixed charges from the area $2\pi y^2$ with $y = 1.005R_{i/2}$ ($i = 2, 4, 8, 16$, etc.). The solid line is a power-law fit, $\sigma_{s,i}/\sigma_{s,1} = i^{-0.0865}$, to predict $\sigma_{s,i}$ for clusters of arbitrary size.
 (b) Dimensionless time evolutions of average hydrodynamic and gyration radii, $\langle R_h \rangle$ (filled symbols) and $\langle R_g \rangle$ (open symbols), in RLCA for three different coagulant concentrations (ionic strength). Solid and broken curves are results of the respective PBE simulations.

(see Figure 7.8 for comparison). A further feature of the RLCA–coalescence process as shown in figure 7.10b is that not all the experimental data collapse onto master-curves for $\langle R_h \rangle$ and $\langle R_g \rangle$ as we discussed in section 7.3.4 for non-coalescing systems. This is, despite having equal charge loss, i.e., using the same value of y , because of the different evolution of $W_{i,j}$ with ionic strength for the three different coagulant concentrations used in the experiments.

Let us compare the case of coalescing elastomer clusters having fixed surface charges discussed above to the case of mobile charges. This is for example the case of ionic surfactants that are typically only physically adsorbed on the particle surface. In this case the charged groups are squeezed out from the neck region during particle fusion and they relocate according to their adsorption equilibrium. Thus, assuming that no charge is entrapped, the surface charge density σ_s becomes a function of the available colloidal surface S , i.e., $\sigma_s(S)$. If the adsorption equilibrium of the surfactant is known, one can compute σ_s from the actual colloidal surface given by the CMD at time t . For the experimental system considered in Figure 7.11a, it is shown that the charge density increases as the particle surface decreases during aggregation and cluster coalescence. Accordingly, the colloidal interactions, change in time and in particular the stability ratio W_{ij} increases during aggregation. Figure 7.11b shows the time evolution

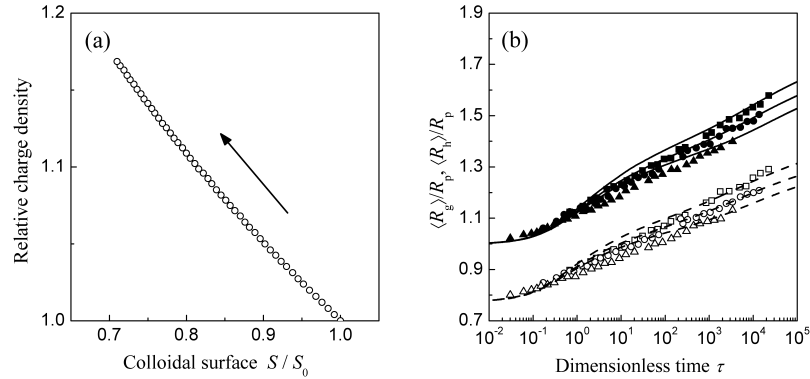


Figure 7.11: (a) Relative surface charge density $\sigma_s/\sigma_{s,0}$ as a function of the available colloidal surface, S/S_0 .
 (b) Dimensionless time evolutions of average hydrodynamic and gyration radii, $\langle R_h \rangle$ (filled symbols) and $\langle R_g \rangle$ (open symbols), in RLCA for three different coagulant concentrations (ionic strengths). Solid and broken curves are results of the respective PBE simulations.

of the average cluster sizes of three colloidal systems under these conditions. It is seen that the process is much slower, particularly when compared to the case of fixed charges shown in figure 7.10. Finally note that again the experimental data do not collapse onto master-curves, manifesting that RLCA under coalescence conditions is a non-universal process. In the case of the mobile surfactant charges, their relocation depends on the dissociation state of the ionic groups and therefore on the ionic strength of the solution, which is different for the three coagulant concentrations employed in figure 7.11.

7.5 Solid Suspensions under Shear

7.5.1 Shear induced Aggregation

In all previous chapters we considered the aggregation kinetics of colloidal suspensions in stagnant conditions, where particle collisions are driven by Brownian motions, i.e., Brownian-induced aggregation. This is relevant in many applications such as the estimation of the shelf stability of a solid dispersion. However, in most industrial processes suspensions are subject to stirring and then the aggregation process is driven by the velocity gradient induced in the suspension by the stirrer. This is referred to as shear-induced aggregation and it is discussed

in the following.

Purely shear-induced aggregation kinetics

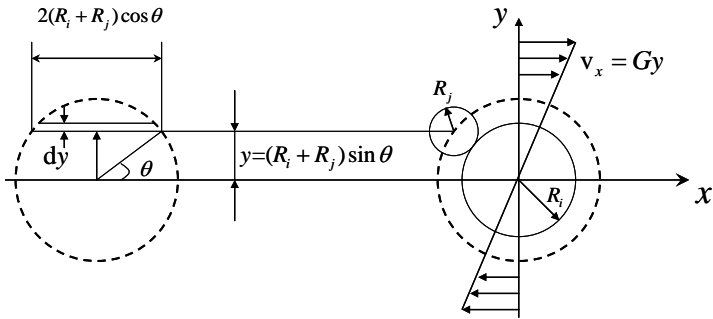


Figure 7.12: Schematic of the geometry of the problem for purely shear-induced aggregation.

We consider the stationary test particle, of radius R_i , located at the origin of the Cartesian frame, and a particle of radius R_j moving toward the test particle along the streamline of the shear flow, x . From the geometry of the problem, schematically depicted in figure 7.13 below, it is evident that the two particles can collide and aggregate only if the relative distance between the two particles centers is $y \leq (R_i + R_j)$ which implies that the y -axis coordinate of the center of the second particle must be $y \leq (R_i + R_j) \sin \theta$. The velocity of the second particle along the x direction be denoted by $v_x = Gy$, where G is the constant shear-rate. If we denote by n_j the number of particles j per unit volume, the number of particles j that enter the element of collision surface in the upper-left quadrant per unit time is given by:

$$2[(R_i + R_j) \cos \theta] G n_j dy \quad (7.42)$$

Given the symmetry of the problem, an equal number of collisions arises in the lower-right quadrant. Introducing a factor two and the number concentration of test particles, n_i and integrating over the spatial coordinate, gives the total number of collisions with the test particle per unit time and per unit volume:

$$4 \int_0^{R_i + R_j} [(R_i + R_j) \cos \theta] G n_i n_j dy \quad (7.43)$$

Substituting for y and changing the integration coordinate to θ leads to :

$$4n_i n_j (R_i + R_j)^3 G \int_0^{\pi/2} \cos^2 \theta \sin \theta d\theta \quad (7.44)$$

CHAPTER 7. KINETICS AND STRUCTURE OF COLLOIDAL AGGREGATES

from which the collision frequency per unit volume follows as:

$$\beta_{11} = \frac{32R^3G}{3} \quad (7.45)$$

This result, which was derived for the first time by M. von Smoluchowski in the eventful year 1917, shows that the rate of shear-induced aggregation is proportional to the shear rate and to third power of the sum of the particle radii. This strong dependence on the particle size is what renders shear aggregation faster than Brownian aggregation for sufficiently large particles.

The above β_{11} expression is valid under laminar conditions, seldom encountered in industrial units that typically operate under turbulent conditions. In the presence of turbulence, such dependency is still valid, provided that G is replaced by an average shear rate that can be calculated from the average energy dissipation rate of the turbulent flow, ϵ . This approximation is valid in the case where the aggregates are smaller than the Kolmogorof vortices, within which the laminar flow prevails with shear equal to $G = (\epsilon/\nu)^{0.5}$, where ν is the kinematic viscosity of the disperse medium.

Generalization to DLVO-interacting Brownian particles in shear flow

The Smoluchowski result for purely shear-induced aggregation kinetics is valid under the restrictive hypotheses that the particles are non-Brownian and non-interacting. The latter hypothesis means that the particles are treated as hard spheres which stick upon collision. The shear-induced aggregation kinetics of Brownian particles which do interact (typically with a superposition of van der Waals attraction and electric double layer repulsion) is a more complicated problem. The interplay between shear and interactions in this case gives rise to an interesting phenomenology: a colloidal suspension which is completely stable under stagnant conditions (owing to charge-stabilization) can be made to aggregate under the imposition of shear flow, with the result that the rheological properties of the suspension may change dramatically. A typical situation is depicted in the Figure below, where, after a lag-time or induction period within which it remains constant, the viscosity suddenly undergoes a very sharp upturn and eventually results in the overload of the shearing device, and the system turns into solid-like upon cessation of flow. Furthermore, the duration of the lag-time correlates exponentially with the applied shear-rate, in the sense that the lag-time before the viscosity upturn decreases exponentially upon increasing the shear rate.

The difficulty of treating this general case is related to the mathematical complexity of the

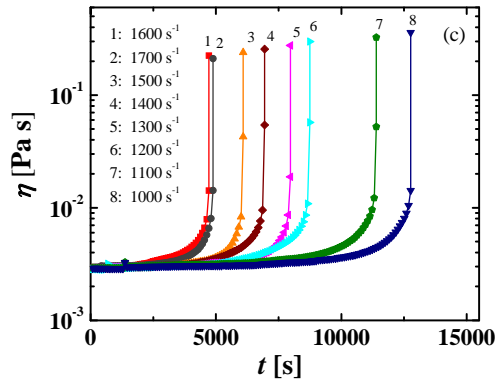


Figure 7.13: Typical time-evolution of the suspension viscosity for charge-stabilized latex particles in laminar shear flow at a varying imposed shear-rate (see legend).

governing equation. This, in the presence of shear, is the convective diffusion equation with an interparticle interaction potential, $U(r)$, which reads:

$$\nabla \left[\frac{D}{k_B T} (-\nabla U + bv) - D \nabla \right] c = 0 \quad (7.46)$$

where b is the hydrodynamic drag acting on a particle, v is the particle velocity due to the flow and c is the concentration of particles. This equation is a partial differential equation in three-dimensional space and cannot be solved analytically. Further problems are due to the flow velocity term (linear in the radial distance r) which diverges at infinity. However, since our problem is to determine the collision frequency, this equation can be reduced to an ordinary differential equation in the radial distance as the independent variable. The underlying simplifying assumption is that one neglects the spatial correlation between the concentration and velocity fields. Integration under the proper boundary conditions for the problem leads to the following generalized kinetic constant for aggregation :

$$\beta_{11} = \frac{16\pi D_0 R}{2 \int_0^{\delta/R} \frac{dx}{\varphi(x)(x+2)^2} \exp(\int_{\delta/R}^x dx [d(U/k_B T)/dx + Pe \tilde{v}_{r,eff}])} \quad (7.47)$$

where x is the surface-to-surface radial distance between the particles, $\tilde{v}_{r,eff}$ is the relative velocity between two particles due to the flow normalized by GR , Pe is the Peclet number (i.e. the ratio between the shear and the Brownian forces) and $\varphi(x)$ is a hydrodynamic function accounting for the resistance of the solvent being squeezed when the two particles approach each other. δ is the thickness of the hydrodynamic boundary-layer (a function of the Peclet

number and of the interaction range). This expression is still sufficiently complicated, where the integrals need be evaluated numerically. A further simplification can be done by considering the limits of a high interaction potential barrier and moderate Peclet number. Under these conditions, the previous expression reduces to the following simple relationship:

$$\beta_{11} = \sqrt{Pe - (U''_m/k_B T)} \exp(-U_m/k_B T + 2Pe/3\pi) \quad (7.48)$$

where U_m is the value of the interaction potential at the maximum of the barrier and U''_m is the second derivative evaluated at the maximum. Since the Peclet is proportional to the shear rate ($Pe = 3\pi\mu GR^3/k_B T$, where μ is the solvent viscosity, k_B is Boltzmann's constant, and T is the absolute temperature) this formula explains the observed exponential dependence of the lag-time preceding the viscosity upturn upon the shear-rate in terms of the attempt time (activation delay) for the shear-induced aggregation of particles with a potential barrier. The exponential scaling with the shear-rate predicted by this formula is in fairly good agreement with experimental observations.

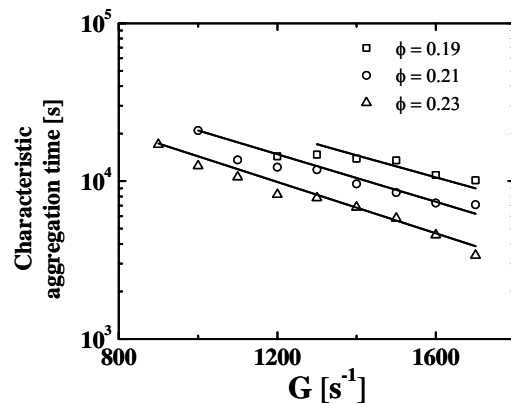
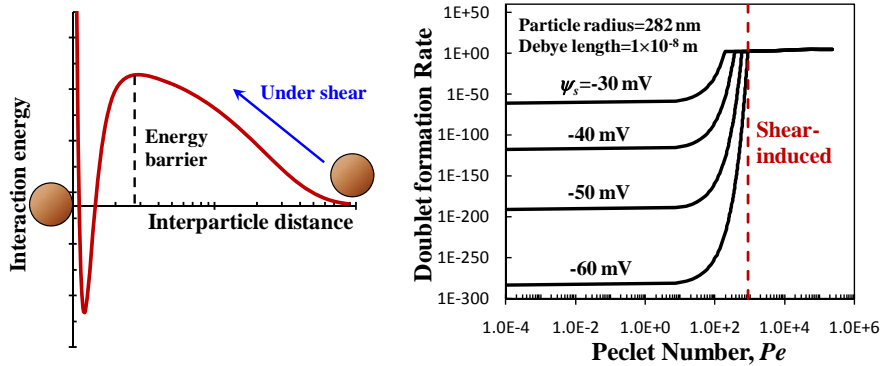


Figure 7.14: Characteristic aggregation time as a function of the applied shear-rate.

To better illustrate the physical meaning of the above expression the right panel of the following figure shows the aggregation rate constant, β_{11} as a function of the Peclet number Pe , for four values of the surface potential, ψ_s , which are typical for DLVO-interacting colloidal systems. It is seen that there are two regimes separated by the broken line: on the left hand side (small Pe values), the aggregation rate is very small and sensitive to the surface potential, while on the right hand side (large Pe values) it is substantially larger and practically independent

of the surface potential. This defines the critical Pe value separating Brownian- from shear-induced aggregation.



7.5.2 Shear induced Breakage

In the presence of strong shear rates, another phenomenon arises which is usually not present under stagnant conditions: cluster breakage. Fluid velocity gradients are not only capable of accelerating the rate of aggregation, but also to break clusters into two or more fragments and also to restructure them, i.e., to increase the primary particles packing density inside a cluster. Both phenomena are strongly coupled, since a more open cluster will be easier to break than a denser one. In addition, cluster breakage also depends on the strength of inter-particle bonds, on cluster size and on the shear rate. Up to know, no complete theory exist which is capable of fully capturing the details of breakage. A typical semi-empirical expression for the breakage rate constant of a cluster with mass i is the one proposed by Delichatsios and Probstein in 1976 and later modified by Kusters in 1991:

$$\beta_i^{\text{break}} = \frac{4}{15\pi} G \exp\left(-\frac{B}{G^2 R_i}\right) \quad (7.49)$$

Equation (7.49) shows that the rate of breakage increases as the shear rate increases (in a non linear fashion for small shear rates, linearly for large shear rates) and increases as the cluster size R_i increases following a sigmoidal trend. The constant B empirically accounts for all dependencies upon structure, material and particle-particle interactions. It is noteworthy that equation (7.49) is just one of the many available expressions proposed to model the rate of breakage, even though it is probably the most commonly used one.

One of the major difficulties related in the modelling of breakage events is that the rate of breakage is not the only piece of information required to construct a mathematical model for coagulation in the presence of shear. In fact, it is necessary to also know the distribution of fragments generated in a breakage event. Unfortunately, it is very difficult to obtain the fragment distribution function both theoretically and experimentally. Usually, either simple binary breakage or fragmentation of a cluster into a specific number of equal size fragments are assumed.

One significant difference between a breakage event and an aggregation event is that breakage is a first order kinetic process, i.e., the rate of breakage is proportional to the first power to the cluster concentration, while all aggregation mechanisms discussed so far are second order kinetic processes, because they require the collision of two clusters. This implies that the formulation of population balance equations (PBE) changes substantially when breakage is present. The PBE (equation (7.8)) in the presence of shear can be formulated as follows:

$$\frac{dN_k}{dt} = \frac{1}{2} \sum_{i=1}^{k-1} \beta_{i,k-i} N_i N_{k-i} - N_k \sum_{i=1}^{\infty} \beta_{ik} N_i - \beta_k^{\text{break}} N_k + \sum_{i=k+1}^{\infty} \Gamma_{k,i} \beta_i^{\text{break}} N_i \quad (7.50)$$

The last two terms of equation (7.50) provide the contribution due to breakage to the mass balances. The second last term is a mass loss, due to the breakage of clusters with mass k , while the last term is a positive contribution due to formation of clusters with mass k generated by the fragmentation of all clusters with mass $i > k$. The function $\Gamma_{k,i}$ is the fragment distribution function, which is defined as the number of fragments with mass k generated by breaking a cluster with mass i .

7.6 Gelation of Colloidal Suspensions

7.6.1 The Gelation Process

During aggregation clusters continuously grow in size. Taking the radius of the smallest sphere enveloping the cluster of mass i as the cluster dimension, R_i , we can compute the cumulative volume fraction occupied by all clusters, as follows:

$$\phi(t) = \sum_i \frac{4}{3} \pi R_i^3 N_i \quad (7.51)$$

where N_i is the CMD, for example computed through the PBE (Eq. 7.8). As shown in figure 7.15, $\phi(t)$ increases in time reaching values larger than one. This indicates that the system

CHAPTER 7. KINETICS AND STRUCTURE OF COLLOIDAL AGGREGATES

is becoming increasingly crowded, so that the clusters are not anymore able to diffuse randomly but begin to interact strongly with each other. The consequence is that the liquid-like colloidal dispersion can dynamically arrest or jam to form a solid-like gel, whose properties can be substantially different from their original disperse state, leading to wide applications in many areas such as in producing ceramics, food, medicine, controlled porous materials, drug delivery devices, etc. In particular, during the diffusion-limited cluster aggregation (DLCA) and reaction-limited cluster aggregation (RLCA), the solid-like transition results from interconnections of the fractal clusters when they grow and fill the entire available space. This process, which transforms the original liquid dispersion in a solid-like gel, is referred to as gelation and can be conceptually divided in two steps:

- cluster formation: this is the aggregation process described by the PBE (Eq. 7.8) which continues until the so called arrest time, which is time where the clusters have occupied so much of the space that their movement is seriously hindered. At this point the cumulative volume fraction occupied by all clusters, $\phi(t)$ is of the order of unity. This time can be measured using dynamic light scattering technique;
- cluster interconnection: the substantially arrested clusters interact with each other forming a percolating structure which span the entire available volume. This process is completed at the so called gelation time.

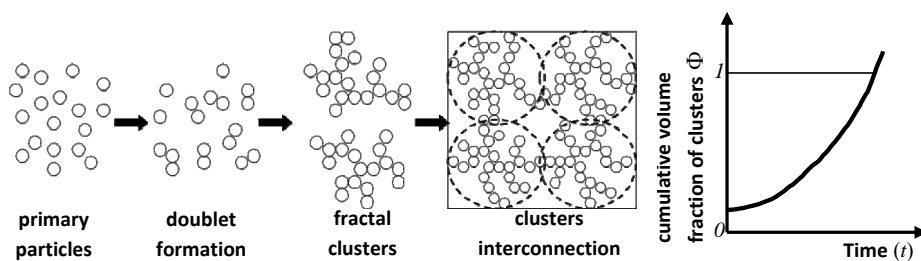


Figure 7.15: Schematic overview on the gelation process

There are various methods to define the critical conditions (time, t_c) for the gelation to occur. The simplest method is through visual observation, i.e., by tilting the aggregation system to see if it ceases flowing. There are more rigorous methods based on measurements of variations in the system physicochemical properties. One of the most commonly used

methods is monitoring elastic modulus (G') of the system, which is near zero in the liquid-like state and sharply increases when the clusters start to interconnect forming the solid-like gel. Another technique that can be well used to define the occurrence of gelation is cross-correlation dynamic light scattering, whose intensity indicates the transition of the system from ergodic (liquid-like) to non-ergodic (solid-like). The three methods mentioned above to define the critical gelation time (t_c) are depicted in the following figure.

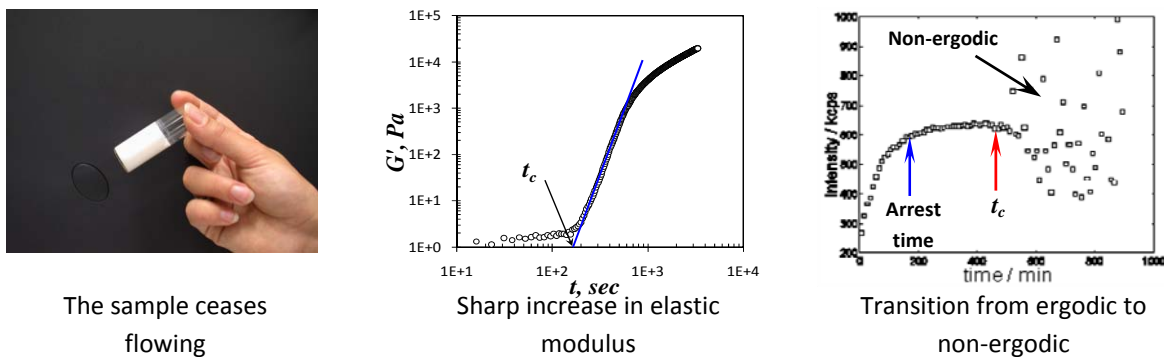


Figure 7.16: Schematic overview on the gelation process

7.6.2 Brownian-Induced Gelation

When a colloidal system is fully or partially destabilized by adding electrolytes, the Brownian-induced aggregation (i.e., DLCA or RLCA) of the particles can lead to gelation if the initial particle volume fraction is large enough (e.g., $\phi > 0.01$). Under DLCA conditions, once the system is in close vicinity to gelation, the interconnection process among the clusters is very fast, due to two main reasons: The first is because every collision between particles and clusters results in a new cluster, i.e., the reactivity is independent of cluster size. The second arises due to the fact that the characteristic CMD of DLCA is rather monodisperse, and all clusters experience approximately the same environment and are on average separated by the same short distance. This view is confirmed by experiments performed on polystyrene colloids, where the gelation time and the arrest time have been measured as a function of solid volume fraction, as shown in the following figure (left panel). It is seen from the figure that the gelation time and the arrest time basically overlap within the experimental error.

It should be mentioned that from practical application viewpoint, gelation under DLCA

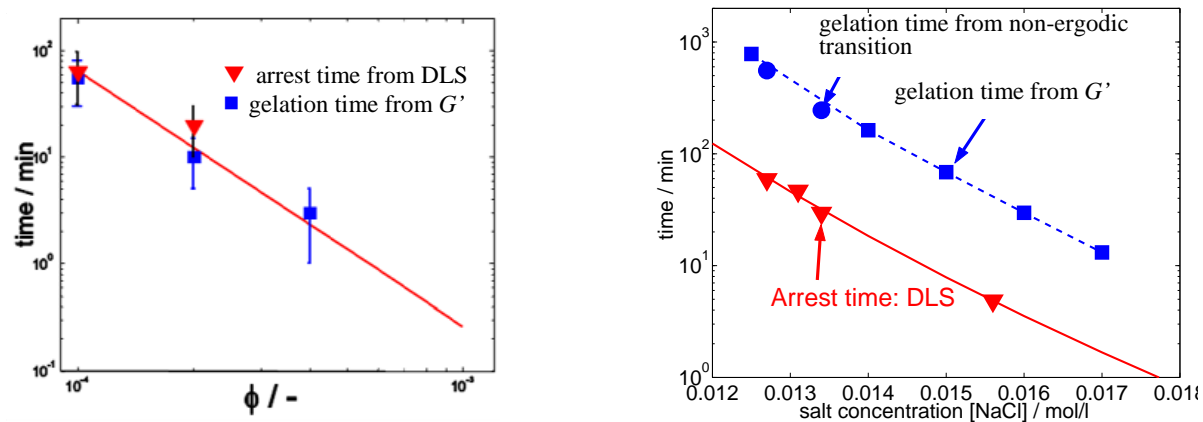


Figure 7.17: Schematic overview on the gelation process

conditions is not the first choice because the process is too fast to obtain homogeneous gels at large solid volume fractions. Instead, gelation under RLCA conditions is more commonly used (e.g. in food and ceramic industry), because the aggregation and gelation rate can be well tuned by the amount of salt added into the system. In this way, gelation can be carried out in a large range of solid volume fractions. In the above figure (right panel), the gelation time and the arrest time measured experimentally are shown as a function of salt concentration for polystyrene particles at a fixed solid volume fraction. One can see that under RLCA conditions, the arrest time is substantially smaller than the gelation time. This is likely due to the broad CMD and different reactivity of the clusters in RLCA. With the wide CMD, although a gel network would be formed by the first few largest clusters, it is rather weak due to the small bonding number, and the system is still dominated by small clusters, which have low reactivity and thus need substantially long time to form a standing gel network.

7.6.3 Shear-Induced Gelation

To form a gel under DLCA and RLCA conditions, one needs to use electrolytes to screen the repulsive energy barrier and then destabilize the colloidal system. Using electrolytes may be undesired because they cannot be fully eliminated after gelation, leading to contamination of the final products. Thus, without adding any electrolytes, one may impose a high shear stress to a colloidal system through fluid motion to force the particle to overtake the energy barrier so as to aggregate and subsequently gelate. Recalling the characteristics of the shear aggrega-

CHAPTER 7. KINETICS AND STRUCTURE OF COLLOIDAL AGGREGATES

tion process discussed in section 7.5.1 and in particular the dependence of the corresponding aggregation rate constant on the Pe number, we can conclude that once the imposed shear is high enough, leading to a Pe value in the shear-induced regime, the aggregation will be extremely fast and independent of the DLVO interactions. This occurs for Pe values larger than the critical value leading to shear-induced aggregation.

In practical applications, shear-induced gelation can be realized by forcing a colloidal system to pass through a microchannel (MC) without adding any electrolyte to screen the DLVO interactions. The left panel of the following figure shows an example of such a device where the capillary exhibits a z-shape with retention times in the order of tens of microseconds and pressure in the range of 20 to 120 bar. The intense shear is generated by forcing the colloidal system to pass through the z-MC under pressure. In general, right after passing through the z-MC, the system can be either a Newtonian liquid or a viscous non-Newtonian liquid or solid-like gel, depending on how many clusters have been generated, which in turn depends on the shear rate, the particle volume fraction and size. One can speculate that if a sufficient amount of clusters is formed in the capillary, gelation occurs and at the MC outlet we have a solid gel having diameter similar to that of the connecting tube. If the conditions for gelation are not reached then the exiting liquid suspension is composed of two distinct classes of clusters: Class 1, constituted mainly of primary particles, and at most some dimers and trimers, and Class 2, constituted of large clusters (or gels) with sizes at least two orders of magnitude larger than that of the primary particles. It is remarkable that clusters with intermediate size are negligible. These two classes can in fact be easily isolated using a 5 μm -opening filter. Such a bimodal CMD is rather different from the CMDs which are typically obtained under DLCA or RLCA conditions, and it is indeed difficult to be explained on physical ground.

On the other hand, when one thinks to the formation of macroscopic pieces of coagulum which is often observed in suspension/emulsion reactors and coagulators, this can certainly not be regarded as an academic curiosity. One possible explanation can be offered by referring again to the critical transition from Brownian to shear induced aggregation (Pe is already above the critical Pe !). Since the Pe number depends upon the third power of the aggregate size, one can speculate that if in an otherwise stable suspension (i.e., under very slow Brownian aggregation) a very few doublets or triplets are formed (for whatever reason) they might enter the shear-induced aggregation regime and grow very fast, following some kind of runaway behavior, leading to the formation of macroscopic pieces of coagulum.

In the case of the shear-induced aggregation in the MC, it is quite reasonable to expect that also breakage plays a role. As a matter of fact, since in general the Pe number is in the order of

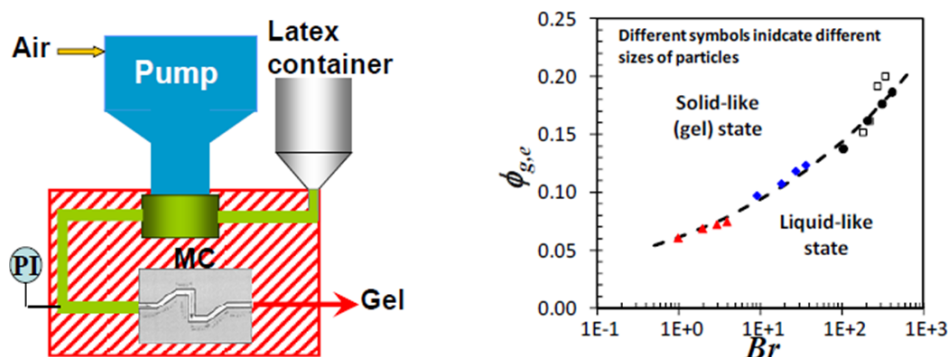
CHAPTER 7. KINETICS AND STRUCTURE OF COLLOIDAL AGGREGATES

$10^3\text{-}10^4$, we should expect the system to be always controlled by shear-induced aggregation. Whether a liquid-like or a solid-like system is obtained at the outlet of the MC should then be related to the competition between the shear generated in the MC and the strength of the aggregates. This is well represented by the Breakage number, Br defined by:

$$Br = \frac{\mu G R_p^3}{U_{min}} = \frac{\mu G R_p^3}{h k_B T} \quad (7.52)$$

Which is the ratio between the shearing energy acting on a particle ($\mu G R_p^3$) and the inter-particle bonding energy (or the energy required to breakup a doublet bond) ($h k_B T$, where h is a coefficient, significantly larger than unity, representing units of $k_B T$ between the primary minimum and the energy barrier on the interparticle interaction curve).

This vision is confirmed by a series of experiments where the critical conditions for the solid-like system (gel) formation have been measured using a z-MC unit for various values of the imposed shear, G and the primary particle radius, R_p . The obtained results expressed in terms of the effective particle volume fraction, $\phi_{g,e}$, are found to perfectly correlate with the Breakage number as shown in the right panel of the figure below. It is seen that the critical particle volume fraction $\phi_{g,e}$ for the shear-induced gelation to occur increases as Br increases. These values form a boundary separating the plane into two regimes: the solid-like gel above the boundary and the liquid-like state below.



As a final remark we note that although the shear-induced gelation is significantly different from the Brownian-induced gelation, they share one feature: the clusters formed in the intense

shear flow within the MC exhibit fractal scaling with fractal dimension equal to 2.4 ± 0.04 , independent of Br , (i.e., of the shear stress, the particle size and the interparticle bonding energy). This is similar to the case of the Brownian-induced aggregations under DLCA and RLCA conditions, which lead to clusters with fractal dimension equal to 1.8 ± 0.05 and 2.1 ± 0.05 , respectively, independent of the particle type and size and the electrolyte concentration.

7.7 Experimental Characterization of Colloidal Suspensions

7.7.1 Light Scattering

Scattering of light, x-rays, and neutrons is probably the most important experimental technique used in the investigation of colloidal systems and aggregation phenomena, because it allows one to gain information about the size of particles and aggregates, the structure of aggregates and gels, and the kinetics of the aggregation process, in a non-invasive way. Of course several other experimental tools have also been used in the investigation of colloidal systems: microscopy (optical, electron, and X-ray) to study size and morphology; rheology to follow the gel formation and to investigate the mechanical properties of the gel phase; ultrasound spectroscopy to monitor particle size in on-line applications. In this chapter we will focus our discussion on light scattering, but most of the results could be almost immediately be applied to both neutrons and x-ray scattering.

In order to better understand the features of light scattering, it is necessary to have an overview of the physical principles and the main results of scattering theory.

Among the three sources: light, neutron and x-rays, light is the most used one for scattering experiments, due to the relatively low cost of lasers which are good quality monochromatic light sources and due to the development in detectors (photomultipliers and fiber optics) and computer-controlled correlators. Another advantage is that light scattering enables one to perform two different kinds of measurements: dynamic light-scattering measurements and static light scattering measurements. In the following, we will briefly review the main concepts of both kinds of measurements. It should be pointed out that most of the static light scattering theory can be also applied to neutron and x-rays scattering experiments.

Light scattering is due to the interactions of electromagnetic waves with matter. When an incident electromagnetic wave shines on a molecule, the electrons feel the interaction and, as a result, the center of mass of the negative charges in the molecule is shifted from its original

CHAPTER 7. KINETICS AND STRUCTURE OF COLLOIDAL AGGREGATES

position. Then, a dipole is formed, which oscillates with the same frequency as the incident radiation. One of the major results of the electromagnetic theory is that an oscillating dipole emits electromagnetic radiation in all directions. This radiation is the scattered radiation. When a sample is illuminated by an incident electromagnetic wave, the sum of the radiations scattered by all the elements of the sample constitute the scattered radiation. The intensity of the scattered light depends strongly on the optical contrast of the scattering object, which is the difference in refractive index between the object and the surrounding medium.

Another way of understanding the scattering problem is the quantum mechanics perspective, where the incident radiation can be viewed as made of photons traveling in a given direction, and due to the *collisions* with atoms of the sample, these photons are deviated, or scattered, keeping however their frequency constant. According to this picture, multiple scattering corresponds to the situation where photons are scattered more than once. Multiple scattering is likely to occur in system with a high concentration of material or in systems with a high optical contrast, when the probability of a photon to be scattered more than once is very high.

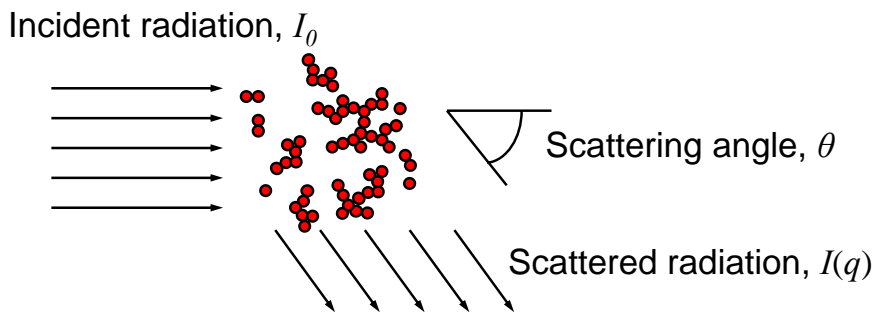
The general treatment of light scattering is quite complex, especially for the most general case where multiple scattering is considered. It requires the full solution of Maxwell equations, which is feasible only for very simple geometries like spheres, cylinders, ellipsoids etc. This arises because the multiple scattering problem is a typical many-body problem: the scattering behavior of one part of the sample has an effect on, and is affected by, all the other parts of the sample. For complex, but always small, systems, where no analytical solutions of Maxwell equations is available, only heavy numerical methods can be used.

Therefore, for most of the applications in the colloidal domain, the interpretation of scattering data is unfortunately limited to those conditions where multiple scattering is absent or can be safely neglected. From an experimental point of view, the conditions where multiple scattering can be neglected are those of low concentration and low optical contrast, where the number of incident photons scattered is a small fraction of the total. An alternative to lowering the concentration of scatterers is the so-called refractive index matching, i.e., finding a solvent that matches as much as possible the refractive index of the scatterer, so that a very low optical contrast can be obtained.

7.7.2 Static Light Scattering

The theory of scattering that neglects multiple scattering is called Rayleigh-Debye-Gans (RDG) theory. The basic assumption is that in every part of the sample, the radiation that illuminates

the sample is only the incident radiation. In this way, the scattering of every part of the system is independent of the others. The theory allows one to compute the profile of the scattered intensity I as a function of the scattering angle Θ , defined as the angle between the directions of the incident radiation and the measurement of the scattered radiation, as shown in next figure.



The existence of an angular dependence of the scattered radiation is because waves scattered from different parts of a sample have a different phases, and that these phase differences become larger as the scattering angle Θ increases. In general, the modulus of the wave vector q of the scattered radiation, equal to the modulus of the difference between the propagation vectors of the scattered and incident radiation, is used instead of the angle θ :

$$q = \frac{4\pi n}{\lambda_0} \sin\left(\frac{\theta}{2}\right), \quad (7.53)$$

where λ_0 is the wavelength of the radiation in vacuum and n is the refractive index of the solvent.

It should be noted that the modulus of the wave vector q has the dimensions of the inverse of a length. Therefore, the quantity $1/q$ represents a length scale, and it gives an indication of the typical size of the objects that contribute to the scattering intensity at the given q value. A better illustration of the meaning of q may be given by an analogy between q and the magnification of a microscope. Looking at the intensity scattered by a sample at different q values is analogous to *observing* the sample by changing the magnification. Low values of q correspond to low magnification, while large values of q correspond to large magnifications and better resolutions. It is obvious from equation (7.53) that changing the scattering angle is not the only way to change the magnitude of q . One can also change the wavelength of the incident radiation. This is one of the reasons why other sources, x-rays and neutrons, are chosen to perform the scattering experiments.

CHAPTER 7. KINETICS AND STRUCTURE OF COLLOIDAL AGGREGATES

X-rays are probably the first source that has been used in the investigation of the structure of materials, particularly crystals. They have been chosen because of their very low wavelength that results in a high resolution. They are usually applied to investigate gels and surfactant solutions. X-rays scattering, particularly small angle x-rays scattering, allows to investigate systems over a broad range of length-scales.

Neutron scattering is based on the scattering of neutrons on the nuclei of atoms. Since neutrons can have a high momentum, which is inversely proportional to their wavelength, neutron scattering also provides a very high resolution. Another advantage is that in the case where the system under investigation is an aqueous solution, the appropriate mixing of water and heavy water (D_2O) enables the elimination of multiple scattering or to change the contrast in such a way that only some part of a sample can be studied. This method is called contrast variation technique.

Static light scattering measurements are to determine the profile of the scattered intensity as a function of the modulus of the wave vector q . To be more quantitative, we consider a sample made of N subunits, having all the same optical properties. In this case, the intensity of the scattered radiation is given by:

$$I(q) = \frac{I_0}{r^2} \sum_{j=1}^N \sum_{m=1}^N b_j(q) b_m^*(q) \exp(-i \mathbf{q} \cdot (\mathbf{R}_j - \mathbf{R}_m)), \quad (7.54)$$

where I_0 is the intensity of the incident radiation, r is the distance of the sample from the detector (assumed to be much larger than the size of the sample), \mathbf{R}_j is the vector defining the position of the center of the j^{th} subunit with volume V_j , i is the imaginary unit, the asterisk defines the complex conjugate, and the quantity $b_j(q)$, called scattering length, is defined as follows:

$$b_j(q) = \frac{\pi n^2}{\lambda_0^2} \left(\frac{n_p^2 - n^2}{n_0^2} \right) \int_{V_j} \exp(-i \mathbf{q} \cdot \mathbf{r}_j) d^3 r_j, \quad (7.55)$$

where n_p is refractive index of the material, n_0 is the average refractive index of the dispersion (material and dispersant) and \mathbf{r}_j is the vector defining the coordinate of a point inside the j^{th} subunit at a distance r_j from its center of mass. It is important to notice that equation (7.54) is very general, and holds true not only for light scattering but also for neutron and x-rays scattering. The only difference for different radiation sources is the dependence of the scattering length on the physical properties responsible for the scattering behavior of the system, namely the term multiplying the integral in equation (7.55).

From equations (7.54) and (7.55) three very important features of intensity of scattered light can be recognized. First of all, the scattered intensity is proportional to the reverse

fourth power of the wavelength. This explains among others why the sky appears blue: the component of white sun's light which is diffused more heavily by dust particles and water droplets is blue light (low wavelength). The second important feature is that the intensity of scattered light is proportional to the square of the volume of the object. Therefore, in the presence of a population of large and small particles, the amount of light scattered by large particles easily overwhelms that of small particles. The third feature is that the intensity of scattered light strongly depends on the optical contrast between the material and the medium around it. If the optical contrast is reduced to zero, the intensity of scattered light also goes to zero.

Since equation (7.54) is quite complex, requiring the knowledge of the relative distances among the various subunits in the sample, it is useful to consider a special case of equation (7.54) that is very important for all colloidal applications. In particular, let us assume that all the subunits are equal and of spherical shape, then equation (7.54) takes the form:

$$I(q) = I_0 K_1 N V_p^2 P(q) S(q), \quad (7.56)$$

where V_p is the volume of one spherical particle, K_1 is a constant that incorporates the dependence of equation (7.54) on the optical constants, $P(q)$ is called particle form factor and depends on the geometrical shape and size of a particle, and $S(q)$ is the structure factor, which depends on the correlations among the particles. In the case of spherical particles, the form factor $P(q)$ is given by:

$$P(q) = \left[\frac{3(\sin(qR_p) - qR_p \cos(qR_p))}{(qR_p)^3} \right]^2, \quad (7.57)$$

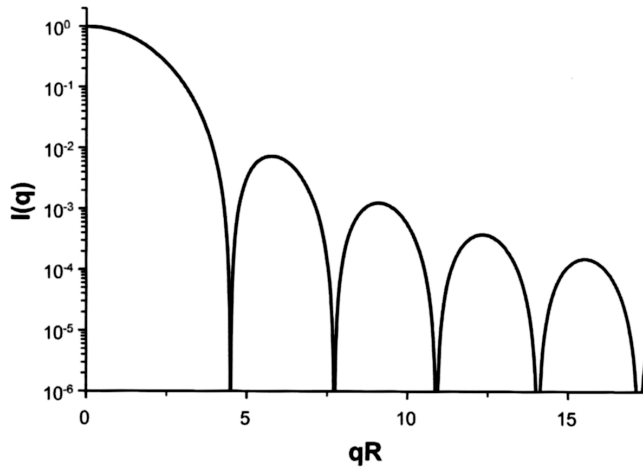
The form factor for a sphere is plotted in the next figure.

This formula is correct usually for particles sufficiently smaller than the wavelength of the radiation (about 10 times smaller), and with a low optical contrast. If the particles do not fulfill these requirements, the RGD theory cannot be applied to interpret the scattering profile of particles. Instead, the full scattering theory, referred to as Mie theory, has to be used.

From a Taylor expansion of the particle form factor, one can derive a very useful relation:

$$P(q) = 1 - \frac{1}{3}q^2 R_{g,p}^2, \quad (7.58)$$

where $R_{g,p}$ is the primary particle radius of gyration. Equation (7.58) suggests that, from the bending of the form factor, one can estimate the radius of gyration of an object. The radius of



gyration of an object is defined as the sum of the squares of the distances of all his points from the center of mass:

$$R_{g,p}^2 = \frac{1}{i} \sum_{j=1}^i (\mathbf{r}_j - \mathbf{r}_{cm})^2, \quad (7.59)$$

For a continuous object, the sum in the above equation should be replaced by an integral. In the case of a sphere, $R_{g,p} = \sqrt{3/5}R_p$.

The structure factor, $S(q)$, on the other hand, contains information about the structure of the system, i.e., how the particles are arranged. The relation between the structure factor and relative positions of i spherical particles in the system is given by the following expression:

$$S(q) = \frac{1}{i^2} \sum_{m,j=1}^i \frac{\sin(qr_{mj})}{qr_{mj}}, \quad (7.60)$$

where r_{mj} is the distance between the centers of the m^{th} and the j^{th} particles. If the system is dilute enough that no correlations among the particles exist, i.e., the relative distances among the particles are much larger than $1/q$, then $S(q) = 1$ and the scattering intensity depends only on the geometrical properties of the particles.

The general procedure to obtain the structure factor of a system from static scattering measurements is as follows. One first determines the particle form factor $P(q)$ by performing the static scattering measurements for a dilute suspension of particles, where $S(q) = 1$ and the measured profile is only proportional to the form factor. Then, by dividing the scattering profile of the sample by the obtained form factor, the structure factor can be analyzed.

Two kinds of information from the structure factor are crucial in the study of aggregation phenomena. In the case of a dilute suspension of large fractal aggregates, it can be shown that

CHAPTER 7. KINETICS AND STRUCTURE OF COLLOIDAL AGGREGATES

the structure factor has typically a power-law behavior within a certain q -range:

$$S(q) \sim q^{-d_f}, \quad (7.61)$$

so that from the slope of $S(q)$ in a double logarithmic plane the cluster fractal dimension d_f can be extracted. The validity of this procedure will be subsequently discussed in the case of small clusters and in the case of gels. Another important quantity that can be determined from the scattering profile is the radius of gyration. It can be obtained by using a Taylor expansion similar to what was done for a single particle. This procedure is called Zimm plot analysis:

$$P(q)S(q) = 1 - \frac{1}{3}q^2R_g^2, \quad (7.62)$$

where a linear region can be found when plotting $P(q)S(q)$ versus q^2 , the slope of which is proportional to the square of the radius of gyration of the system.

All the theory summarized above refers to a system in which there is no polydispersity. When a polydisperse system is analyzed, the effect of the polydispersity on the scattered intensity has to be taken into account. It can be seen from equation (7.56) that, since the intensity scattered by each particle is proportional to the square of its volume (proportional to the square of the mass), large particles contribute much more to the total scattered intensity than small particles. In particular, in the case of a dilute population of particles with m different classes of particles, the total scattered intensity becomes:

$$I(q) = I_0 K_1 \sum_{j=1}^m N_j V_{p,j}^2 P_j(q), \quad (7.63)$$

where N_j , $V_{p,j}$ and $P_j(q)$ are respectively the number, volume and form factor of the j^{th} class particles. Moreover, even for a monodisperse colloidal system, when the aggregation of the primary particles occurs, since the population of aggregates is often broad, the expression of the scattered intensity becomes:

$$I(q) = I_0 K_1 V_p^2 P(q) \sum_{i=1}^{i_{\max}} N_i i^2 S_i(q), \quad (7.64)$$

where N_i and $S_i(q)$ are the number and structure factor of a cluster with mass i and i_{\max} is the largest mass of the clusters in the population.

Consistently, the measured radius of gyration will be an average value $\langle R_g \rangle$, which, can be

written in the following form:

$$\langle R_g \rangle^2 = \frac{\sum_{i=1}^{i_{\max}} N_i(t) i^2 R_{g,i}^2}{\sum_{i=1}^{i_{\max}} N_i(t) i^2}. \quad (7.65)$$

Equation (7.65) shows that the average radius of gyration receives a much greater contribution from large clusters than from small clusters. This is again a consequence of the dependence on the square of the volume of the radiation scattered by an object.

7.7.3 Dynamic Light Scattering

The second scattering technique often used in the study of the colloidal systems and aggregation phenomena is dynamic light scattering, which measures, instead of the scattered intensity as a function of the scattering angle, the rapid fluctuations of the intensity at one specific angle. In a colloidal suspension, the configuration of the system changes rapidly with time due to the Brownian motion of the particles, and consequently, so does the pattern of the scattered radiation. Moreover, such random motion of the particles (or clusters) results that the configuration of the system at a certain time t loses quickly any correlation with its initial status. An effective way to analyze such irregular change in the scattered intensity induced by the random motion of particles (or clusters) is to compute the intensity time autocorrelation function $\langle I(q, 0)I(q, \tau) \rangle$:

$$\langle I(q, 0)I(q, \tau) \rangle = \lim_{T \rightarrow \infty} \frac{1}{T} \int_0^T I(q, t)I(q, t + \tau) dt, \quad (7.66)$$

where $I(q, t)$ is the scattered intensity at time t and τ is the delay time. When the delay time $\tau = 0$, the intensity autocorrelation function is equal to the mean square intensity, and it decays to the square of the average intensity when the delay time τ goes to infinity. For the latter, the system has lost any correlation with its initial configuration. The above analysis is possible only if the system is fully ergodic, i.e., as time goes by, the system has the freedom to probe all the possible configurations and does not retain memory of previous stages. Dynamic light scattering can be used to investigate even concentrated colloidal suspension, to recover interesting information about the mobility of particles at high volume fractions and in the presence of multi-body interactions, but through a very complicated and sophisticated analysis. In this paragraph we will focus our attention only on the case of dilute colloidal suspensions.

CHAPTER 7. KINETICS AND STRUCTURE OF COLLOIDAL AGGREGATES

It is useful to introduce the normalized intensity autocorrelation function:

$$g^{(2)}(\tau) = \frac{\langle I(q, 0)I(q, \tau) \rangle}{\langle I(q) \rangle^2}, \quad (7.67)$$

where $\langle I(q) \rangle$ is the average intensity. It can be shown that $g^{(2)}(\tau)$ is related to another autocorrelation function, the electric field autocorrelation function $g^{(1)}(\tau)$, defined as:

$$g^{(1)}(\tau) = \frac{\langle E(q, 0)E^*(q, \tau) \rangle}{\langle I(q) \rangle}, \quad (7.68)$$

where $E(q, \tau)$ is the electric field of the scattered wave at delay time τ and wave vector q , and $E^*(q, \tau)$ is the complex conjugate. The relation between the two autocorrelation functions is called Siegert relation:

$$g^{(2)}(\tau) = 1 + \sigma \left(g^{(1)}(\tau) \right)^2, \quad (7.69)$$

where σ is a constant that depends on the specific configuration of the detector used in the experiment, but it is always smaller than unity and approaches 1 with increasing the detector area. It can be shown that in the case of a dilute suspension of equal size, non-interacting spherical particles, the field autocorrelation function decays exponentially, and the time constant is proportional to the particle diffusion coefficient D_{iff} :

$$g^{(1)}(\tau) = \exp(-D_{\text{iff}}q^2\tau). \quad (7.70)$$

From equation (7.70), it can be seen that the faster the particle move, the larger their diffusion coefficient and the faster is the decay of the exponential. Therefore, by measuring $g^{(2)}(\tau)$, $g^{(1)}(\tau)$ can be extracted using the Siegert relation, equation (7.69), and from the slope of the logarithm of $g^{(1)}(\tau)$, one can determine the diffusion coefficient, and consequently the hydrodynamic radius R_h using the Stokes-Einstein relation:

$$D_{\text{iff}} = \frac{kT}{6\pi\eta R_h}, \quad (7.71)$$

For a sphere, the hydrodynamic radius is equal to the sphere radius. For any other body, equation (7.71) defines the hydrodynamic radius as the size of the equivalent sphere that experiences the same friction as the body.

In the case of a polydisperse suspension, equation (7.70) does not hold any longer. The contribution of particles (clusters) of different sizes to the total field autocorrelation function is proportional to their masses squared and to their scattering form factors (structure factors).

In the case of a population of clusters, equation (7.70) becomes:

$$g^{(1)}(\tau) = \frac{\sum_{i=1}^{i_{\max}} N_i i^2 S_i(q) \exp(-D_{\text{eff},i} q^2 \tau)}{\sum_{i=1}^{i_{\max}} N_i i^2 S_i(q)}. \quad (7.72)$$

It is clear that measurements performed at different angles, i.e., at different q values, give different results. An important consequence of equation (7.72) is that only an average diffusion coefficient can be estimated, and therefore an average hydrodynamic radius $\langle R_h \rangle$:

$$\langle R_h \rangle = \frac{\sum_{i=1}^{i_{\max}} N_i(t) i^2 S_i(q)}{\sum_{i=1}^{i_{\max}} \frac{N_i(t) i^2 S_i(q)}{R_{h,i}^{\text{eff}}}}, \quad (7.73)$$

where $R_{h,i}^{\text{eff}}$ is an effective hydrodynamic radius of a single cluster with mass i , accounting also for the rotational diffusive motion of the cluster.

From Eqs. (7.73) and (7.65), it can be seen that dynamic light scattering and static light scattering allow one to determine two different average sizes of the CMD. These sizes are independent moments of the CMD, and contain independent information on the width of the CMD, thus useful information for the CMD analysis. These are also the formulas that allow one to relate measurable quantities to the results of PBE computations.

7.8 Zeta Potential, Electrophoretic Mobility, and Surface Charge Density

When working with electrostatically stabilized particles, it is particularly important to determine their surface charge status. This is typically carried out by using a combination of techniques.

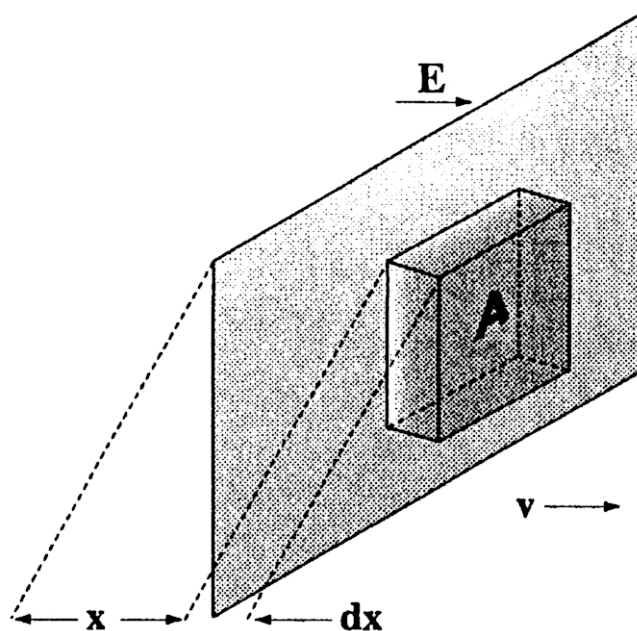
The first step usually consists in measuring the surface charge density, or to be more precise the maximum surface charge density. Potentiometric titration can be used for this purpose. Potentiometric titration consists in using either a concentrated base or a concentrated acid, which are added in small quantities, and simultaneously measuring the conductivity of the suspension. Titration works exactly as in the case of common acids or base solutions. It

CHAPTER 7. KINETICS AND STRUCTURE OF COLLOIDAL AGGREGATES

allows one to measure the point of zero charge of a colloidal particles, which corresponds to the point where all of its charges have been neutralized. From a simple material balance, the total amount of base (acid) used to achieve neutralization can be related to the amount of surface charge.

However, another physical property is very commonly used to extract information on the surface charge of particles: the electrophoretic mobility. It is well known (and also rather intuitive) that a charged particle moves in the presence of an external electric field. The velocity at which the particle will move is linearly proportional to the applied electric field. The electrophoretic mobility is defined as the ratio between the velocity at which the charged particle moves and the applied electric field.

Developing a comprehensive theory which accounts for all the physics involved in the study of the electrophoretic mobility is a demanding task. In the following, we will therefore restrict us to the case where particles are surrounded by a thin double layer. This occurs in the presence of a sufficient amount of electrolytes. Since the thickness of the double layer is small compared to the size of a particles, one can use planar geometry to perform a few simple calculations. The next figure shows the geometry.



We consider a small slab of fluid parallel to a charged planar surface. In the presence of an electric field, there are two forces acting on the small slab of fluid: the electrostatic force and

CHAPTER 7. KINETICS AND STRUCTURE OF COLLOIDAL AGGREGATES

the viscous drag force, and the two have to balance each other. The electrostatic force per unit volume is equal to:

$$F_{\text{el}} = E\rho \quad (7.74)$$

where E is the electric field and ρ is the volume charge density. The viscous drag is instead equal to:

$$F_{\text{vis}} = \eta \frac{d^2v}{dx^2} \quad (7.75)$$

where η is the dynamic viscosity, and v the fluid velocity. By equating the two forces, and making use of Poisson equation to express the charge density as a function of the electrostatic potential, one obtains the following equation:

$$\epsilon \frac{d^2\psi}{dx^2} E = -\eta \frac{d^2v}{dx^2} \quad (7.76)$$

A first integration of this equation leads to:

$$\epsilon \frac{d\psi}{dx} E = -\eta \frac{dv}{dx} + C \quad (7.77)$$

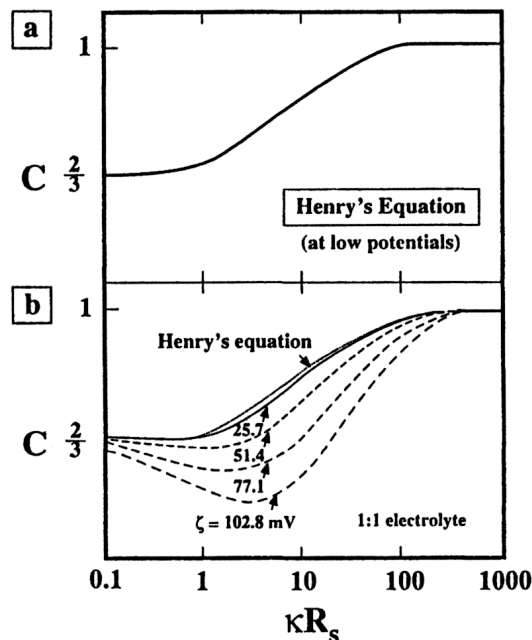
where the arbitrary constant C has to be equal to zero since at infinite distance from the surface both $d\psi/dx$ and dv/dx have to be equal to zero, meaning that both electric field and velocity field are constant at infinite distance from the surface. A second integration can be carried out from the so-called shear plane, i.e., the position where the velocity is zero (which is located very close to the surface) and the potential equal to the so-called ζ -potential, and outside the double layer, where the electrostatic potential equals zero and the velocity equals the particle velocity v . The final expression for the electrophoretic mobility u is:

$$u = \frac{v}{E} = \frac{\epsilon\zeta}{\eta} \quad (7.78)$$

The most remarkable feature of equation (7.78) (originally derived by Smoluchowski) is that the electrophoretic mobility u is independent of the particle size, and only depends on the value of the ζ -potential. The concept of ζ -potential is very important in colloidal science. Since the ζ -potential is the potential at a position very close to the surface (even though it is *not* the potential at the surface), it provides very useful information about the surface charge status of the particles. This information is complementary to that provided by titration. In fact, the shear plane, where the zeta potential is measured, is located outside the Stern layer. It therefore accounts for the net charge of a particle, i.e., both the surface charge and the counterions located within the inner Helmholtz plane. This net charge enclosed within the

surface of shear, is smaller than the charge estimated from titration measurements, but more useful in studying colloidal stability of particles.

Equation (7.78) is only valid for small double layers compared to the particle size. When instead the double layer is larger than the particle size, Debye proved that the electrophoretic mobility is equal to $2/3$ of the values predicted by equation (7.78). A more complete theory, developed by Henry, provides accurate results for all double layer thicknesses, but only for low surface potentials, and shows that the electrophoretic mobility increases monotonically from the Debye limit to the Smoluchowski limit. However, a non-monotonic behavior is observed for high surface potentials, as shown in the next figure. These curves are obtained using more complex numerical calculations. In addition, a weak dependence on the type of electrolyte present in the system has been also observed.



Nowadays electrophoretic mobility is most often measured through a combination of DLS and electrophoresis. In fact, in the presence of an electric field, the field autocorrelation function of a particle takes the following form:

$$g^{(1)}(\tau) = \exp(\pm iqEu\tau) \exp(-D_{\text{eff}}q^2\tau). \quad (7.79)$$

where i is the imaginary unit. Therefore, the autocorrelation function shows a typical oscillating pattern in the presence of an electric field, the frequency of which equals qEu . The

CHAPTER 7. KINETICS AND STRUCTURE OF COLLOIDAL AGGREGATES

electrophoretic mobility can then be obtained by fitting the frequency of these oscillations, and from this the particles zeta potential is calculated.

Chapter 8

Protein Aggregation

8.1 Introduction

Protein aggregation is a challenging topic with crucial implications in several fields, such as human health and drug production. More than 20 human neurodegenerative diseases, including Alzheimer's and Parkinson's diseases, are indeed known to be associated with the formation of fibrillar protein aggregates *in vivo*. Moreover, the aggregation of therapeutic proteins is a significant hurdle in protein drug development, hindering rapid commercialization of potential drug candidates. Aggregation is indeed the major protein instability encountered in almost all stages of therapeutic protein manufacturing, including expression from the cells, purification, storage, shipping and administration to the patient. As the presence of protein aggregates in pharmaceuticals may compromise drug safety and drug efficacy, the protein aggregate content must be strictly controlled to assure satisfactory product quality. There is therefore a need for gaining knowledge on the mechanisms of protein aggregation at a fundamental level with a view to optimizing operative parameters, i.e. mainly the solution composition through the choice of solution pH, excipients type and concentration. As an illustrative example, Figure 8.1 shows some pictures of protein aggregates obtained by Transmission Electron Microscopy (TEM).

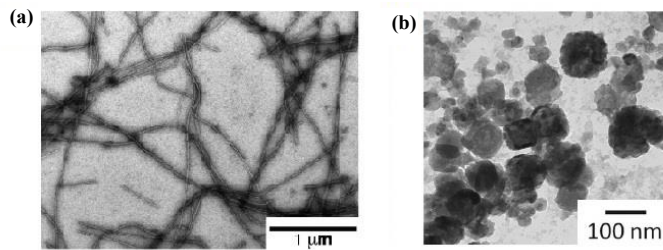


Figure 8.1: TEM pictures of protein aggregates. (a) α -synuclein fibrils (involved in Parkinson's disease) produced *in vitro* (from Campioni, JACS, 2014) (b) Antibody amorphous aggregates obtained after stirring stress (from Telikepalli, Pharma. Biotech., 2014).

Although protein solutions are molecular mixtures and thus represent true solutions, they can be treated in many respects such as colloidal dispersions. Protein sizes are indeed typically in the order of a few nanometers, and are thus lying in the colloidal range. Proteins are therefore small enough to be affected by Brownian motion, but sufficiently large compared to solvent molecules so that the solvent can be considered as a continuum. In this chapter, we show how the kinetics of protein aggregation can be examined under the light of colloid science.

8.2 Monoclonal Antibodies

Monoclonal antibodies (mAbs) occupy a large and growing part of the pharmaceutical market and represent promising therapies in the treatment of several human diseases, such as cancer or rheumatoid arthritis.

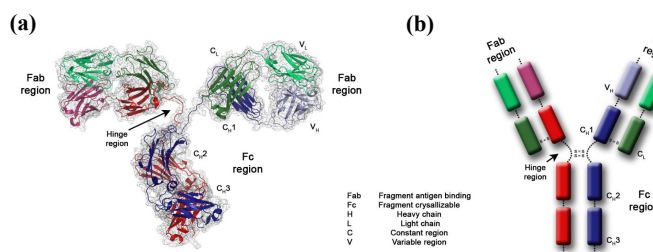


Figure 8.2: Structure of a monoclonal antibody. (From badrilla.com)

Antibodies, also known as immunoglobulins (Ig), are large (150 kDa) Y-shaped proteins composed of three equal-sized regions: a Fc region and two Fab regions, as shown in Figure 8.2. Different antibodies have different antigen binding regions (Fab), but they share the same constant region (Fc) within the same class (IgG, IgM ...).

8.3 Protein Colloidal Stability

To make use of the concepts developed for colloid science, proteins can be regarded at the molecular level as uniformly charged spheres. In the frame of this approach, it is of interest to evaluate a global protein net charge in order to estimate the contribution of the electrostatic repulsion to the protein colloidal stability. To this end, the protein net charge can be either computed theoretically from the protein amino-acid primary sequence, or measured experimentally by using biophysical techniques such as electrophoretic mobility.

Briefly, as in the case of polymer colloids, zeta potential values (ζ) of proteins can be evaluated from the measurement of the electrophoretic mobility (μ) according to the Henry equation:

$$\mu = \frac{2\epsilon\zeta}{3\eta} \quad (8.1)$$

where ϵ and η are the dielectric constant and the viscosity of the medium, respectively.

The protein net charge can then be estimated from the measure of the zeta potential according to the following equation:

$$Z = \frac{4\pi\epsilon R_p}{e} (1 + \kappa R_p) \zeta, \quad (8.2)$$

Where R_p is the protein radius, e is the elementary charge, and κ is the inverse Debye length. The protein charge changes significantly with the solution pH, as it can be seen in Figure 8.3, which shows the theoretical net charge of a monoclonal antibody as a function of pH. It is then expected that the protein stability strongly depends on the solution pH.

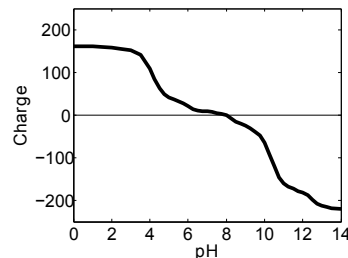


Figure 8.3: Theoretical charge as a function of pH for a mAb.

Moreover, as in the case of traditional polymer colloids, the presence of salt is generally found to destabilize protein solutions. Based on the knowledge of the protein charge, the

CHAPTER 8. PROTEIN AGGREGATION

DLVO theory (presented in Chapter 6) provides a framework to rationalize the impact of solution pH and of salt concentration on the aggregation propensity of proteins.

However, the correlation between protein charge and aggregation propensity is not straightforward, as explained in the following.

8.4 Protein Conformational Stability

As a matter of fact, the protein stability does not result only from the *protein colloidal stability*, but also from the *protein conformational stability*. While the protein colloidal stability is related to the energy barrier which prevents protein molecules from colliding, the protein conformational stability is related to the energy barrier which prevents protein molecules from unfolding.

Protein unfolding is a monomolecular reaction during which the protein native state (i.e. the properly folded conformational state, which is predominant under biological conditions) undergoes conformational changes, thus leading to a denatured (i.e. unfolded) conformational state of the protein, which is generally less stable than the native state. Protein unfolding can affect both the *protein secondary structure* (i.e. the regular local sub-structure of the molecule, which can for example be an α -helix structure or a β -sheet structure) and the *protein tertiary structure* (i.e. the overall three-dimensional arrangement of the local secondary structures in the entire molecule).

While the protein colloidal stability depends mainly on intermolecular protein-protein interactions, the protein conformational stability is dictated by the delicate balance between intramolecular protein interactions and intermolecular protein-solvent interactions. As a result, both the protein colloidal stability and the protein conformational stability are affected by solution composition, which regulates the type and strength of inter- and intramolecular interactions.

The protein colloidal stability and the protein conformational stability are strongly interconnected and are extremely difficult to investigate independently experimentally. For instance, a decrease in pH below the protein isoelectric point is expected to lead to a higher colloidal stability due to an increase in the protein net charge. However, acidic environments are also known to promote protein unfolding due to intramolecular electrostatic repulsion. Protein unfolding then leads to the exposure of buried hydrophobic patches, which results in strong attractive hydrophobic intermolecular interactions that favor protein aggregation. All in all, a decrease in pH below the isoelectric point is expected to increase the colloidal stability but

to decrease the conformational stability, thus making predictions of the impact of pH on the protein aggregation propensity hardly possible.

Therefore, it is paramount to characterize both the colloidal stability and the conformational stability when assessing the protein stability experimentally. The protein conformational stability is commonly evaluated with Differential Scanning Calorimetry (DSC) from the unfolding temperature obtained during heat-induced protein denaturation, as illustrated in Figure 8.4 (a). Moreover, Circular Dichroism (CD) measurements can be performed in order to get more detailed characteristics of the protein secondary and tertiary structures, as shown in Figure 8.4 (b). For example, a minimum in the CD intensity spectrum at 218 nm is characteristic of the presence of β -sheets structures.

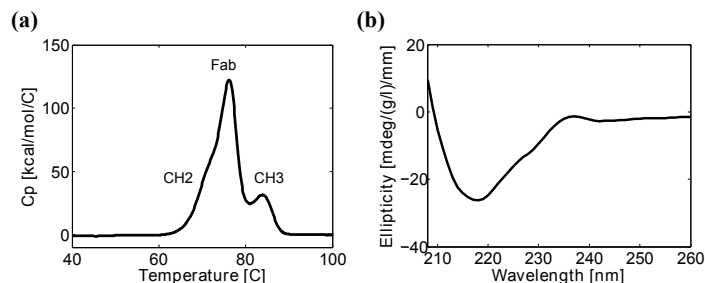


Figure 8.4: (a) Typical DSC thermogram of a mAb, showing three unfolding temperatures, each corresponding to a domain of the mAb. (b) Typical CD spectra of a mAb, indicating the presence of β -sheets structures, as shown by the minimum at 218 nm.

8.5 Mechanisms of Protein Aggregation

Protein aggregation results from a complex multi-step process involving both monomolecular conformational changes and bimolecular aggregation events. The main steps involved in the process of protein aggregation are shown in the scheme of 8.5.

First, a non-native aggregation-prone conformational state of the protein is formed, as a result of changes in the protein secondary or tertiary structures. This intermediate then promotes nucleation of oligomers, which subsequently grow to larger aggregates, either by monomer addition or by aggregate-aggregate assembly. This multi-step aggregation scheme is sufficiently general to describe a large variety of protein aggregation behaviors. However, the quantification of the relative importance of the individual steps in a specific system remains challenging. Kinetic analysis has been proven to be a powerful tool to complement experimental characterization in order to quantify from macroscopic measurements the contribution of elementary

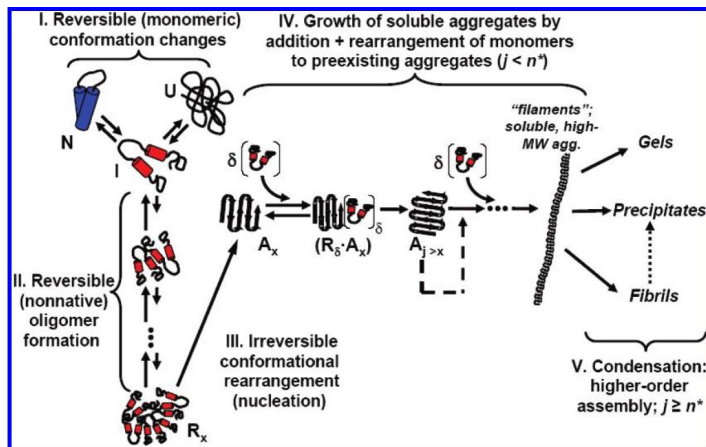


Figure 8.5: Schematic representation of the mechanism of protein aggregation (From Roberts, J. Phys. Chem. B, 2007).

events on the global aggregation process, as will be illustrated in the case studies.

8.6 Aggregation Kinetics and Reaction Order

As in the case of polymer colloids, Static Light Scattering (SLS) and Dynamic Light Scattering (DLS) can be used to follow the increase in the average gyration radius ($\langle R_g \rangle$) and in the average hydrodynamic radius ($\langle R_h \rangle$), respectively. In order to compare results from model simulations with experimental results, the simulated $\langle R_g \rangle$ and $\langle R_h \rangle$ can be reconstructed from the simulated aggregate population by using equations (7.65) and (7.73), respectively.

Moreover, SLS experiments can be performed in order to measure the aggregate fractal dimension, as shown in the case studies below. Indeed, as for traditional polymer colloids, protein aggregates are often found to exhibit fractal morphology.

In addition to the experimental characterization usually applied to follow the kinetics of aggregation of polymer colloids, Size Exclusion Chromatography (SEC) is widely used to quantify the residual monomer (i.e. primary particle) content, as well as the oligomer distribution, in the case of proteins (see Figure 8.6 (a)).

When SEC is coupled with an inline Multi Angle Light Scattering detector, the average aggregate molecular weight (i.e. the average number of monomeric unit per aggregate) can also be monitored as a function of time (see Figure 8.6 (b)). In order to compare results from model simulations with experimental data, the simulated average aggregate molecular weight can be computed from the simulated moments of the aggregate distribution (see equation (2.39)).

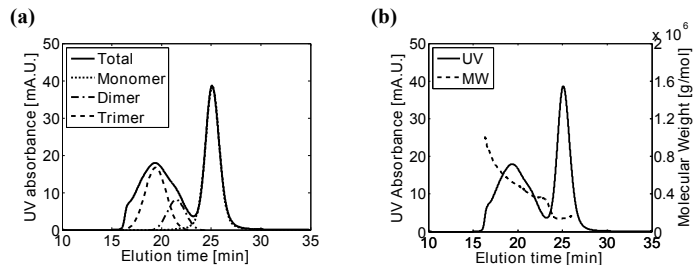


Figure 8.6: Typical SEC chromatogram of a mixture of mAb monomer and mAb aggregates. (a) Determination of the monomer, dimer and trimer content by peak deconvolution (b) Measure of the aggregate molecular weight from Multi Angle Light Scattering.

Monitoring monomer depletion kinetics at several protein concentrations can provide relevant information on the step rate limiting the monomer consumption. In that purpose, it is of interest to describe monomer depletion kinetics in terms of an apparent reaction order n , defined as:

$$\frac{dM}{dt} = -k_{\text{app}} M^n, \quad (8.3)$$

Where M is the monomer concentration followed on a few half-lives and k_{app} is the apparent reaction rate constant for monomer loss. Values of n lying between one and two are typically observed. In particular, $n = 1$ is indicative that unimolecular conformational changes are rate limiting the kinetics of monomer depletion, whereas $n = 2$ rather corresponds to the case where monomer consumption is rate limited by the aggregation events leading to dimer formation.

8.7 Case Studies

In the following, we investigate the aggregation behavior of two mAbs, a glycosylated IgG1 and a non-glycosylated IgG2, denoted as mAb-1 and mAb-2, respectively. The same operating conditions were used for the two mAbs, i.e. neutral pH and thermal stress. As accelerated studies at elevated temperatures are commonly performed in an attempt to assess formulation stability, it is indeed of interest to gain insight into the mechanisms of therapeutic protein aggregation under thermal stress. For the two systems under investigation, we combine experimental characterization with theoretical modeling in order to:

- 1) Identify the key steps involved in the aggregation mechanism
- 2) Study the impact of co-solutes on the kinetics of aggregation

To illustrate our approach, we selected two co-solutes: NaCl and sorbitol, which are common excipients used in drug formulation to provide physiological osmolality and hinder protein aggregation, respectively.

8.7.1 Case Study 1: mAb-1

Experimental Observations

Figure 8.7 shows some experimental observations regarding mAb-1 aggregation. We conclude from these data that, in the case of mAb-1:

- (a) The monomer depletion is rate limited by monomolecular conformational changes
- (b) Aggregation is irreversible
- (c) Aggregates exhibit fractal morphology, with $d_f = 1.85$

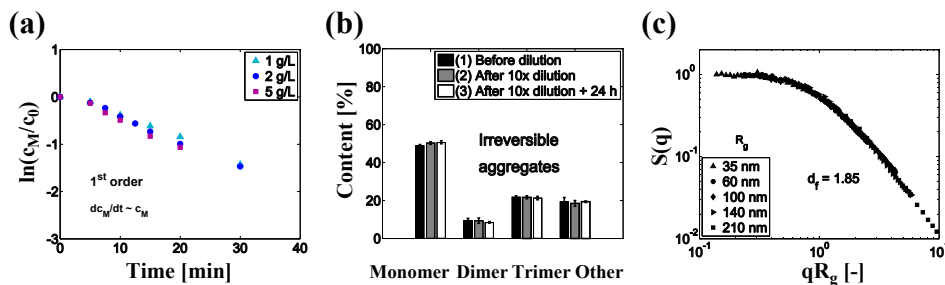


Figure 8.7: Experimental observations for mAb-1. (a) Linearization of the monomer depletion kinetics followed by SEC (b) Dilution experiments to assess aggregates reversibility (c) SLS experiment to measure the fractal dimension of aggregates.

Reaction Scheme

According to these observations, the reaction scheme shown in Figure 8.8 is proposed.

First, the monomer in its native form N unfolds to form U , which is a denatured conformational state of the monomeric protein. This step, denoted as (M1-1) in the kinetic scheme, is regarded as irreversible in this study. Indeed, U can be considered as an intermediate reactive species which is depleted by irreversible aggregation before it can re-fold. Therefore, aggregation is faster with respect to the possible backward reaction of unfolding, and the reversibility of the unfolding step can be neglected. It is worth mentioning that the quantity experimentally accessible from SEC experiments is the sum of the concentrations of N and U , since SEC is

CHAPTER 8. PROTEIN AGGREGATION

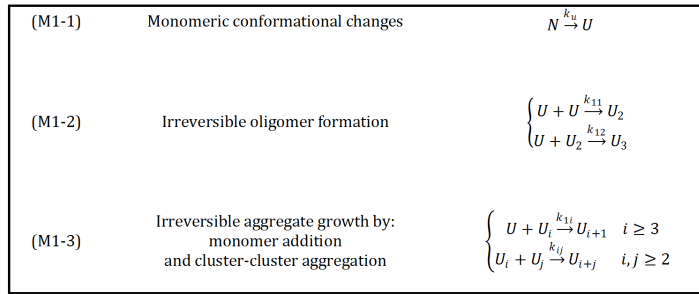


Figure 8.8: Proposed reaction scheme for mAb-1 aggregation.

not sensitive to changes in protein conformation. The aggregation prone form of the protein, U , can then aggregate to form oligomers, according to step (M1-2). Finally, aggregates grow irreversibly either by monomer addition or by cluster-cluster aggregation, as depicted in step (M1-3).

The unfolding step is a simple monomolecular reaction, which can be easily described by a single kinetic rate constant k_u . Describing the aggregation steps is a bit more challenging, though, as it requires the definition of an aggregation kernel which provides a relation between aggregate size and aggregate reactivity. Following the approach presented before in the case of polymer colloids, we first compute the characteristic time for rapid coagulation so as to determine whether or not aggregation occurs under diffusion limited conditions. At 70 °C, with a protein concentration of 1 g/L, we obtain $t_{RC} \approx 10^{-5} s$. Therefore, we conclude that aggregation is not limited by diffusion under these conditions, and we select the traditional RLCA kernel to describe aggregate growth.

However, it must be emphasized that this kernel was derived in the case of spheres uniformly charged, while it is known that protein reactivity strongly depends on protein conformation and on the accessibility of aggregation-prone patches. This effect can be accounted for by introducing different values of the Fuchs stability ratio in order to characterize the stability of different sub-populations of species characterized by a similar reactivity. In particular, the unfolded aggregation-prone monomer U is an unstable intermediate which has a very high reactivity compared to other aggregates species. Therefore, three types of aggregation events characterized by species with different reactivity can be identified: monomer-monomer, monomer-aggregate and aggregate-aggregate. Accordingly, three Fuchs stability ratios are defined: W_{11}, W_{1j} and W_{ij} , which describe oligomer formation, aggregate growth by monomer addition and aggregate growth by cluster-cluster aggregation, respectively.

Population Balance Equations

The kinetic model corresponding to the reaction scheme of Figure 8.8 is given below:

$$\left\{ \begin{array}{l} \frac{dN}{dt} = -k_U N \\ \frac{dU}{dt} = k_U N - U \sum_{j=1}^{\infty} k_{1,j} U_j \\ \frac{dU_{i \geq 2}}{dt} = \frac{1}{2} \sum_{j=1}^{i-1} k_{j,i-j} U_j U_{i-j} - U_i \sum_{j=1}^{\infty} k_{i,j} U_j \end{array} \right. \quad (8.4)$$

With:

$$\left\{ \begin{array}{l} k_{i,j} = k_s B_{i,j} P_{i,j} W_{i,j}^{-1} \\ k_s = 8k_B T / 3\eta \\ B_{i,j} = \frac{1}{4} (i^{-1/d_f} + j^{-1/d_f}) (i^{1/d_f} + j^{1/d_f}) \\ P_{i,j} = (ij)^\lambda \end{array} \right. \quad (8.5)$$

And $W_{11} \neq W_{1j} \neq W_{ij}$

It can be observed that the usual Smoluchowski population balance equations were modified in order to account for features that are specific to proteins: (1) an unfolding step was introduced to reflect monomolecular changes in protein conformation, (2) several Fuchs ratio values were introduced to describe the different reactivities of the various sub-populations present in solution.

Parameter Estimation

The implementation of the proposed kinetic scheme requires the estimation of several parameters. Some of these parameters can be evaluated by independent measurements, while others can be estimated by fitting the suitable quantities to those measured experimentally as a function of time. Since the concentration of U is low and nearly constant due to its high reactivity, the unfolding rate constant k_U can be approximated to k_{app} , which is determined from the linearization of the experimental monomer depletion. The fractal dimension has been measured by SLS and the power law factor λ appearing in the aggregation kernel has been estimated as $\lambda \approx 1 - 1/d_f$. The remaining parameters are the three Fuchs ratios which have been fitted to

CHAPTER 8. PROTEIN AGGREGATION

describe the experimental data at the reference protein concentration of 2 g/L. The parameters used for the simulations are summarized in Table 8.1.

Parameter	k_U	d_f	λ	W_{11}	W_{1j}	W_{ij}
Value	$1 \times 10^{-3} \text{ s}^{-1}$	1.85	0.5	8.5×10^6	4×10^7	8×10^8
Source	k_{app}	SLS Exp.	$1 - 1/d_f$	Fit	Fit	Fit

Table 8.1: Parameters used for the simulations of mAb-1 aggregation (without co-solutes).

In Figure 8.9 (a-c) it can be seen that the simulations are in excellent agreement with the experiments, indicating that the proposed kinetic model can successfully describe the aggregation of mAb-1 under the investigated conditions.

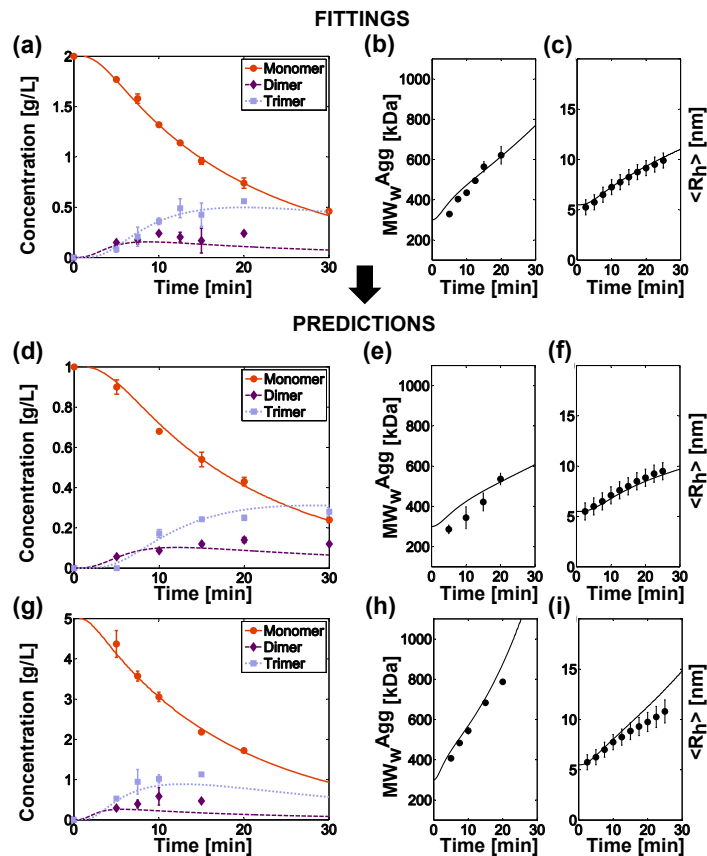


Figure 8.9: Comparison between experimental data and simulations for mAb-1 at protein concentration of 2 g/L (a-c), 1 g/L (d-f) and 5 g/L (g-i). The experimental concentration of monomer, dimer and trimer were determined by SEC. The aggregate molecular weight was measured by SEC-MALS and the average hydrodynamic radius was followed by DLS.

CHAPTER 8. PROTEIN AGGREGATION

The comparison between the different Fuchs stability ratios estimated by the fitting to experimental data provides information on the relative reactivity of the various species involved in the aggregation process. Considering the values reported in Table 8.1, it can be noticed that $W_{11} \ll W_{1j}$. This highlights that, for this system, aggregate growth by monomer addition prevails over aggregate growth by cluster-cluster aggregation, probably due to the high reactivity of the unfolded monomer.

Model Validation

To further validate the proposed kinetic scheme, the kinetics of aggregation were simulated at protein concentrations of 1 g/L and 5 g/L using the same set of values reported in Table I, with no additional parameters. In Figure 8.9 (d-i), it can be seen that the model predictions agree very well with all the experimental results, proving that the model is capable of predicting the concentration effect on the aggregation kinetics of mAb-1 in the concentration range from 1 g/L to 5 g/L.

Conclusion 1: Kinetic Mechanism

We can therefore conclude that the kinetic scheme of mAb-1 aggregation is the one presented in Figure 8.10.

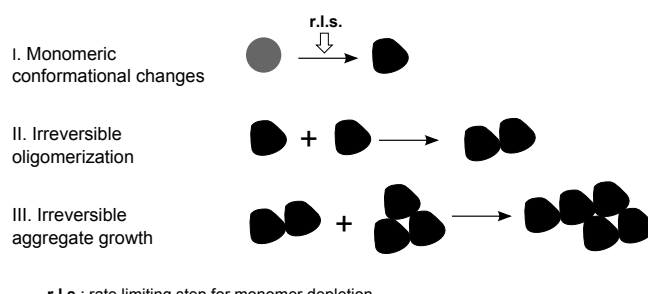


Figure 8.10: Kinetic scheme for mAb-1 aggregation

Comparison with DLVO theory

The kinetic approach used in this study allows the quantification of the inter-particle interaction potentials, expressed in terms of the Fuchs stability ratio, from the reaction rate constants estimated by fitting to the experimental kinetics of aggregation. The estimated value of W_{11} is

CHAPTER 8. PROTEIN AGGREGATION

in the order of 10^7 (Table 8.1). This large value indicates the presence of a high energy barrier that particles must overcome before colliding, which reduces the collision efficiency and thus delays the aggregation process.

However, a low value of zeta potential of the antibody solution was measured ($\zeta \approx 6\text{mV}$). This value corresponds to a protein net charge of around +4 (consistent with the value of the theoretical charge at neutral pH shown in Figure 3). Net electrostatic stabilization is therefore expected to be small under these conditions.

Figure 8.11 shows the computed contribution of the Van der Waals attraction and of the electrostatic repulsion to the total protein-protein interaction potential as a function of the inter-particle distance. The Van der Waals interaction potential was computed from equation (6.7) with $a_1 = a_2$ and $A_H = 3k_B T$, while the electrostatic interaction potential was computed from the modified Hogg-Healy-Fursteneau equation as described in *Jia et al., J. Colloid Interf. Sci., 2006*.

Based on these calculations and on the definition of the Fuchs ratio which is given in equation (7.26), $W_{11}^{\text{DLVO}} \approx 1$ was computed. This low value, which corresponds to the DLCA regime, reflects the low net charge of the antibody solution under these conditions, and is several orders of magnitude smaller than the value estimated by kinetic analysis.

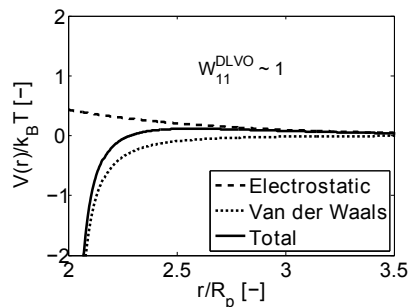


Figure 8.11: Computed protein-protein interaction potential for mAb-1 in the frame of the DLVO theory.

This result strongly indicates that the colloidal stability of this antibody solution cannot be rationalized in the frame of the DLVO theory, which considerably underestimates the repulsive energy barrier between two approaching molecules. The DLVO theory may underestimate the mAb colloidal stability for several reasons including: (i) the low colliding efficiency due to the heterogeneous protein surface, which may provide only limited specific patches prone to aggregate and requires specific geometrical orientation of the two aggregating molecules, in contrast with sticking homogeneous spherical colloids; (ii) additional repulsive non-DLVO repulsion forces, such as hydration, which further contribute to the interaction potential.

Impact of NaCl

In the following, we investigate the impact of NaCl on the aggregation kinetics of mAb-1 at the protein concentration of 1 g/L.

First, the impact of NaCl on the effective protein charge was assessed by zeta-potential measurements. It can be observed in Figure 8.12 (a) that the zeta-potential of mAb-1 decreases from 5.7 mV to a value close to zero upon salt addition.

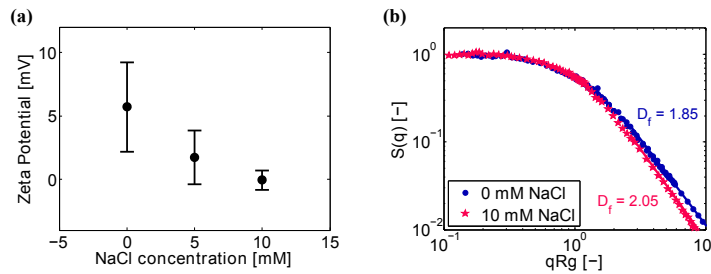


Figure 8.12: Impact of NaCl on the zeta potential fractal dimension for mAb-1.

In addition, the aggregate morphology was investigated by SLS, as shown in Figure 8.12 (b). The results indicate that the presence of NaCl leads to an increase in the fractal dimension. One possible explanation for this trend, which is opposite as the one expected for polymer colloids, lies in the patchiness of the protein surface. Indeed, the fractal dimension value, which is relatively low in the absence of salt ($d_f = 1.85$) considering that aggregation occurs under RLCA conditions, suggests that aggregation is confined to a few aggregation-patches. By screening local charges, the presence of salt then makes the protein surface more uniform. This leads to the formation of more compact aggregates, with a fractal dimension of 2.05, consistent with aggregation occurring under RLCA conditions.

Figure 8.13 shows the experimental data on the kinetics of aggregation of mAb-1 in the absence of salt as well as in the presence of 5 mM and 10 mM NaCl. It can be observed that salt significantly accelerates the increase in aggregate molecular weight during time, while it has only a slight impact on the monomer depletion. In Figure 8.13 (e), it can be seen that at a given monomer conversion, the presence of NaCl induces the formation of larger aggregates, with respect to the situation without salt. This experimental observation suggests that the presence of salt decreases the characteristic time of aggregate growth, while it does not change the characteristic time of monomer depletion, which has been previously shown to be rate-limited by monomeric conformational changes.

Therefore, the analysis of the impact of NaCl on the mAb aggregation kinetics reveals that

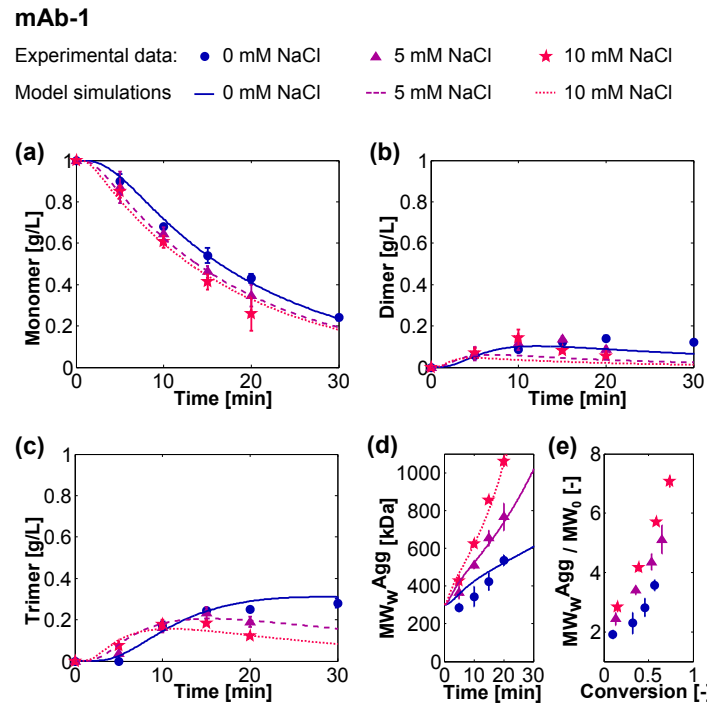


Figure 8.13: Comparison between experimental data and simulations for mAb-1 aggregation kinetics in the absence of co-solute and with 5 and 10 mM NaCl.

the unfolding rate constant is not affected by the presence of salt, while the aggregation rate constants increase upon salt addition, indicating a decrease of the net repulsive intermolecular forces, in agreement with the changes in zeta potential and aggregate morphology described in the previous paragraph. To simplify the fitting procedure, we assumed that salt has the same impact on all the aggregation rate constants. Thus, we introduced a parameter α_1 defined as the ratio between the aggregation rate constants in the presence and in the absence of co-solute. Since the aggregation rate constants are inversely proportional to the Fuchs ratios, α_1 is defined as:

$$\alpha_1 = \frac{W_{11}^{-CS}}{W_{11}^{+CS}} = \frac{W_{1j}^{-CS}}{W_{1j}^{+CS}} = \frac{W_{ij}^{-CS}}{W_{ij}^{+CS}} \quad (8.6)$$

Where $-CS$ and $+CS$ denote the situations without and with co-solute, respectively.

Regarding the two other parameters, the fractal dimension was measured experimentally and the power law factor λ was estimated as $\lambda \approx 1 - 1/d_f$.

The values of the parameters used for the simulations are summarized in Table 8.2.

It can be seen in Figure 8.13 that the model is capable of describing well the time evolution

Parameter	d_f	λ	k_U	α_1
5 mM NaCl	1.94	0.5	$1 \times 10^{-3} s^{-1}$	3.45
10 mM	2.05	0.5	$1 \times 10^{-3} s^{-1}$	7.14
Source	SLS Exp.	$1 - 1/d_f$	Unchanged	Fit

Table 8.2: Parameters used for the simulations of mAb-1 aggregation in the presence of NaCl.

of the different sets of experimental data. In summary, our results show that the presence of NaCl increases the aggregation kinetics of mAb-1 only by promoting the aggregation events, i.e., by reducing the repulsive energy barrier between two colliding particles, without impacting the kinetics of formation of the aggregation prone monomer, i.e., the unfolding step.

Impact of Sorbitol

We now apply the same methodology to study the impact of sorbitol on the aggregation behavior of mAb-1 (still at the protein concentration of 1 g/L).

The results presented in Figure 8.14 show that sorbitol does not impact neither the zeta potential value, nor the aggregate fractal dimension of mAb-1

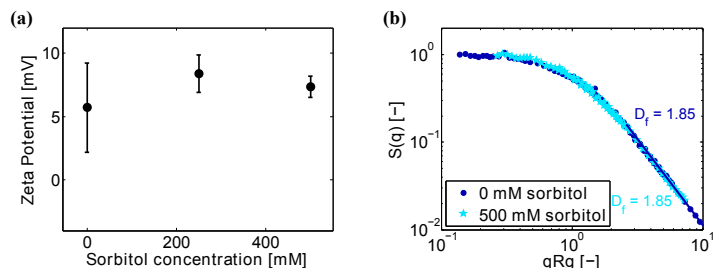


Figure 8.14: Impact of sorbitol on the zeta potential and fractal dimension for mAb-1.

Figure 8.15 presents experimental data of the kinetics of mAb-1 aggregation in the absence of polyol sugar and in the presence of 250 mM and 500 mM sorbitol. It can be observed that sorbitol significantly delays the monomer depletion kinetics, while it has almost no impact on the increase in aggregate molecular weight. Therefore, at a given monomer conversion, the presence of sorbitol induces the formation of larger aggregates compared to the situation without polyol sugar, as can be seen in Figure 8.15 (e). This suggests that the presence of sorbitol increases the characteristic time of monomer depletion, which corresponds to the character-

istic time of protein unfolding, to a larger extent than the characteristic time of aggregate growth.

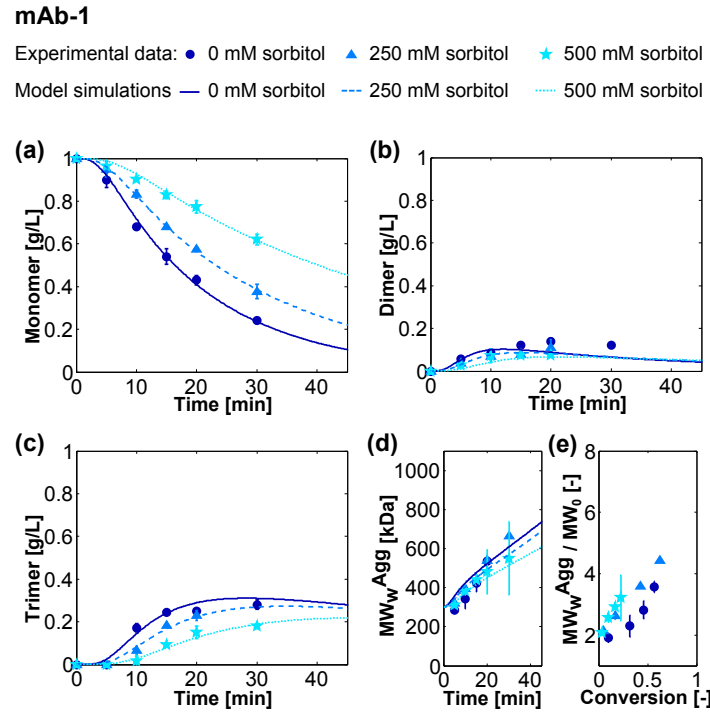


Figure 8.15: Comparison between experimental data and simulations for mAb-1 aggregation kinetics in the absence of co-solute and with 250 mM and 500 mM sorbitol.

The finding that sorbitol does not impact aggregation events is consistent with the experimental observations reported above, which showed that sorbitol neither impacts the protein net charge nor the aggregate morphology of mAb-1.

The parameters used for the simulations are determined as follows: the fractal dimension is measured experimentally, the power law factor λ is estimated as $\lambda \approx 1 - 1/d_f$, the Fuchs ratio values are unchanged compared to the situation without salt, and finally, the unfolding rate constant is fitted to the experimental data. The parameter values used for the simulations are summarized in Table 8.3.

As can be seen in Figure 8.15, the model simulations are in excellent agreement with the experimental data. In particular, it is worth noticing that the slight delay observed in the kinetics of aggregate growth in the presence of sorbitol can be explained by a decrease in the unfolding rate constant only (i.e. without changes in the Fuchs stability ratio), as proven by model simulations. This analysis reveals that sorbitol delays the kinetics of mAb-1 aggrega-

Parameter	d_f	λ	k_U	α_1
250 mM sorbitol	1.85	0.5	$6.7 \times 10^{-4} s^{-1}$	1
500 mM sorbitol	1.85	0.5	$3.5 \times 10^{-4} s^{-1}$	1
Source	SLS Exp.	$1 - 1/d_f$	Fit	Unchanged

Table 8.3: Parameters used for the simulations of mAb-1 aggregation in the presence of sorbitol.

tion only by delaying the kinetics of formation of the aggregation prone monomer without impacting protein reactivity, i.e. sorbitol slows down protein unfolding while it has a negligible impact on the energy barrier that colliding particles must overcome before aggregating.

Sorbitol is known to be excluded from the protein surface due to unfavorable protein-solvent interactions. This exclusion effect favors the formation of a compact native conformation of the protein with respect to more open unfolded conformations which would expose a higher surface area to the solvent, as illustrated in Figure 8.16. Here, we show that sorbitol increases the kinetic stability of the mAb solution under investigation by delaying the kinetics of formation of the partially unfolded aggregation-prone monomer.

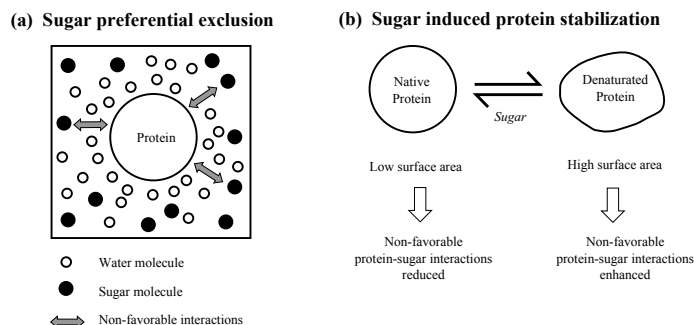


Figure 8.16: (a) Sugar molecules are *preferentially excluded* from the protein surface due to unfavorable protein-sugar interactions. The protein is then said to be *preferentially hydrated*, i.e. mainly surrounded by water molecules. (b) The presence of sugar molecules favors a native (compact) conformation of the protein over an unfolded (rather open) conformation. An unfolded conformation would indeed lead to stronger non-favorable interactions due to the higher surface area exposed to the solvent. This effect delays the kinetics of protein unfolding, and therefore delays the kinetics of monomer depletion.

In the model presented above (which is also summarized in the Model 1 in Figure 8.17),

the stabilization effect of sorbitol is captured by modifying the value of the unfolding rate constant k_U at different sorbitol concentrations, with k_U decreasing upon an increase in sorbitol concentration. This lumped approach provides a semi-empirical dependence of the unfolding rate constant on the co-solute concentration, but lacks the fundamental physical description of the process and does not allow the prediction of the stabilization effect of sorbitol for non-measured co-solute concentrations.

In order to derive an explicit expression of the apparent unfolding rate constant as a function of the sorbitol concentration, we propose in the following a kinetic model that takes into account explicitly the effect of the presence of sorbitol by introducing a reversible reaction between the sugar molecules and the antibody monomers. This reversible reaction induces the formation of a stable conformation of the monomer that is unable to unfold. According to this model, denoted as Model 2 in Figure 8.17, two native monomeric conformations are considered: N , which is subject to unfolding, and N_s , which is formed in the presence of sorbitol and is unable to unfold. Consequently, the effective concentration of native monomer which can undergo unfolding is reduced in the presence of sorbitol. This reduction in the effective monomer concentration delays the kinetics of unfolding and, in turn, delays the kinetics of aggregation. In this description, the contribution of sorbitol in the stabilization reaction is described by a generic equilibrium constant K_{eq} between the protected and non-protected native monomeric species.

As a matter of fact, in the frame of Model 2, the unfolding rate constant k_U^0 is not affected by the presence of sorbitol and is equal to the value estimated in the absence of co-solute. Indeed, Model 2 accounts for the effect of sorbitol through its impact on the equilibrium between N and N_s . In particular, a larger proportion of protected monomer N_s is favored at higher sorbitol concentrations. It is noteworthy that with this approach, the determination of the parameters k_U^0 and K_{eq} (as indicated in Figure 8.17) allows predicting quantitatively the inhibition effect of sorbitol on mAb aggregation.

To derive the explicit expression of the apparent unfolding rate constant on the sorbitol concentration, it is crucial to connect the semi-empirical Model 1 with the more explicit Model 2. The formation of the aggregation-prone monomer U is equal to $k_U^0[N]$ in Model 2, while it is equal to $k_U[N_T]$ in Model 1, where:

$$[N_T] = [N] + [N_s] \quad (8.7)$$

Therefore, $k_U[N_T] = k_U^0[N]$.

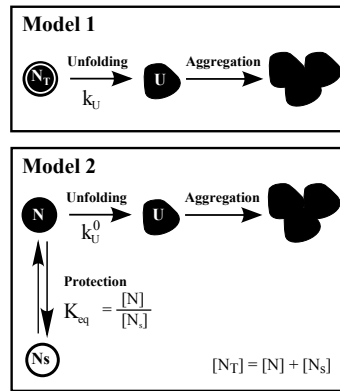


Figure 8.17: Kinetic models proposed to describe the stabilization effect of sorbitol on mAb aggregation.

The equilibrium constant between the protected and non-protected native monomer in Model 2 is defined as:

$$K_{eq} = \frac{[N]}{[N_s]} \quad (8.8)$$

It follows that:

$$[N_T] = [N](1 + 1/K_{eq}) \quad (8.9)$$

And thus:

$$k_U = \frac{k_U^0}{1 + 1/K_{eq}} \quad (8.10)$$

Where k_U^0 corresponds to the value of k_U in the absence of sorbitol. This relation shows that, from a mathematical point of view, the stabilization by sorbitol can be described equivalently either by a decrease in the unfolding rate constant of Model 1, or by a decrease in the conformational equilibrium constant of Model 2. The Wyman linkage equation states that the equilibrium constant varies with the presence of sugar according to:

$$\frac{\partial \log(K_{eq})}{\partial \log([S])} = \Delta\nu \quad (8.11)$$

Where $\Delta\nu$ is the preferential binding parameter, i.e. the difference in ligand binding between the two native states involved in the equilibrium. The preferential binding is a thermodynamic quantity which can be either positive or negative depending on the type of protein-cosolute interactions. In the case of unfavorable protein-cosolute interactions (as for example with sugars or polyols), $\Delta\nu$ is negative, reflecting the preferential exclusion of the cosolute from the protein surface, or in other words the preferential hydration of the protein. In contrast, positive $\Delta\nu$ values correspond to favorable protein-cosolute interactions, which are typically

CHAPTER 8. PROTEIN AGGREGATION

encountered with denaturants such as urea or guanidine hydrochloride. The integration of the previous equation provides the following relation:

$$K_{eq} = K_{eq,ref}[S]^{\Delta\nu} \quad (8.12)$$

Where the equilibrium constant $K_{eq,ref}$ is defined at the reference sugar concentration of 1 mol/L. The parameters $\Delta\nu$ and $K_{eq,ref}$ can be easily estimated from the K_{eq} values obtained at several sugar concentrations by using the linearized form:

$$\log(K_{eq}) = \Delta\nu \cdot \log([S]) + \log(K_{eq,ref}) \quad (8.13)$$

Once the parameters $\Delta\nu$ and $K_{eq,ref}$ of Model 2 are determined, they can be used to predict monomer depletion kinetics at other sorbitol concentrations.

Conclusion 2: Impact of co-solutes

The impact of NaCl and sorbitol on the aggregation kinetics of mAb-1 is illustrated on the energy diagram shown in Figure 8.18 (a), where the global aggregation pathway is schematically represented as an unimolecular unfolding event followed by a bimolecular collision step leading to aggregates formation. NaCl reduces the activation energy of aggregation without impacting the activation energy of protein unfolding, while sorbitol increases the activation energy of protein unfolding without impacting the activation energy of aggregation.

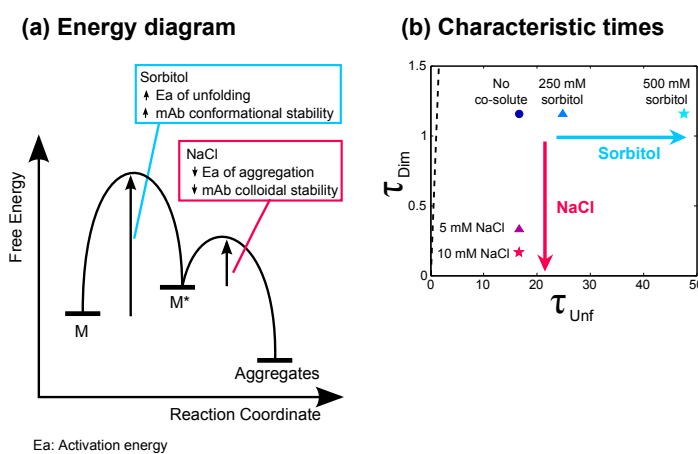


Figure 8.18: (a) Impact of NaCl and sorbitol on the aggregation pathway of mAb-1. (b) Impact of NaCl and sorbitol on the characteristic times of unfolding and dimer formation of mAb-1. The dashed black line defines the border between a process which is unfolding rate limited and a process which is aggregation rate limited.

The decrease in the energy barrier that colliding particles must overcome before aggregating in the presence of NaCl can be (at least partially) attributed to the reduction of electrostatic repulsion induced by salt addition, as suggested by the charge screening observed by zeta potential measurements. It is worth recalling here that it was shown previously that the contribution of electrostatic repulsion to the protein stability is small, and that non-DLVO forces such as hydration forces likely contribute to the protein-protein interaction potential. Hydration forces are very sensitive to the buffer composition are thus most likely affected by the presence of salt.

On the other hand, the finding that sorbitol increases the energy barrier of protein unfolding can be related to the preferential exclusion of sugars at the protein surface, which favor a compact native conformation of the proteins with respect to more open unfolded states.

It is also interesting to quantify the impact of co-solutes on the characteristic times of the various elementary events involved in the global aggregation process. As protein unfolding is a monomolecular event described by a first order kinetic, its characteristic time can simply be computed by $1/k_u$. Dimerization, instead, arises from a bimolecular collision event and is described by a second order kinetics. Its characteristic time at a reference protein concentration M_0 can be computed by $1/(k_{11}M_0)$, where k_{11} is the aggregation rate constant of dimer formation (computed from W_{11}).

The impact of co-solutes on the characteristic times of unfolding and dimer formation at the reference protein concentration of 1 g/L is summarized in Figure 8.18(b). It can be seen that in the absence of co-solutes, the characteristic time of protein unfolding is in the order of 20 min, while the characteristic time of dimer formation is in the order of 1 min, consistent with the previous finding that mAb-1 aggregation is unfolding rate-limited. It can also be observed that NaCl decreases the characteristic time of dimerization without impacting the characteristic time of protein unfolding; whereas sorbitol increases the characteristic time of protein unfolding without affecting the characteristic time of dimerization. It is worth noticing that both co-solutes increase the ratio between the characteristic time of unfolding and the characteristic time of aggregation. This important observation allows us to conclude that the monomer depletion remains rate-limited by protein unfolding upon addition of NaCl or sorbitol. The monomer depletion of mAb-1 could potentially become aggregation rate-limited upon addition of a co-solute which is either increasing the characteristic time of aggregation, or reducing the characteristic time of unfolding, such as urea or guanidinium chloride, which are known to be strong denaturants.

8.7.2 Case Study 2: mAb-2

Experimental Observations

Figure 8.19 shows some experimental observations regarding mAb-2 aggregation. We conclude from these data that, in the case of mAb-2:

- (a) The monomer depletion is rate-limited by bimolecular aggregation events
- (b) Aggregation is reversible
- (c) Aggregates exhibit fractal morphology, with $d_f = 2.05$

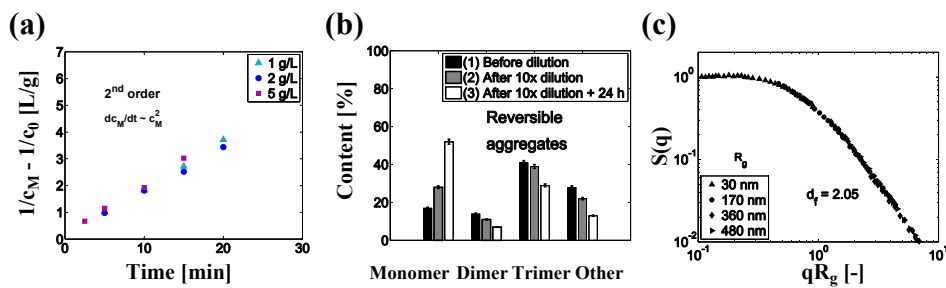


Figure 8.19: Experimental observations for mAb-2. (a) Linearization of the monomer depletion kinetics followed by SEC (b) Dilution experiments to assess aggregates reversibility (c) SLS experiment to measure the fractal dimension of aggregates.

Reaction Scheme

According to these experimental observations, the scheme of Figure 8.20 is proposed to describe mAb-2 aggregation.

At the considered high temperature (70°C), a population of partially unfolded conformational states of the antibody is likely present. However, since the aggregation process is limited by bimolecular collisions, the collected set of experimental data does not provide information on the kinetics and thermodynamics of the unfolding step. It is therefore not possible to determine which monomeric form is involved in the aggregation process. For the sake of generality, we consider reversible monomeric changes from the native state (N) to a non-native state of the protein (U), as schematized in step (M2-1) of the reaction scheme, and we introduce a generic aggregation-prone intermediate (M) in the aggregation kinetic scheme. This generic

CHAPTER 8. PROTEIN AGGREGATION

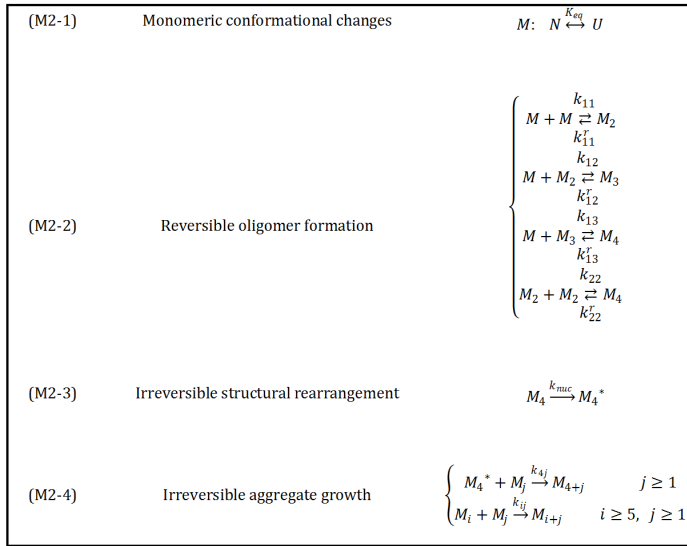


Figure 8.20: Proposed reaction scheme proposed for mAb-2 aggregation.

intermediate is able to represent in a coarse-grained approach all the possible unfolding scenarios. Two limiting cases consistent with the observed second order kinetics of the monomer depletion could occur: the protein could react (i) in its native form ($M = N$) or (ii) in a denatured state ($M = U$) provided that the generation of U is fast compared to its consumption by aggregation. The hypothesis (i) is less likely than (ii) since the native form of the protein is usually the more stable, but it cannot be excluded given the set of experimental data.

The reactive monomeric state can form a nucleus by reversible oligomerization followed by irreversible structural rearrangement, according to the steps (M2-2) and (M2-3) in Figure 8.20, respectively. It can be noticed from the reversibility experiments that not only the dimer and trimer concentrations are reduced upon dilution, but also the concentration of larger oligomers. Since all aggregates larger than trimer elute from SEC in a single unresolved peak, the size of the largest reversible aggregate cannot be determined with accuracy. In the absence of precise information on the reversible oligomer formation, tetramer was assumed to be the largest reversible aggregate.

The complete description of reversible tetramer formation requires eight parameters (four forward reactions and four backward reactions). The reversibility experiments showed that the aggregates are not equally reversible, and in particular trimer appears to be the least reversible species. In order to reduce the number of fitting parameters, we assumed that oligomer formation can be described by a single Fuchs stability ratio, i.e. $W_{11} = W_{12} = W_{13} = W_{22}$. In addition, we assumed that each bound inside the tetramer can break with equal probabil-

CHAPTER 8. PROTEIN AGGREGATION

ity, and therefore $k_{13}^r \approx 2k_{22}^r$, since the probability that a tetramer breaks into one monomer and one trimer is two times higher than the probability to form two dimers. Consequently, the number of parameters describing reversible oligomerization is reduced from eight to four ($W_{11}, k_{11}^r, k_{12}^r, k_{13}^r$).

Finally, the step (M2-4) in the reaction scheme represents aggregate growth, which can occur either by monomer addition or by cluster-cluster aggregation. As is the case of mAb-1, aggregate growth is described by Smoluchowski PBE, using the usual RLCA kernel, as already presented in Equation 8.5. In order to account for the differences in reactivity of the various populations present in solutions, three different Fuchs ratios have been considered: one for oligomer formation (W_{11}), one for nucleus consumption (W_{4^*j}), and one for cluster-cluster aggregation (W_{ij}).

Population Balance Equations

$$\left\{ \begin{array}{l} \frac{dM}{dt} = -k_{1,1}MM - M \sum_{j=2}^{\infty} k_{1,j}M_j + 2k_{11}^rM_2 + k_{12}^rM_3 + k_{13}^rM_4 \\ \frac{dM_2}{dt} = \frac{1}{2}k_{1,1}MM - k_{1,2}MM_2 - k_{2,2}M_2M_2 - k_{2,4^*}M_2M_{4^*} - M_2 \sum_{j=5}^{\infty} k_{2,j}M_j + 2k_{22}^rM_4 - k_{11}^rM_2 \\ \frac{dM_3}{dt} = k_{1,2}MM_2 - k_{1,3}MM_3 - k_{3,4^*} - M_3 \sum_{j=5}^{\infty} k_{3,j}M_j + k_{13}^rM_4 - k_{12}^rM_3 \\ \frac{dM_4}{dt} = k_{1,3}MM_3 + \frac{1}{2}k_{2,2}M_2M_2 - k_{2,2}M_4 - k_{nuc}M_4 \\ \frac{dM_{4^*}}{dt} = k_{nuc}M_4 - M_{4^*} \sum_{j=1}^{\infty} k_{4^*,j}M_j \\ \frac{dM_{i \geq 5}}{dt} = k_{4^*,i-4}M_{4^*}M_{i-4} + \frac{1}{2} \sum_{j=5}^{i-1} k_{j,i-j}M_jM_{i-j} - k_{4^*,i}M_{4^*}M_i - M_i \sum_{j=5}^{\infty} k_{i,j}M_j \end{array} \right. \quad (8.14)$$

Parameter Estimation

The fractal dimension was measured by SLS and λ was estimated as $\lambda \approx 1 - 1/d_f$. All the other parameters ($W_{11}, W_{4^*j}, W_{ij}, k_{11}^r, k_{12}^r, k_{13}^r, k_{nuc}$) were estimated by fitting to the experimental data at the reference protein of 2 g/L. The parameter values are summarized in Table 8.4.

Parameter	d_f	λ	W_{11}	W_{4^*j}	W_{ij}
Value	2.05	0.5	2.7×10^7	10^6	4×10^8
Source	SLS	$1 - 1/d_f$	Fit	Fit	Fit
Parameter	k_{11}^r	k_{12}^r	k_{13}^r	k_{nuc}	
Value	4.4×10^{-3}	1.4×10^{-4}	1.3×10^{-2}	3.7×10^{-3}	
Source	Fit	Fit	Fit	Fit	

Table 8.4: Parameters used for the simulations of mAb-2 aggregation (without co-solutes).

In Figure 8.21, we present the comparison between experimental and simulated kinetics of aggregation of mAb-2. It can be seen that the simulations are in very close agreement with all experimentally accessible quantities.

Model Validation

With the parameters determined at the reference protein concentration of 2 g/L we then simulate the aggregation kinetics at 1 g/L and 5 g/L, thus testing the capability of the model to predict the concentration dependence of the aggregation rate (see Figure 8.21). The model predictions of the monomer depletion, dimer and trimer formation, as well as the aggregate weight average molecular weight and average hydrodynamic radius of the non-fractionated population are in good agreement with the experimental data, confirming the validity of the proposed kinetic model.

As in the case of mAb-1, the ranking of the Fuchs stability ratios provides information on the relative reactivity of the different species present in the system. Considering the values of W reported in Table 8.4, the various species involved in the kinetic mechanism can be classified according to their reactivity in the following order: nucleus > oligomers > large aggregates. This observation is consistent with the definition of nucleus as the least stable species present in the system.

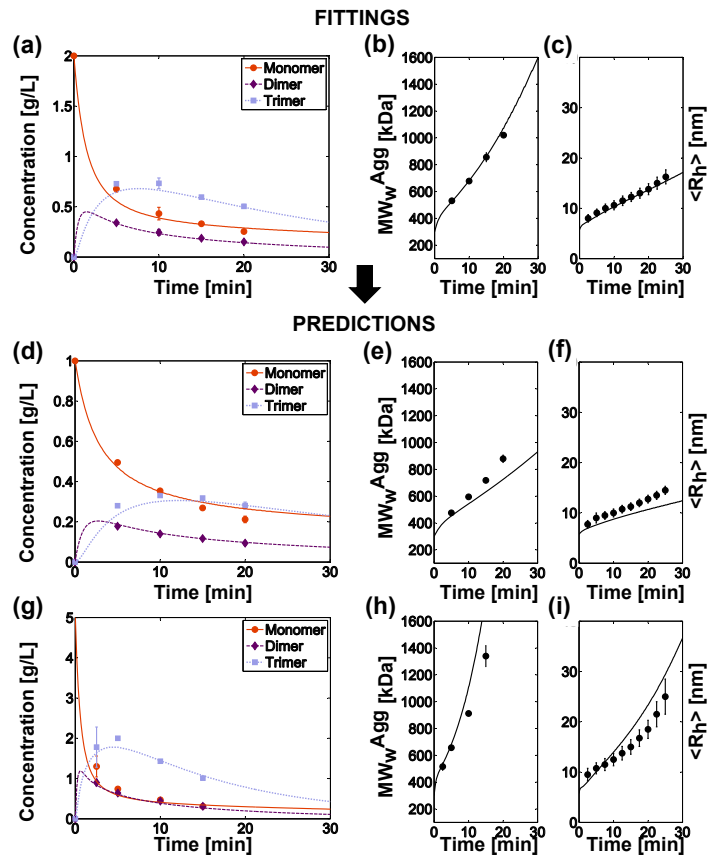


Figure 8.21: Comparison between experimental data and simulations for mAb-2 at protein concentration of 2 g/L (a-c), 1 g/L (d-f) and 5 g/L (g-i). The experimental concentration of monomer, dimer and trimer were determined by SEC. The aggregate molecular weight was measured by SEC-MALS and the average hydrodynamic radius was followed by DLS.

Conclusion 1: Kinetic Mechanism

We can therefore conclude that the kinetic scheme of mAb-2 aggregation is the one presented in Figure 8.22.

Comparison with DLVO theory

In the case of mAb-2, a zeta potential value of $\zeta = +0.5mV$ was measured, which corresponds to a protein net charge of $z \approx +0.4$. The simulations of the inter-particle potential in the frame of the DLVO theory are shown in Figure 8.23.

As in the case of mAb-1, a value of $W_{11}^{DLVO} \approx 1$ is obtained, which is several order of magnitude smaller than the one estimated by kinetic analysis. This confirms that the large

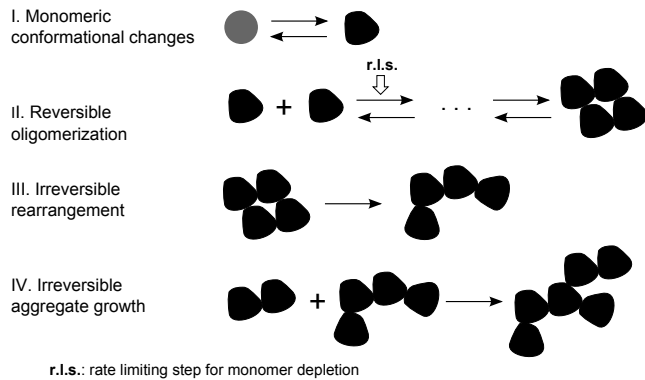


Figure 8.22: Kinetic scheme for mAb-2 aggregation

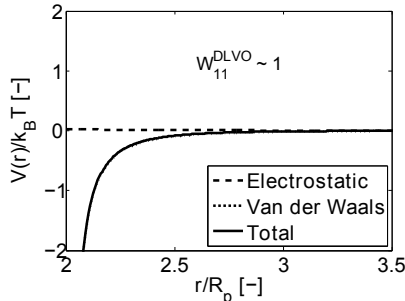


Figure 8.23: Computed protein interaction potential for mAb-2 in the frame of the DLVO theory. stability of antibody solutions cannot be explained by electrostatic repulsion only.

Impact of NaCl

In the following, we investigate the impact of NaCl on the aggregation kinetics of mAb-2 at the protein concentration of 1 g/L. Figure 8.24 shows the experimental data of mAb-2 aggregation in the absence of salt as well as in the presence of 10 mM and 50 mM NaCl.

In Figure 8.24, it can be observed that the presence of NaCl accelerates both the monomer depletion and the aggregate growth. In addition, it is worth noting that for a given monomer conversion, the aggregate weight average molecular weight (Figure 8.24 (e)), as well as the dimer and trimer concentrations (data not shown) are independent of salt concentration. This important observation indicates that the aggregate distribution obtained at a given monomer conversion is independent of the salt concentration. Since specific promotion of nucleation or growth events would affect in a different way the aggregate distribution at a given monomer conversion, the analysis provides evidence that NaCl does not impact specific steps of the reaction scheme but rather accelerates similarly all the elementary steps of the aggregation

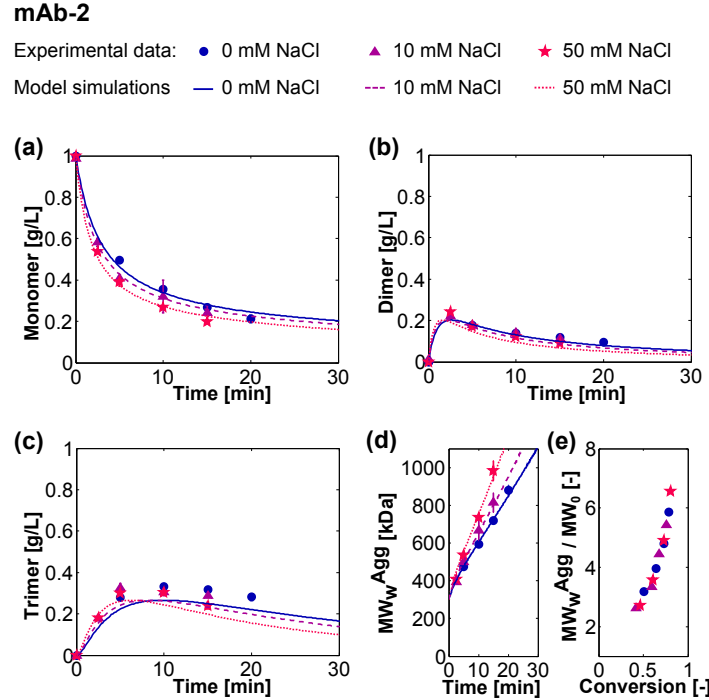


Figure 8.24: Comparison between experimental data and simulations for mAb-2 aggregation kinetics in the absence of co-solute and with 10 and 50 mM NaCl.

process. (Note that this was not the case for mAb-1. Indeed, the presence of NaCl was leading to an increase in the aggregate molecular weight at a given conversion due to the fact that NaCl specifically accelerates aggregate growth of mAb-1 with respect to protein unfolding.)

Based on these considerations, we introduce a parameter α_2 defined as the ratio of the value of each kinetic rate constant (corresponding either to an aggregation, dissociation or nucleation event) in the presence of co-solute divided by the corresponding value in the absence of co-solute. Since the aggregation rate constants are inversely proportional to the Fuchs ratios, α_2 is defined as:

$$\alpha_2 = \frac{W_{11}^{-CS}}{W_{11}^{+CS}} = \frac{W_{4^*j}^{-CS}}{W_{4^*j}^{+CS}} = \frac{W_{ij}^{-CS}}{W_{ij}^{+CS}} = \frac{k_{11}^{r+CS}}{k_{11}^{r-CS}} = \frac{k_{12}^{r+CS}}{k_{12}^{r-CS}} = \frac{k_{13}^{r+CS}}{k_{13}^{r-CS}} = \frac{k_{nuc}^{+CS}}{k_{nuc}^{-CS}} \quad (8.15)$$

At each salt concentration, the parameter α_2 was evaluated by fitting to the experimental data. Due to sample precipitation at large aggregate sizes, the fractal dimension of mAb-2 aggregates in the presence of salt could not be measured experimentally, and was thus assumed to be the same as the one estimated in the absence of salt. The power law factor λ appearing in the aggregation kernel has been estimated as $\lambda = 1 - 1/d_f$. The parameters used for the

simulations are summarized in Table 8.5.

Parameter	d_f	λ	α_2
10 mM NaCl	2.05	0.5	1.2
50 mM NaCl	2.05	0.5	1.6
Source	Unchanged	$1 - 1/d_f$	Fit

Table 8.5: Parameters used for the simulations of mAb-2 aggregation in the presence of NaCl.

As shown in Figure 8.24, the simulations are in very good agreement with the set of experimental data. Therefore, the kinetic analysis confirms that NaCl accelerates in a concentration dependent manner all the elementary steps involved in the aggregation scheme to the same extent.

Impact of Sorbitol

Finally, the impact of sorbitol on the aggregation kinetics of mAb-2 was investigated (still at the protein concentration of 1 g/L). Experimental data are presented in Figure 8.25, showing that sorbitol is capable of delaying both the monomer depletion and the aggregate growth. As in the case of NaCl, the aggregate weight average molecular weight (Figure 8.25 (e)) as well as the dimer and trimer concentrations (data not shown) obtained at a given monomer conversion are not affected by the presence of sorbitol. This suggests that the presence of sorbitol does not impact the aggregate distribution at a given monomer conversion, indicating that sorbitol does not impact specific steps of the reaction scheme but rather delays all the elementary steps of the aggregation process to the same extent.

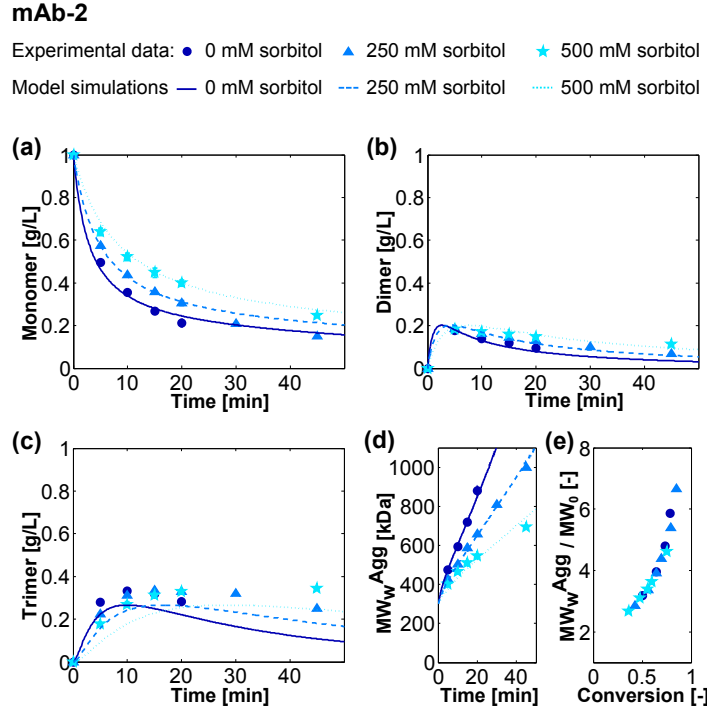


Figure 8.25: Comparison between experimental data and simulations for mAb-2 aggregation kinetics in the absence of co-solute and with 250 and 500 mM sorbitol.

Similarly to the approach used in the case of NaCl, we performed the simulations of the inhibited aggregation kinetics in the presence of sorbitol by considering the set of kinetic rate constants evaluated in the absence of sorbitol multiplied by a constant factor α_2 , which was determined by fitting to the experimental data. Moreover, the fractal dimension was measured by SLS and λ was estimated $\lambda = 1 - 1/d_f$. The parameters used for the simulations are summarized in Table 8.6.

Parameter	d_f	λ	α_2
250 mM sorbitol	2.05	0.5	0.60
500 mM sorbitol	2.05	0.5	0.35
Source	SLS Exp.	$1 - 1/d_f$	Fit

Table 8.6: Parameters used for the simulations of mAb-2 aggregation in the presence of sorbitol.

As shown in Figure 8.25, the model simulations describe very well the set of experimental

CHAPTER 8. PROTEIN AGGREGATION

data, thus confirming that sorbitol delays in a concentration dependent manner all the elementary steps that contribute to the global aggregation process in equal measure.

Conclusion 2: Impact of co-solutes

While NaCl and sorbitol were shown to impact specific elementary steps in the aggregation mechanism of mAb-1, the addition of co-solutes in the case of mAb-2 was found to impact all the elementary steps (i.e. reversible oligomerization, irreversible oligomer rearrangement and irreversible aggregate growth) to the same extent. While all the elementary steps that contribute to the global aggregation process were found to be accelerated in equal measure upon NaCl addition, they were found to be all delayed to the same extent in the presence of sorbitol.

8.8 Conclusion

To conclude, in this chapter, we showed **how some concepts developed for colloid science can be applied to study protein aggregation**. We also highlighted some key differences between traditional polymer colloidal particles and protein systems. This is summarized Table 8.7.

	What can be borrowed from colloid science	What needs to be added in the case of proteins
Experimental Characterization	<ul style="list-style-type: none">• Charge (zeta potential)• d_f (SLS)• Increase in R_h (DLS)	<ul style="list-style-type: none">• Conformation stability (DSC,CD)• Monomer and oligomer (SEC)• MW_{Agg} (SEC-MALS)
Mechanisms and Population Balance Equations	Irreversible aggregate growth: → Aggregation kernel → Smoluchowski PBE	<ul style="list-style-type: none">• Protein unfolding• Reversible oligomerization• Irreversible oligomer rearrangement
Fuchs Ratio	$W = W_{11}$	Several W values
Colloidal Stability	DLVO for electrostatics	<ul style="list-style-type: none">• Surface patchiness• Additional forces (e.g.: hydration)

Table 8.7: Input and limits of colloid science to study protein aggregation.

We showed how it is possible to combine experimental data with theoretical kinetic analysis to gain knowledge on the mechanisms of protein aggregation, and to extract relevant information on the impact of co-solutes on the kinetics of aggregation. The approach is illustrated here

CHAPTER 8. PROTEIN AGGREGATION

with two mAbs and two co-solutes, but is sufficiently general to be applied to other systems.

This study revealed that under the same operating conditions, the two mAbs follow different aggregation mechanisms, and are affected differently by the presence of co-solutes. These behaviors are specific to the proteins examined, and do not identify the particular immunoglobulin classes IgG1 and IgG2. This shows the large variety of behaviors that proteins may exhibit due to their chemical structure complexity.

References

POLYMER REACTION ENGINEERING

- Dotson, N. A., *Polymerization process modeling*. VCH: New York 1996.
- Flory, P. J., *Principles of polymer chemistry*; Cornell University Press, 2006.
- Hamielec, A. E., *Polymerization Processes, 2. Modeling of Processes and Reactors*. Ullmann's Encyclopedia, Wiley-VCH 2000.
- Nomura, M., *Emulsion polymerization: Kinetic and mechanistic aspects*. *Polymer Particles* 2005, 175, 1-128.
- Odian, G., *Principles of polymerization*. 4th ed.; Wiley, 2004

COLLOIDAL ENGINEERING

- Berg, J. C., *An introduction to interfaces and colloids the bridge to nanoscience*. World Scientific 2010.
- Cosgrove, T., *Colloid science principles, methods and applications*. 2nd ed.; Wiley 2010.
- Friedlander, S. K., *Smoke, dust, and haze fundamentals of aerosol dynamics*. 2nd ed.; Oxford University Press 2000.
- Israelachvili, J. N., *Intermolecular and surface forces*. 3rd ed.; Academic Press 2011.
- Jia, Z. C., *A generalized model for the stability of polymer colloids*. *Journal of Colloid and Interface Science* 2006.
- Lin, M. Y., *Universality in Colloid Aggregation*. *Nature* 1989, 339, 360-362.
- Sandkuhler, P., *Modeling structure effects on aggregation kinetics in colloidal dispersions*. *Aiche Journal* 2003, 49, 1542-1555.
- Chi, E.Y., *Physical stability of proteins in aqueous solution: mechanism and driving forces in nonnative protein aggregation*. *Pharmaceutical Research* 2003, 20, 1325-1336.
- Roberts, C.J., *Non-native protein aggregation kinetics*. *Biotechnology and Bioengineering*

CHAPTER 8. PROTEIN AGGREGATION

2007, 98, 927-93.

Wang, W., *Protein aggregation and its inhibition in biopharmaceutics. International Journal of Pharmaceutics* 2005, 289, 1-30.

Nicoud, L., *Kinetic Analysis of the Multistep Aggregation Mechanism of Monoclonal Antibodies. Journal of Physical Chemistry A*, 2014.